• U C •

FCTUC FACULDADE DE CIÊNCIAS
E TECNOLOGIA
UNIVERSIDADE DE COIMBRA

DEPARTAMENTO DE
ENGENHARIA MECÂNICA

Failure prediction in can's deep drawing

Submitted in Partial Fulfilment of the Requirements for the Degree of Master in Mechanical Engineering in the speciality of Production and Project

Previsão da rotura na estampagem de embalagens metálicas

Author
Pedro Daniel Mendes Carvalho

Advisors
Marta Cristina Cardoso de Oliveira
Pedro Daniel Pleno Rascão de Barros

Jury

President	**Professor Doutor Diogo Mariano Simões Neto** **Professor Convidado da Universidade de Coimbra**
Vowel	**Professor Doutor José Luís de Carvalho Martins Alves** **Professor Associado da Universidade do Minho**
Advisor	**Professora Doutora Marta Cristina Cardoso de Oliveira** **Professora Auxiliar da Universidade de Coimbra**

Coimbra, July, 2016

To João, Ana Bela, André and Andreia.

“Anyone who has never made a mistake has never tried anything new.”

Albert Einstein

ACKNOWLEDGEMENTS

Immeasurable appreciation and deepest gratitude for the help and support are extended to the following people who in one way or another have contributed in making this thesis possible.

To Professora Doutora Marta Oliveira,
For her guidance, support, motivation, power and willingness.

To Engenheiro Pedro Barros,
For his guidance, friendship, patience and dedication.

To Professor Doutor Luís Menezes, Professor Doutor Diogo Neto, Mestre João Martins,
For sharing their scientific skills in our meetings.

To Professor Doutor Luís Alves,
For his time and effort to clarifying some hard questions.

To Patrick Cunha and Tomás Neves,
For their suggestions and valuable comments.

To all my friends,
For their encouragement and loyalty.

To my family,
For their support and care through all life.

To Andreia,
For her love, care and friendship.

Abstract

The deep drawing process is a suitable operation to produce cans. Although those containers are also manufactured with ceramics and plastics materials, aluminum and steel are typically used, considering safety and manufacturing costs. Nowadays, the finite elements analysis is commonly used in the cans tool design since it allows predicting quickly and accurately the earing profile, the thickness reduction and the occurrence of failure. However, the prediction of these phenomena is strongly affected by the material properties and also by the process conditions. Thus, it is important to improve the knowledge concerning the suitable constitutive model and numerical parameters.

The process conditions considered in this work are the ones established for the BENCHMARK 1 – Failure Prediction after Cup Drawing, Reverse Redrawing and Expansion, proposed under the NUMISHEET 2016 international conference. In this example, the cup's deep drawing is performed considering three processes: drawing, reverse redrawing and expansion. The aim is to predict the failure point, knowing this multi-step process causes complex nonlinear strain paths.

The two materials considered are an AA5352 aluminum alloy and a TH330 steel, whose mechanical behavior is modelled taking into account the available experimental information. In order to understand the influence of the yield criterion, the mechanical behavior is modelled, for both materials, with the CB2001 yield criterion, which is known for its accurate description of the material anisotropic behavior, and with the CPB06, which also enables the description of tension-compression asymmetry. The numerical simulation of the forming process is performed using DD3IMP in-house code.

The punch force evolution and the cup height in all phases, the thickness profile, after the reverse redrawing operation, and the strain paths are the evaluated variables. To try to predict the failure point in both materials, three methods were used, including the strain-based FLC, stress-based FLC and the through-thickness strain rate analysis.

Globally, the aluminum alloys show a higher earing profile and number of ears than the steel. Moreover, it was only possible to predict the failure point in the AA5352

aluminum alloy with CB2001 yield criterion. Although the experimental results are not yet available, the aluminum alloy presents lower mechanical strength and lower formability for monotonic loads, as shown in the strain-based FLC. Thus, the fact that the aluminum alloy presents necking while no localized strain is predicted for steel is expected an accurate prediction.

Keywords Deep-drawing, Finite element analysis, Yield criteria, Earing prediction, Failure prediction.

Resumo

A manufatura de latas, essencialmente associadas à conservação de alimentos, está muito ligada a processos de estampagem. Embora este tipo de lata possa ser construído com materiais cerâmicos ou plásticos, são tipicamente usadas ligas de aço e alumínio, devido à sua fiabilidade e custo reduzido. Atualmente, recorre-se a programas de simulação numérica na conceção das ferramentas de estampagem para a produção de latas, uma vez que permitem prever com elevada rapidez e exatidão a ocorrência de orelhas de estampagem, redução de espessura, ou mesmo de rotura. No entanto, a previsão destes fenómenos é fortemente influenciada pelas propriedades do material e ainda pelas condições do processo. Assim, é importante melhorar o conhecimento sobre os modelos constitutivos e os parâmetros numéricos a adotar.

O exemplo analisado neste trabalho é o processo multi-etapa de estampagem de uma lata, que se enquadra com o caso de estudo: *BENCHMARK 1 – Failure Prediction after Cup Drawing, Reverse Redrawing and Expansion*, proposto no âmbito da conferência internacional NUMISHEET 2016. O processo de conformação da taça é composto por três fases consecutivas: estampagem, estampagem inversa e expansão. O objetivo é a previsão do ponto de rotura, sabendo que este processo multi-etapa envolve trajetórias complexas, não-lineares, de deformação.

Os dois materiais em estudo são uma liga de alumínio, AA5352, e um aço, TH330, sendo o seu comportamento mecânico descrito com base na informação experimental disponível. De modo a compreender a influência do critério de plasticidade, o comportamento mecânico dos dois materiais é modelado com o critério de plasticidade CB2001, conhecido por permitir uma correta descrição do comportamento anisotrópico do material, e com o CPB06, que permite também a descrição da assimetria entre o comportamento à tração e à compressão. As simulações numéricas do processo foram realizadas com o programa DD3IMP.

As variáveis analisadas foram a evolução da força dos diferentes punções, a altura da taça em cada fase, o perfil de espessura depois da estampagem inversa, e as trajetórias de deformação. Para procurar prever o ponto de rotura, para ambos os materiais,

foram testados três critérios: curva limite de estampagem (CLE) definida no espaço das deformações, CLE definida no espaço das tensões e análise da taxa de redução da espessura.

Globalmente, os resultados mostram que a liga de alumínio apresenta um maior número de orelhas de estampagem, de maior amplitude, do que o aço. Além disso, apenas foi possível prever a rotura para o alumínio AA5352 com o critério de plasticidade CB2001. Apesar de os resultados experimentais não estarem ainda disponíveis, a liga de alumínio apresenta menor resistência mecânica e menor formabilidade, para trajetórias monótonas, como mostra a CLE. Assim, o facto de ser prevista rotura para a liga de alumínio, e não ser para o aço, pode estar de acordo com os resultados experimentais.

Palavras-chave: Estampagem, Análise pelo método dos elementos finitos, Critério de plasticidade, Previsão das orelhas de estampagem, Previsão de rotura.

Contents

LIST OF FIGURES xi

LIST OF TABLES xv

SIMBOLOGY AND ACRONYMS xvii
Simbology xvii
Acronyms xix

1. INTRODUCTION 1
1.1. Background 1
1.2. Objectives 9
1.3. Numerical Simulation Software 10
1.4. Reading guide 12

2. CUP MULTI-STAGE FORMING: FE MODEL 13
2.1. Blank sheet discretization 13
2.2. Process and tool modelling 16
2.2.1. Drawing operation 17
2.2.2. Reverse redrawing operation 20
2.2.3. Expansion operation 22
2.2.4. Discussion 25
2.3. Material mechanical behaviour 25
2.3.1. Yield criteria 26
2.3.2. Hardening laws 31
2.3.3. Materials characterization 33
2.4. Failure prediction 41
2.4.1. Strain-based and stress-based FLC 41
2.4.2. Strain rate analysis – linear best fit 45
2.4.3. GTN Model 46

3. RESULTS AND DISCUSSION 51
3.1. Drawing operation 51
3.2. Reverse redrawing operation 56
3.3. Expansion operation 62
3.4. Strain-based FLC and strain paths 64
3.5. Stress-based FLC 68
3.6. Strain rate analysis – linear best fit 73

4. CONCLUDING REMARKS 77

5. REFERENCES 79

ANNEX A 85

LIST OF FIGURES

Figure 1.1. Schematic illustration of the stamping process (based on Wallmeier et al., 2015). 2

Figure 1.2. (a) Three-piece can (extracted from “http://www.clker.com”); (b) Two-piece can (extracted from “http://www.slideshare.net”). 2

Figure 1.3. (a) Earing profile in HSLA steel cup (extracted from Nikhare et al., 2008); (b) Earing profile evolution in an aluminum cylindrical cup (extracted from “http://www.expack.co.uk”). 3

Figure 1.4. Schematic of several tension modes in a strain-based FLD (extracted from Hasan et al., 2011). 5

Figure 1.5. Illustration of FFL and SFFL (adapted from Isik et al., 2014). 6

Figure 1.6. Numisheet 2016 – Benchmark 1 (extracted from Watson et al., 2016). 8

Figure 1.7. Numisheet 2011 – Benchmark 1 (extracted from Dick, 2011). 9

Figure 1.8. Numisheet 2014 - Benchmark 1 (extracted from Du et al., 2013). 9

Figure 2.1. In-plane: definition of different regions in the blank. 14

Figure 2.2. Final blank: in-plane discretization. 16

Figure 2.3. Drawing operation: (a) concept (b) model. 17

Figure 2.4. Drawing operation – Punch 1: (a) concept (b) model. 18

Figure 2.5. Drawing operation – Die 1: (a) concept (b) model. 19

Figure 2.6. Drawing operation – Pressure-pad 1: (a) concept (b) model. 19

Figure 2.7. Drawing operation – Aluminum cup: (a) Before drawing (b) After drawing... 19

Figure 2.8. Redrawing operation: (a) concept (b) model. 20

Figure 2.9. Redrawing operation – Punch 2: (a) concept (b) model. 21

Figure 2.10. Redrawing operation – Pressure-pad 2: (a) concept (b) model. 21

Figure 2.11. Redrawing operation – Aluminum cup: (a) Before redrawing (b) After redrawing. 22

Figure 2.12. Expansion operation without clamp for steel TH330 showing the wrinkling effect. 22

Figure 2.13. Expansion operation: (a) concept (b) model. 23

Figure 2.14. Expansion operation – Punch 3: (a) concept (b) model. 24

Figure 2.15. Expansion operation – Cup support: (a) concept (b) model. 24

Figure 2.16. Expansion operation – Clamp: (a) concept (b) model. 24

Figure 2.17. Expansion operation – Aluminum cup: (a) before expansion (b) after expansion (until failure). 25

Figure 2.18. (a) Plane stress yield loci according to CPB06 for different values of the ratio (σ^T / σ^C) between the yield stress in tension and compression, in comparison with the von Mises yield locus (b) Plane stress yield loci corresponding to $k = 0.2$ and $k = -0.2$ (extracted from Cazacu et al., 2006). 29

Figure 2.19. Subsequent and initial yield surface with (a) isotropic and (b) kinematic hardening (extracted from Banabic, 2010). 32

Figure 2.20. Experimental and predicted yield stresses for (a) AA5352 aluminum alloy and (b) TH330 steel. 37

Figure 2.21. Experimental and predicted r-values for (a) AA5352 aluminum alloy and (b) TH330 steel. 38

Figure 2.22. Predicted yield surfaces in the σ_{11}, σ_{22} plane for (a) AA5352 aluminum alloy and (b) TH330 steel..... 39

Figure 2.23. Deformation of an element on the flange, stress states on the flange (left) and stress states on the yield surface (right): (a) isotropic material, with symmetric tension-compression behavior; (b) material with asymmetric tension-compression behavior (adapted from Yoon et al., 2011). 40

Figure 2.24. Strain-based FLC for: (a) AA5352 aluminum alloy; (b) TH330 steel. 42

Figure 2.25. Stress-based FLC for: (a) AA5352 aluminum alloy; (b) TH330 steel. 45

Figure 2.26. Evolution of the necking: (a) Thinning; (b) Thinning rate (extracted from Volk & Hora, 2010). 45

Figure 2.27. Force-displacement diagram indicating the 4 stages of voids evolution. 48

Figure 3.1. Punch 1 load evolution with its stroke during the drawing operation for: (a) AA5352 aluminum alloy and (b) TH330 steel..... 52

Figure 3.2. Pressure-pad 1 force evolution with the punch 1 stroke during the drawing operation for: (a) AA5352 aluminum alloy and (b) TH330 steel. 53

Figure 3.3. Pressure-pad 1 stroke evolution with the punch 1 stroke during the drawing operation for: (a) AA5352 aluminum alloy and (b) TH330 steel. 54

Figure 3.4. Deformation along the thickness direction after the drawing operation for AA5352 aluminum alloy with: (a) CB2001 and (b) CPB06 yield criteria. 54

Figure 3.5. Deformation along the thickness direction after the drawing operation for TH330 steel with: (a) CB2001 and (b) CPB06 yield criteria..... 54

Figure 3.6. Cup height after drawing operation for (a) AA5352 aluminum alloy and (b) TH330 steel. 55

Figure 3.7. Punch 2 force evolution with the punch 2 stroke during the reverse redrawing operation for (a) AA5352 aluminum alloy and (b) TH330 steel. 56

Figure 3.8. Pressure-pad 2 force evolution with the punch 2 stroke during the reverse redrawing operation for (a) AA5352 aluminum alloy and (b) TH330 steel. 57

Figure 3.9. Pressure-pad 2 stroke evolution with the punch 2 stroke during the reverse redrawing operation for (a) AA5352 aluminum alloy and (b) TH330 steel. 58

Figure 3.10. Deformation along the thickness direction for the AA5352 aluminum alloy and a 50 mm punch stroke, as predicted by the yield criterion: (a) CB2001 and (b) CPB06. The black lines correspond to the ones that will be located at 20 mm and 45 mm from the cup bottom, at the end of the redrawing stage. 59

Figure 3.11. Deformation along the thickness direction for the TH330 steel and a 50 mm punch stroke, as predicted by the yield criterion: (a) CB2001 and (b) CPB06. The black lines correspond to the ones that will be located at 20 mm and 45 mm from the cup bottom, at the end of the redrawing stage. 59

Figure 3.12. Cup height after the reverse redrawing operation for (a) AA5352 aluminum alloy and (b) TH330 steel. 60

Figure 3.13. Thickness profile at a height of 20 mm from the base of the cup after the reverse redrawing operation for: (a) AA5352 aluminum alloy and (b) TH330 steel. The dashed line corresponds to the gap between the punch and the die of the redrawing operation. 60

Figure 3.14. Thickness profile at a height of 45 mm from the base of the cup after the reverse redrawing operation for: (a) AA5352 aluminum alloy and (b) TH330 steel. The dashed line corresponds to the gap between the punch and the die of the redrawing operation. 61

Figure 3.15. Contact forces when punch 2 stroke is 50 mm for AA5352 aluminum alloy with yield criterion: (a) CB2001 and (b) CPB06. 62

Figure 3.16. Punch 3 force evolution with the punch 3 stroke during the expansion operation for (a) AA5352 aluminum alloy and (b) TH330 steel. 63

Figure 3.17. Deformation along the thickness direction after the expansion operation for AA5352 aluminum alloy with yield criterion (a) CB2001 and (b) CPB06. 63

Figure 3.18. Deformation along the thickness direction after the expansion operation for TH330 steel with yield criterion (a) CB2001 and (b) CPB06. 64

Figure 3.19. Schematic representation of the interpolation method adopted to compare the numerical results with the FLC strain-based. 65

Figure 3.20. FLC strain-based for the AA5352 aluminum alloy and the strain paths at the leading edge of the cup at 0^0, 45^0 and 90^0, respected to each stage. 67

Figure 3.21. FLC strain-based for TH330 steel and the strain paths at the leading edge of the cup at 0^0, 45^0 and 90^0, respected to each stage. 67

Figure 3.22. Schematic representation of the orthotropic frame in the: (a) blank and (b) in the vertical wall. 68

Figure 3.23. Necking analysis with stress-based FLC: (a) Pure bending *vs* High tension bending; (b) Stress necking limit (extracted from Stoughton & Yoon, 2011). 69

Figure 3.24. (a) Schematic representation of the hexahedral solid element with the 8 GP used in selective reduced integration, identified by local numbers; (b) Four

possible combinations of GPs of two elements, corresponding to necking occurrence. 70

Figure 3.25. Evaluation of σ_1 with σ_2 for the AA5352 aluminum alloy with CB2001 yield criterion. 72

Figure 3.26. Deformation along the thickness direction when the simulation for the AA5352 aluminum alloy with CB2001 yield criterion stopped according to the strategy using stress-based FLC. 72

Figure 3.27. Analysis of the deformation and thinning rate during expansion operation for the AA5352 aluminum alloy with yield criterion CB2001, for the element identify for the onset of failure. 74

Figure 3.28. Linear best fit. 75

Figure 3.29. Comparison of the strain paths for points located in RD, 45^0 and TD with the point where necking occurs (necking). 75

Figure A.1. Void volume fraction evolution predicted using the GTN model for a single element, considering different values for the stress triaxiality (labeled "T") for two values of the Lode parameter (labeled "L"). 87

Figure A. 2. Void volume fraction evolution predicted for a three-dimensional unit cell, considering the CPB06 (continuous line) and the Hill'48 (dashed line) yield criteria, using different values for the stress triaxiality (labeled "T") and a Lode parameter equal to 1.0. 87

Figure A. 3. Void volume fraction evolution predicted for a three-dimensional unit cell, considering the CPB06 (continuous line) and the Hill'48 (dashed line) yield criteria, using different values for the stress triaxiality (labeled "T") and a Lode parameter equal to -1.0. 88

Figure A. 4. Distribution of the equivalent plastic strain in the three-dimensional unit cell, for both yield criteria, for the stress triaxiality of 1.5. 89

LIST OF TABLES

Table 2.1. Elastic mechanical properties and Voce law for the AA5352 aluminum alloy. 34

Table 2.2. Elastic mechanical properties and Swift law for the TH330 steel. 34

Table 2.3. Uniaxial tension test data..... 34

Table 2.4. Equal biaxial tension and disk compression test data. 35

Table 2.5. CPB06 and CB2001 anisotropy parameters. 37

Table 2.6. Yield stress ratios $\sigma_\theta^{\mathrm{T}} / \sigma_\theta^{\mathrm{C}}$ for CPB06 yield criterion. 38

Table 2.7. Experimental and numerically predicted equal biaxial tension and disk compression test data..... 39

Table 2.8. Strain-based FLC for the AA5352 aluminum alloy and the TH330 steel. 42

Table 2.9. Stress-based FLC for the AA5352 aluminum alloy and the TH330 steel. 44

Table 3.1. Outline of the algorithm adopted in the numerical implementation of the rupture criterion based on the experimental FLC. 66

Table 3.2. Outline of the algorithm adopted in the numerical implementation of the rupture criterion based on the experimental FLCS. 71

Table A. 1. Hill'48 anisotropy parameters. 86

SIMBOLOGY AND ACRONYMS

Simbology

α - ratio between the major and the minor principal stresses;

β - ratio between the plastic strains, for a linear strain path;

λ - arc angle;

θ - angle measured from RD (circumferential direction);

ε_0 - initial plastic strain;

ε_1 - major strain;

ε_2 - minor strain;

ε_1^{num} - numerically predicted major strain ;

ε_2^{num} - numerically predicted minor strain;

ε_3^u - through-thickness strain in each displacement increment;

$\overline{\varepsilon}_p$ - equivalent plastic strain;

ε_r - deformation along the radial direction;

ε_t - deformation along the thickness direction;

μ - friction coefficient;

ν - Poisson ratio;

$\boldsymbol{\sigma}$ - Cauchy stress tensor;

$\boldsymbol{\sigma}'$ - deviatoric stress tensor;

$\hat{\boldsymbol{\sigma}}$ - Cauchy stress tensor, defined in the material orthotropic frame;

$\overline{\sigma}$ - equivalent stress;

σ_1 - major stress;

σ_2 - minor stress;

σ_1^{num} - numerically predicted major stress;

σ_2^{num} - numerically predicted minor stress;

$\sigma_\theta^{\mathrm{C}}$ - experimental yield stresses in compression, obtained from the uniaxial tests for a specific orientation (θ) with respect to RD;

$\sigma_\theta^{\mathrm{T}}$ - experimental yield stresses in tension, obtained from the uniaxial tests for a specific orientation (θ) with respect to RD;

$\sigma_\theta^{Y_T}$ - yield stress measured with a specimen oriented at an angle θ to the rolling direction;

σ_b - yield stress measured from an equi-biaxial tensile test;

σ^C - yield stress obtained from the uniaxial compression test;

$\sigma_i', \mathrm{i} = 1,...,3$ - principal values of the stress deviator;

σ^T - yield stress obtained from the uniaxial tensile test;

$\boldsymbol{\Sigma}$ - effective stress tensor;

$\sum_{ij}, i, j = 1,2,3$ - effective stress tensor components;

$a_1, \ldots, a_6$ and $b_1, \ldots, b_{11}$ - anisotropy parameters;

a, k, n, A, B, C, C_Y, K, , Y_0 and Y_{sat} - material parameters;

f - void volume fraction;

f^* - effective porosity;

f_c - void volume fraction critical value;

$l_{element}$ - element size;

$n_{elements}$ - number of elements;

p - hydrostatic pressure;

q_1, q_2 and q_3 - adjustment parameters for the GTN model;

r - radial direction;

$\overline{r}$ - averaged r-value

r_θ - uniaxial tension r-value, obtained from the uniaxial tests for a specific orientation (θ) with respect to RD;

r_θ^{C} - uniaxial compression r-value, obtained from the uniaxial tests for a specific orientation (θ) with respect to RD;

r_b - anisotropy coefficient measured from the disk-compression test;

r -value - anisotropy coefficient;

t - thickness direction;

$\dot{t}$ - thinning rate;

t_0 - initial thickness of the sheet metal;

t^u - thickness in each displacement increment;

s - tensor obtained from the linear transformation;

s_1, s_2 and s_3 - principal values of **s**;

$w_{\sigma_\theta^T}$, $w_{\sigma_\theta^C}$, w_{r_θ}, w_{σ_b} - weighting factors;

A - set of parameters associated with the selected yield criterion;

B - constant;

C - constant 4th-order tensor;

E - Young's modulus;

J_2 - second invariant of the deviatoric stress tensor;

J_2^0 - second invariant of the effective stress;

J_3^0 - third invariant of the effective stress;

P_{zone_i} - perimeter of the zone i;

R - smallest radius of the die;

V_{void} - volume of the void;

V_{RVE} - volume of the representative element.

Y - flow stress;

Acronyms

3D – Three dimensions;

AA5352 – Aluminum alloy 5352;

ASCII – American standard for information interchange;

CB2001 – Cazaku, Barlat, 2001 yield criterion;

CPB06 – Cazaku, Plunkett and Barlat, 2006 yield criterion;

DD – Diagonal direction;

DD3IMP – Deep drawing 3D implicit;

DD3LT - Deep drawing 3D learning and teaching;

DD3MAT – Deep drawing 3D materials;

DD3OSS – Deep drawing 3D one step springback;

DD3TRIM – Deep drawing 3D trimming;

DIC – Digital image correlation;

FEA – Finite element analysis;

FFL – Forming limit line;

FLC – Forming limit curve;

GP - Gauss point;

GTN – Gurson, Tvergaard and Needleman model;

HAH - Homogeneous-yield-function-based anisotropic hardening;

HCP – Hexagonal close packing metals;

Hill'48 – Hill 1948 yield criterion;

ODF – Orientation distribution function;

ND – Normal direction;

PEPS – Polar effective plastic strain;

RD – Rolling direction;

SD – Strength differential effects;

SFFL – Shear fracture forming limit line;

SRI – Selective reduced integration technique;

TD – Transverse direction;

TH330 – Unstoved steel 330;

Yld 91 – Barlat et *al*. 1991 yield criterion.

1. INTRODUCTION

1.1. Background

Sheet metal forming is a metalworking process which consists in giving a desired shape to metal parts and objects by introducing plastic deformation. A metal sheet has a high surface area to volume ratio, which is obtained through a series of mechanical processes like rolling. Different types of sheet metal forming processes include bending, shearing, tensile forming and combined tensile and compressive forming. The last category of forming processes referred involves operations where the plastic deformation is caused by both tensile and compressive loads. The tensile forming processes take place when the deformation is caused by uniaxial or multiaxial tensile stress, like the extending by stretching, stretch forming, hydroforming and expansion processes. This last operation usually involves two different tools: an expansion punch and a cup support tool.

The stamping process typically combines both tensile and compressive loads, where a thin metal sheet, initially flat, is drawn into a forming die by the mechanical action of a punch. The process is considered a deep drawing when the depth of the drawn part exceeds its diameter. Typically, the stamping process involves three different tools: a punch, a die and a blank-holder. The blank sheet is initially placed between the die and the blank-holder, followed by imposing a pre-defined force to the blank-holder (Step 1 in Figure 1.1). Next, the punch moves vertically upwards or downwards depending on the process definition, giving to the sheet metal blank the shape determined by the die (Steps 2, 3 and 4 in Figure 1.1).

The deep drawing process is a suitable operation to produce cans. These are containers of foods, beverages, oil or chemicals. Therefore, many industries are interested in can's manufacturing. Although those containers are also manufactured with ceramics and plastics, aluminum and steel cans are particularly popular, considering safety and manufacturing costs. There are two types of metal cans: three-piece (Figure 1.2 (a)) and two-piece cans (Figure 1.2 (b)). The first one has two ends: lower and upper ends, while the second has a body and only one end. Drawing and ironing processes are typically required to make the two-piece can, being that the knowledge of the materials' plastic

behaviour is very important for the success of the forming operation, since the optimization of the process parameters is directly dependent on the material mechanical behaviour.

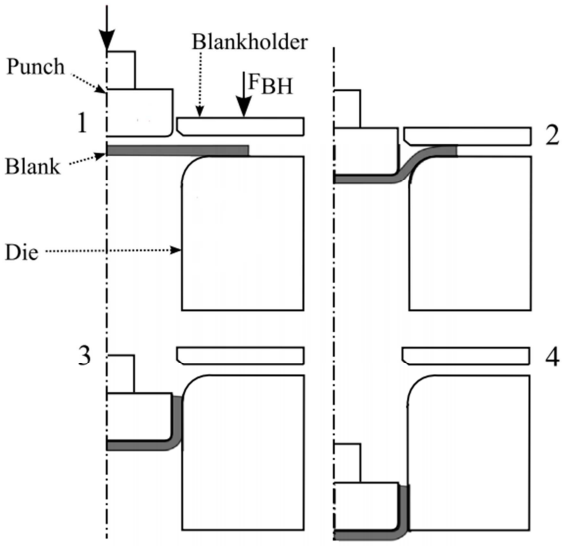

Figure 1.1. Schematic illustration of the stamping process (based on Wallmeier et al., 2015).

(a) (b)

Figure 1.2. (a) Three-piece can (extracted from "http://www.clker.com"); (b) Two-piece can (extracted from "www.meatsandsausages.com").

The forming operation can be considered unsuccessful if the final component presents defects, being responsible for high scrap rates. There are several types of defects, related to the two-piece can:

- Earing profile;
- Excessive thinning;
- Necking;
- Fracture.

Although not relevant in can manufacturing, there are other types of defect, like wrinkling, surface deflection and springback (Tekkaya, 2000).

In the two-piece can making process, an earing profile develops during cylindrical cup drawing and/or redrawing, as an effect of the planar anisotropic properties of the sheet material. This anisotropic behaviour is presented due to the rolling process. The evolution of the earing profile is also dependent on specific lubrication conditions. In the beginning of the 19th century, earing has been noticed in early applications of the rolled metallic sheets for the deep-drawing of cylindrical parts (Vrh et al., 2014). Typically, the number of ears is 4 for steel (Figure 1.3(a)) and 6 or 8 for aluminum cups (Figure 1.3(b)). Several studies have shown the existence of a direct relationship between the number of ears and the variation of the anisotropy coefficient in the plane of the sheet metal (Chung et al., 2011; Yoon et al., 2010).

The ironing operation, which consists in wall thinning, is known to contribute to the earing phenomenon reduction, allowing a more uniform wall thickness of the component as well as increased cup height (Barros et al., 2013). In order to minimize the earing phenomenon, some efforts have been made, like: (i) the optimization of the blank geometry; (ii) other optimization procedures combined with the numerical simulation of the multi-stage forming process (Barlat et al., 1994; Lin & Kwan, 2009); and (iii) as the development of analytical approaches (Yoon et al, 2011).

(a) (b)

Figure 1.3. (a) Earing profile in HSLA steel cup (extracted from Nikhare et al., 2008); (b) Earing profile evolution in an aluminum cylindrical cup (extracted from “http://www.expack.co.uk”).

Excessive thinning is often considered a failure criterion in the metal forming industry. At high-strain, necking or even fracture may develop as a result of excessive structural thinning. Especially in advanced high strength steels, edge cracking may be a significant failure mode in many sheet metal stamping processes (Feistle et al., 2016).

Necking can be considered a macroscopic deformation which causes a decrease in local cross-sectional area. This zone is often designated as "neck". As the local strains in the neck are large, necking is often closely associated with yielding. Thus, this phenomenon usually occurs in ductile materials, metals or polymers. In brittle materials, it is impossible to observe necking, because the fracture occurs without any significant plastic deformation (Dequiedt, 2015). For ductile materials, the beginning of necking is associated with a thickness reduction. Therefore, it is important to analyze the thickness evolution during the forming operations. The onset of the plastic instability can be identified from the strain rate linear fit of the different sections (Volk & Hora, 2010). The same authors proposed a temporal analysis of the thickness strain, ε_3, and the thickness strain rate, $\dot{\varepsilon}_3$ (first derivative of ε_3) along a section perpendicular to the failure region. Two straight lines were fitted along the representative thinning rate evolution, one through the stable deformation zone, and the other through the instable deformation zone (last stage just before necking). The intersection of these lines can be used to define the onset of the plastic instability.

It's very common observing necking in can making processes. Thus, in order to avoid the occurrence of this phenomenon, several approaches are used to define if a process is safe of this defect. The strain-based forming limit curve (FLC) allows knowing when the necking begins, depending on strain conditions. Since deformation is a relatively easy measure to observe, both experimentally and numerically, the majority of practitioners of the sheet metal forming community believe that strain metrics are enough for formability assessment (Stoughton & Yoon, 2012). However, strain metrics are no longer valid when the deformation occurs along non-linear strain paths. In fact, the strain-based FLC represents the maximum admissible strains achievable just before necking $(\varepsilon_1, \varepsilon_2)$ for different types of monotonic loads (Figure 1.4). So, it only allows to get reliable results if the deformation path is linear.

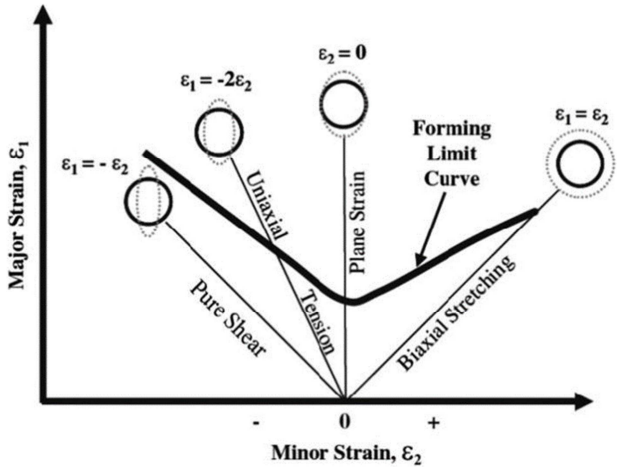

Figure 1.4. Schematic of several tension modes in a strain-based FLD (extracted from Hasan et al., 2011).

One of the alternatives for dealing with strain path changes on the FLC is to consider the stress state based FLC. In fact, the FLC in the stress space is shown to be path-independent and, therefore, it is suitable for the analysis of any forming process (Stoughton & Yoon, 2012). The major disadvantage of these curves is attributed to the reduction of the slope of the true stress-strain relation at large strains, meaning that larger changes in strain occur for similar stress levels, close to the necking limit. In order to remedy this difficulty, same authors prefer the Polar Effective Plastic Strain (PEPS) diagram, as shown in Dick et al., 2015. The PEPS also verifies the strain-path independence. Although this last method seems the most reliable, it is very complex. The main advantages of all these methods are their physical meaning, based on the experimental evidence of the necking process, their lack of mathematical complexity and their independence on the type of test.

Fracture and necking could happen simultaneously. Thus, many authors consider that the FLC for necking is the same as for fracture. As previously mentioned, necking in brittle materials can be considered negligible. However, in ductile materials, there is relevant deformation after the onset of diffuse necking. In fact, experimental results confirmed the existence of two different fracture loci corresponding to crack opening by tension (the fracture forming limit line - FFL) and by in-plane shear (the shear fracture forming limit line - SFFL). So, as shown in Figure 1.5, it has been possible to characterize fracture loci of anisotropic metal sheets under plane stress loading conditions (Isik et al., 2014).

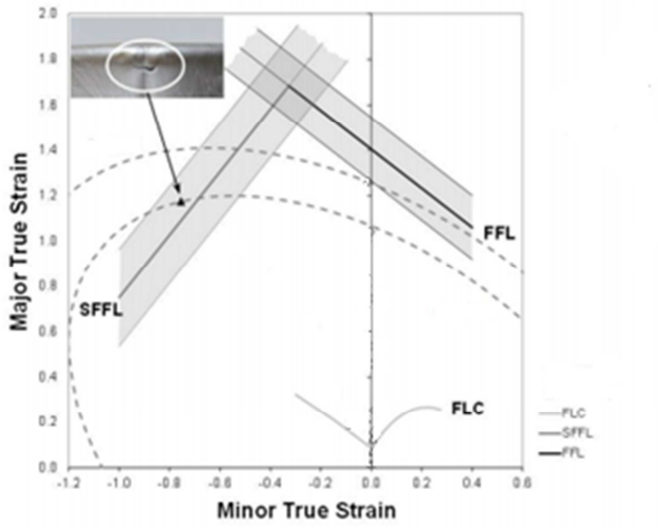

Figure 1.5. Illustration of FFL and SFFL (adapted from Isik et al., 2014).

In order to ensure the processes' safety, the detection of these defects is vital. There are several empirical methods, like X-ray or DIC (digital image correlation), which are very expensive. Thus, numerical simulation emerged as an affordable and quick method to analyze the processes' safety and avoid some of the experimental work. Nowadays, numerical simulation software is used in almost all metal forming processes, including stamping. The development of numerical simulation allows reducing project times and industrialization of new and more complex products. In this context, it is important to refer the automotive industry, which is a very dynamic, active and demanding customer, since it seeks large production volumes and high variety and quality of stamped components (Tekkaya, 2000).

The numerical simulation of sheet metal forming processes requires the description of the material mechanical behavior, which for metallic sheets include the anisotropic plastic behavior. In fact, the grains in polycrystalline materials usually have preferential crystallographic orientations, which define the material texture. Indeed, the texture develops during the rolling processes for sheets, resulting in planar anisotropy. The experimentally measured texture of metal sheets is commonly represented by a three-dimensional crystallite orientation distribution function (ODF). In this context, two major approaches are considered: one based on crystal plasticity and the other based on continuum plasticity. In the first approach, the material is considered as a polycrystalline body and models for its plastic behaviour are used to predict the active slip systems and the

dislocation movement, for each specific loading condition. Thus, this approach is computationally expensive. As a curiosity, Kanetake & Tozawa, 1987 calculated earing in cup drawing based on ODF for steel, aluminum, Mg alloy and copper sheets. More recently, Li et al., 2008 presented the ear profiles in deep cup drawing, obtained using a rate dependent crystal plasticity model.

In the second approach, the material is considered as a homogenous body and the main concept to describe the sheet orthotropic behaviour is the yield surface. The use of this macroscopic approach is less expensive and more practical. Thus, the phenomenological description of plastic deformation in metals is the most commonly used strategy in the numerical simulation of forming processes. This approach considers a yield surface, which corresponds to all stress states for which the plastic deformation begins, and a hardening law, describing the evolution of the yield surface with plastic deformation. Moreover, when using an associated flow rule, the yield surface is used to describe the yielding and the plastic flow of the material. This dual role of the yield surface requires a particular care and accuracy in its modelling. Also, due to the increasingly advanced alloying technologies, the yield surface modelling has become more complex, relaying on an increasing number of material parameters (Barros, 2011).

Numerical simulation enables predicting the punch and blank-holder forces and defects, such as wrinkling, earing, springback, fracture or other instabilities. The phenomenological modeling of the mechanical behavior of the material has an important role in prediction. The currently available software typically provides a wide range of models, which describe almost all the aspects of behavior of materials used in stamping. The most widely used yield criterion is the Hill'48 (Hill, 1948) due to its simplicity. However, it is known for not properly describing the behavior of metallic materials such as aluminum alloys, for which other yield criterion have been proposed, such as the Yld91 (Barlat et al., 1991). Moreover, in order to enable a more detailed description of some materials, such as some aluminum or high strength steels, more complex behavioral models have emerged in this stamping simulation software, such as CB2001 (Cazacu & Barlat, 2001), or for the titanium and magnesium alloys, which present tension-compression asymmetric behavior, the CPB06 (Cazacu, Plunkett, & Barlat, 2006).

To sum up, the numerical simulation of metal forming has assumed a vital role in satisfying the industry needs. In fact, it allows to virtually validate a forming tool,

reducing the number of the experimental tests, time to market for new products and, thus, the costs involved in its development. Nevertheless, there are still challenges to be addressed, particularly in the formability analysis and prediction.

In this context, the NUMISHEET 2016 conference committee proposed a benchmark, named "Failure Prediction after Cup Drawing, Reverse Redrawing and Expansion", with the main objective of predicting the failure point of a food can after drawing, reverse redrawing and expansion operations (Figure 1.6). The NUMISHEET conference and workshop series is specifically devoted to the numerical simulation of sheet metal forming processes. One of the distinctive aspects of NUMISHEET is the proposal of Benchmarks, with the aim of improving the discussion about the different numerical strategies and algorithms that can be applied to the numerical simulation of sheet metal forming processes. It is worth mentioning some of the benchmarks proposed over the last years. The NUMISHEET 2011 benchmark committee proposed a benchmark related to a can making process (Figure 1.7), including drawing and ironing operations, aiming to understand the earing evolution for advanced material modeling. Later, the challenge proposed by the NUMISHEET 2014 benchmark committee (Figure 1.8) was to predict the failure location and timing until fracture point. The main objective was to demonstrate the predictability of forming limits under nonlinear strain paths for a draw panel with a non-axisymmetric reversed dome-shape at the center. Unfortunately, the strain paths observed on the part were almost linear, which limited the discussion. Thus, it is interesting to note that the NUMISHEET 2016 suggests a challenge which combines the earing prediction of a food can, produced using a draw and a redraw operation, followed by the prediction of failure after expansion phase. Therefore, clearly under non-linear strain paths conditions.

Figure 1.6. Numisheet 2016 – Benchmark 1 (extracted from Watson et al., 2016).

Figure 1.7. Numisheet 2011 – Benchmark 1 (extracted from Dick, 2011).

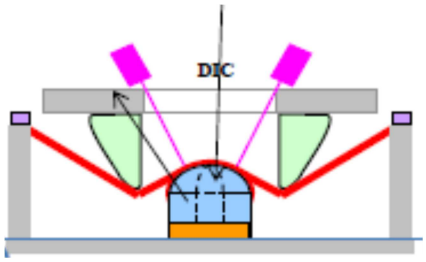

Figure 1.8. Numisheet 2014 - Benchmark 1 (extracted from Du et al., 2013).

1.2. Objectives

The focus of this work is to predict the failure of a can after three stamping processes: drawing, redrawing and expansion, as defined by the NUMISHEET 2016 benchmark committee (Watson et al., 2016). Two different materials are considered: a TH330 steel unstoved (yield strength of 330 MPa), widely used in can making process; and an AA5352 aluminum alloy, which belongs to the 5000 series and it is wrought and magnesium alloyed.

The stamping processes involved pose different challenges for the predictive ability of finite element based solvers, such as thinning and earing, dictated by the plastic anisotropic behavior, and failure, from different strain paths combinations. Therefore, the benchmark committee defined the following objectives:

- prediction of draw, reverse redrawing and expansion punches force evolutions;
- prediction of the earing profile after the reverse drawing operation, highlighting the plastic anisotropy of the material;
- prediction of the thickness profile after the drawing and the reverse redrawing operation;
- prediction of the strain history (Major and Minor principal strains) of the upper surface of the blank as a function of the drawing punch stroke (drawing and reverse redrawing) and the expansion punch stroke;

- prediction of the strain history (Major and Minor principal strains) as a function of punch stroke for the predicted onset failure point.

Thus, these are also the objectives of this work. The NUMISHEET 2016 benchmark committee provided the description of the forming processes, including the tools geometry, and information regarding the materials mechanical behavior. The available information allows the identification of different yield criteria, in order to study their influence in the numerical results. Two yield criteria were selected: the CB2001, which is known for its accurate description of the material anisotropic behavior, and the CPB06, which also enables the description of SD effects.

Moreover, in order to achieve the main objective, corresponding to the failure prediction, a strain-based FLC is provided to the participants, for both materials. Nevertheless, this experimental FLC was obtained for monotonic strain-paths. Therefore, the NUMISHEET 2016 benchmark committee mentions that the participants should use other methods. These can include stress-based FLC's or other strategies based on the thickness strain rate (thinning rate).

In this work, the numerical simulation of all the process was performed using DD3IMP (Deep Drawing 3D IMPlicit) in-house solver, which is known for its robustness and accuracy (Menezes & Teodosiu, 2000).

1.3. Numerical Simulation Software

The DD3 software consists in a main program with several modules focused in specific subjects:

- DD3IMP (Deep Drawing 3D IMPlicit) – sheet metal forming processes simulation;
- DD3TRIM (Deep Drawing 3D TRIMming) –cutting processes simulation;
- DD3OSS (Deep Drawing 3D One Step Springback) –springback simulation;
- DD3MAT (Deep Drawing 3D MATerials) - constitutive laws parameters identification.

- DD3LT (Deep Drawing 3D Learning and Teaching) is an educational software conceived to be used by undergraduate students.

The main program, DD3IMP, is intended for the numerical simulation of the stamping process. Although it was initially developed to simulate this process, it is also possible to use this software in the simulation of other metal forming processes involving plastic deformation. It was developed in Fortran 90/95, using a quasi-static formulation. Large elastoplastic strains and rotations are taken in account in this software. The plastic behavior is described through phenomenogical constitutive models based on the definition of: (i) an associated flow rule; (ii) a yield criterion and (iii) a work-hardening law. There are several yield criteria implemented in DD3IMP, like Hill'48, Yld91, CB2001 or CPB06, as well as different work hardening laws, like Swift, 1947 or Voce, 1948 which can be combined with the kinematic work hardening laws (Frederick & Armstrong, 2007).

The forming tools are assumed as rigid bodies (modeled using parametric surfaces, Bézier or Nagata type), while the frictional contact between the sheet and the tools is described by the Coulomb's classical law. In order to solve the nonlinearities related with the frictional contact problems and the elastoplastic behavior of the deformable body, a fully implicit algorithm Newton-Raphson type algorithm is used. Both nodal displacements and contact forces are involved in the resulting system of nonlinear equations, leading to a mixed formulation. In order to determine an approximate first solution for the nodal displacements, the stress states and frictional contact forces, an explicit approach is used. A $r_{\min}$ strategy is implemented to impose several restrictions on the size of the time increment in order to improve the convergence (Mc-Meeking & Rice, 1975). The first trial solution is iteratively corrected, using a Newton–Raphson algorithm, finishing when a satisfactory equilibrium state in the deformable body is achieved.

The model is defined using ASCII input files with a predefined format, which is commonly adopted in many finite element analysis (FEA) solvers. The standard input files contain the following information:

- DD3_bcon file: boundary conditions;
- DD3_contact file: contact conditions;
- DD3_input file: numerical parameters;
- DD3_mater file: material properties;

- DD3_mesh file: deformable body geometry (blank finite element discretization);
- DD3_phase file: forming process conditions;
- DD3_tool(s) file(s): tools geometry. When using tools described with Nagata patches, IGES files containing the NURBS definition of tools geometry, are also used.

1.4. Reading guide

The structure of this thesis and a brief summary of each chapter are presented in this section.

Chapter 1: shows the importance of sheet metal forming processes in can's manufacturing and how numerical simulation can help in the prediction of defects in that industry. Moreover, the objectives of this study are presented.

Chapter 2: describes the FEA model used in this work. Therefore, the blank sheet discretization, the tool modelling, the constitutive models and methods applied to try to predict the failure point are presented. It includes a detailed description of the CB2001 and CPB06, which are yield criteria used in this work

Chapter 3: discusses the numerical results of all forming operations. It is presented, for each phase, the punch force evolution, the cup height (earing phenomena), the thickness profile at different heights and the strain paths for several points. In order to try to predict the failure point, three methods were used, including strain-based FLC, stress-based FLC and the analysis of the through-thickness strain rate.

Chapter 4: summarizes the main conclusions, including the ones concerning the ability of both yield criteria in predicting the analyzed variables.

2. CUP MULTI-STAGE FORMING: FE MODEL

The efficiency in the can making industry can increase with the prediction of different sheet metal defects and instabilities, like thinning, earing, necking and fracture. Indeed, the numerical simulation of cupping processes is fundamental for this industry. Thus, it strongly depends on the accuracy of the models adopted to represent all forming operations and of some numerical parameters. In addition, the accuracy and flexibility of the models used to describe the material mechanical behavior is also vital.

This chapter describes the main assumptions chosen for performing the multi-stage forming operations of a cup: the blank sheet discretization, the material mechanical behavior and the description of failure prediction methods adopted.

2.1. Blank sheet discretization

The blank sheet is circular in shape with a diameter of 162.9664[1] mm. The thickness is 0.279 mm for the AA5352 and 0.270 mm for the TH330. Due to geometrical and material symmetries, only a quarter of the global structure is modelled. The blank sheet is discretized with 3D 8-node hexahedral finite elements, allowing an accurate evaluation of the contact forces and the through-thickness stress gradients, combined with a selective reduced integration technique (SRI) (Alves, 2003).

In order to achieve minimum reasonable description of the blank, some empirical principles are used. It is worth noting that the springback is negligible, since the component is constrained (axisymmetric conditions). For a correct prediction of the punch force, at least one element should be used to describe an arc length corresponding to $\gamma = 10^{\circ}$, taking into account the smallest tool radius where the metal flows (Li et al., 2002). In this work, an arc length corresponding to $\gamma = 9^{\circ}$ is used. Thus, the element size is determined as:

[1] The original values are defined in inches. However, for the benchmark they were all converted to the International System of Units.

$$l_{element} = \frac{\gamma \times \pi}{180} \times R \tag{2.1}$$

where R is the smallest die radius (radial direction).

Figure 2.1 shows the blank sheet geometry and its division in two regions, defined based on the fact that in zone 1 there is no significant plastic deformation, in both draw and redrawing operations, since the base of both punches operates in this area. Therefore, zone (1) is defined from the origin to a radius of 36 mm and an unstructured mesh will be used, in order to enable a reduction in the total number of elements. As a consequence, the computation time decreases. The remaining zone (2) was defined with a structured mesh. This 2D geometry was initially meshed with quadrilateral elements. Afterwards, the Bi2Tri code was applied to build the 3D mesh, in order to guarantee that, in the final mesh, the elements are organized by layers[2].

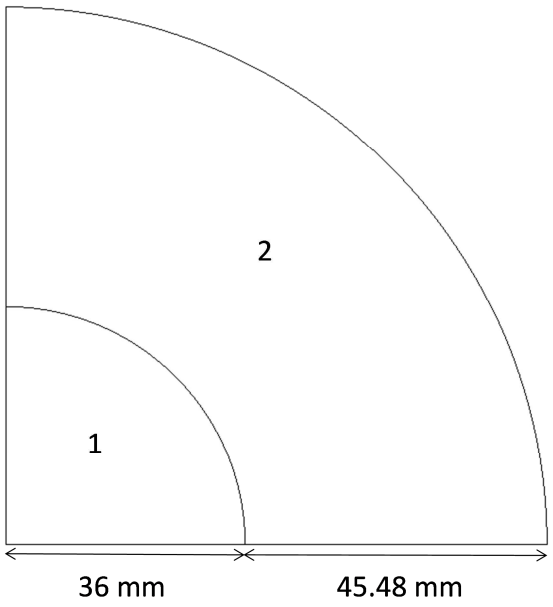

Figure 2.1. In-plane: definition of different regions in the blank.

To obtain the recommended number of elements in the radial direction, it is important to define the required element size. Considering Equation (2.1) and taking into

[2] The first versions of the "Benchmark General Instructions" included a trimming stage after the drawing and redrawing operations. In order to be able to use DD3TRIM code, to perform the trimming operations, it is mandatory that the finite element mesh is organized by layers through the thickness.

account that the smallest shoulder radius of the different dies involved in the process is of 2.54 mm, the minimum element size correspond to 0.399 mm.
Therefore, in zone 2, the empirical minimum number of elements in the radial direction is defined as:

$$n_{elements} = \frac{(81.4832 - 36)}{0.399} = 113.998 \cong 115 \tag{2.2}$$

For the circumferential direction, the main goal is to try to obtain square elements in the structured zone at the end of the drawing and redrawing stage, in order to minimize the influence of the finite element ratio in the expansion stage. Therefore, the size of the element in the circumferential direction must be the same as the previous one, i.e., $l_{element} = 0.399$ mm. In order to estimate the number of elements in the circumferential direction, the minimum radius of the base of the different punches involved in the process is considered, i.e. 43.926 mm. Taking this value as reference it is possible to evaluate the perimeter of the cup at the end of the redrawing phase:

$$P_{zone} = \frac{43.926 \times \pi}{2} = 69 \text{ mm} \tag{2.3}$$

Hence, it is possible to determine the number of elements along the circumferential direction as:

$$n_{elements} = \frac{69}{0.399} = 172 \cong 180 \tag{2.4}$$

Based on this analysis, although the elements located in the periphery are rectangular in the beginning of the process, it is expected that these elements become squarer during the forming process. At this point, it should be mentioned that using 115 elements along the radial direction and 180 along the circumferential, the structured zone presents 20700 square finite elements.

In the thickness direction, only 2 elements are chosen, since it is the minimum required for an accurate thickness prediction. The use of more elements would increase the computational time and since the springback is negligible, it is not expected to have any impact in the results accuracy. Nevertheless, using the previously stablished discretization

would lead to more than 50000 solid finite elements. Therefore, in order to achieve a better compromise between results accuracy and computational time, the discretization in the circumferential direction was strongly reduced. Thus, the number of elements considered in this direction was only 45, as shown in Figure 2.2. In the other directions, the discretization remains equal. The final mesh presents a total number of 11552 solid elements[3].

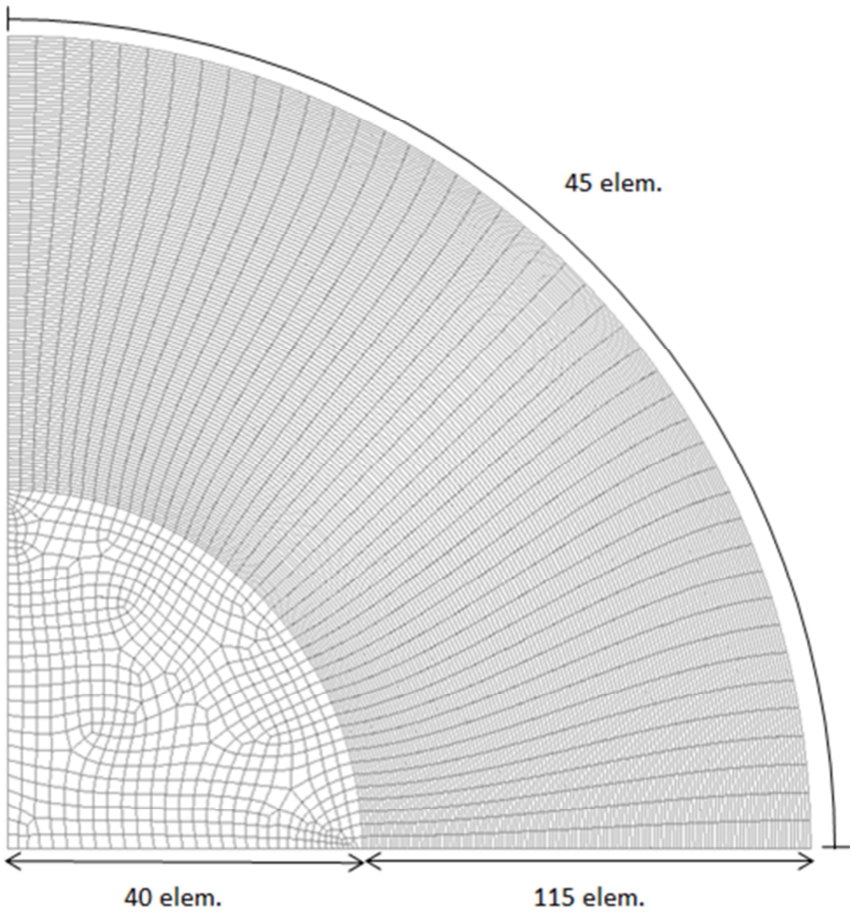

Figure 2.2. Final blank: in-plane discretization.

2.2. Process and tool modelling

The tools for the drawing and redrawing operations consist in a pressure-pad (also known as blank-holder), a die and a punch. All the tools have the same dimensions for both materials. The drawing and redrawing operations are performed considering a constant pressure-pad force, which is also equal for both materials. The contact with

[3] All numerical simulations were performed in a computer machine equipped with an Intel ® Core ™ i7 – 2600K Quad-Core (3.4 GHz) and Windows 7 Professional (64 bits platform) operating system. Typically, the total CPU time was approximately 13 hours for the aluminum alloy and 22 hours for the steel.

friction conditions is described by Coulomb's law, using a constant friction coefficient, μ, of 0.03.

All forming tools are considered rigid and are modelled using Nagata patches (Neto, 2014), which result from the surface smoothing procedure applied to a coarse finite element mesh. Therefore, the following sections show the tools modelling and discretization, for each forming operation. It is worth noting that only the parts of the tools in contact with the metal sheet are modelled. Furthermore, the tools' mesh in the bending radius zones needs to be more refined, in order to keep the geometrical error, attained by the Nagata patches, within acceptable tolerances.

2.2.1. Drawing operation

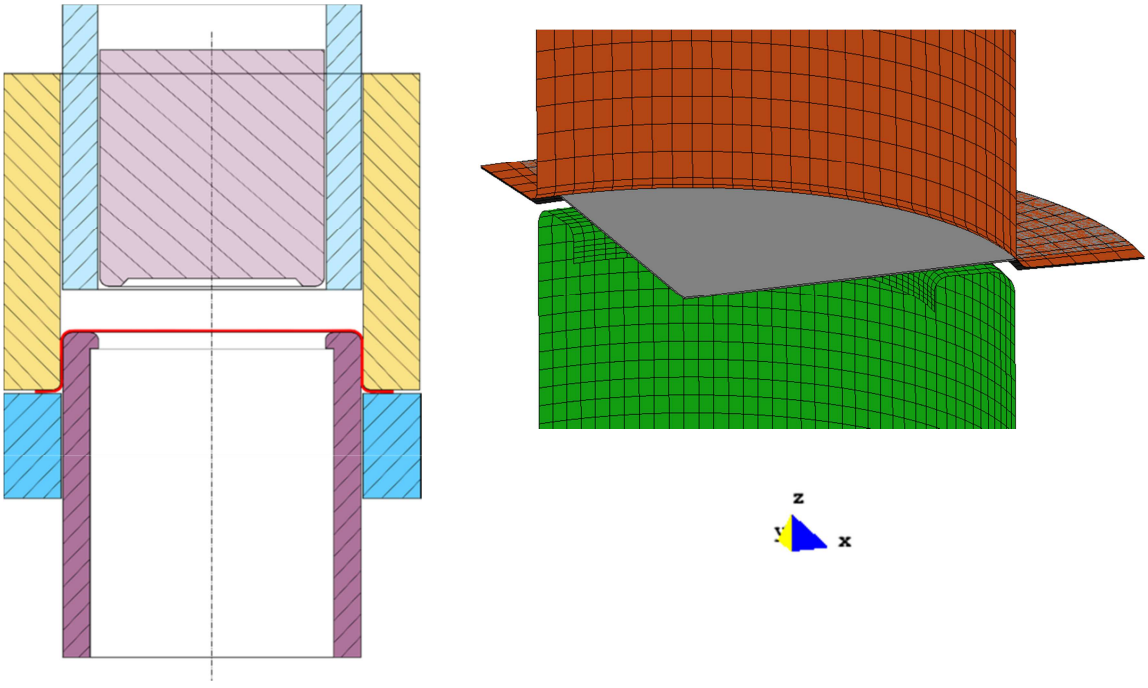

(a) (b)

Figure 2.3. Drawing operation: (a) concept (b) model.

The schematic of the cup drawing process, together with the tools, is shown in Figure 2.3. In this figure, the axis system used in all forming operations is also shown.

Figure 2.4 shows the punch for the drawing operation, which promotes the movement of the blank into the die cavity, as it moves upward. The die for the drawing operation is shown in Figure 2.5. Finally, the pressure-pad for the first stage is presented in Figure 2.6. Its function consists in controlling the flow of the blank into the die cavity, avoiding excessive vertical movement, by pressing the sheet metal against the die. The pressure-pad force is 5275 N for a quarter model. Figure 2.7 shows the cup shape, after the drawing operation, for the aluminum cup. The shape of the steel cup, although not shown, is very similar.

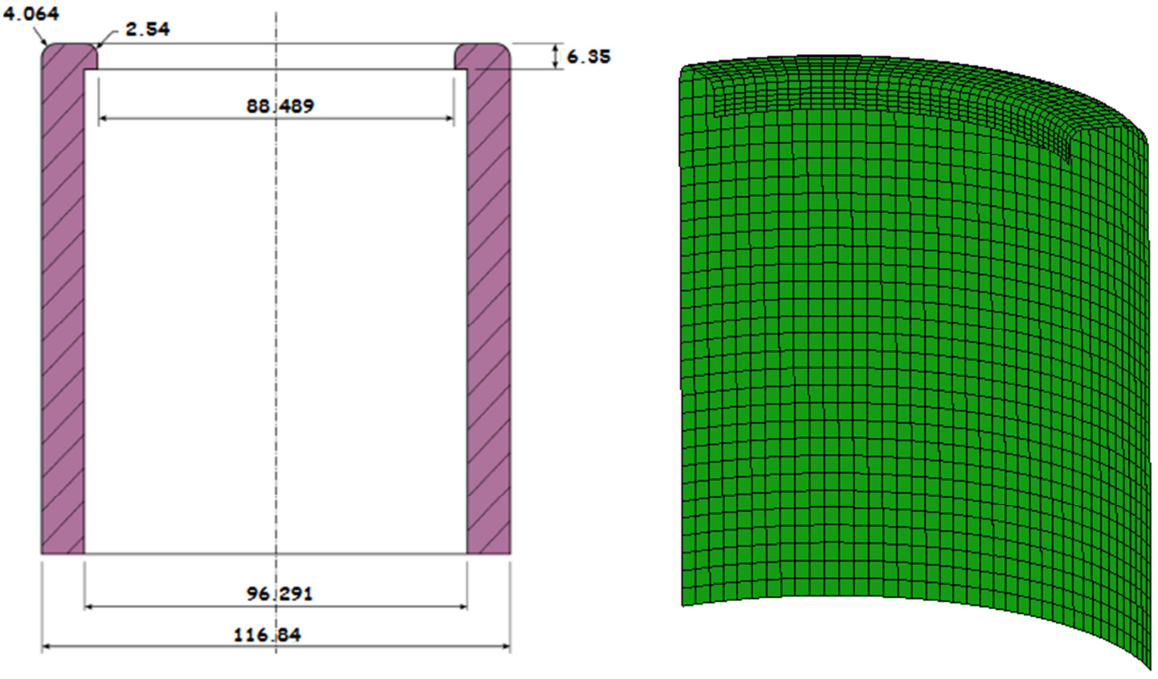

(a) (b)

Figure 2.4. Drawing operation – Punch 1: (a) concept (b) model.

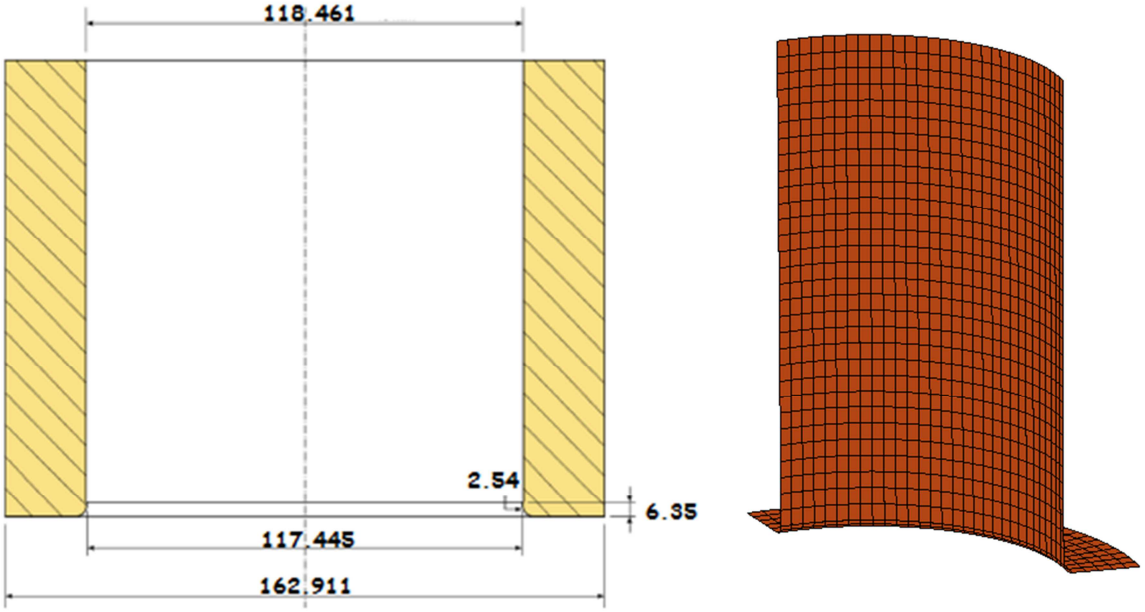

(a) (b)

Figure 2.5. Drawing operation – Die 1: (a) concept (b) model.

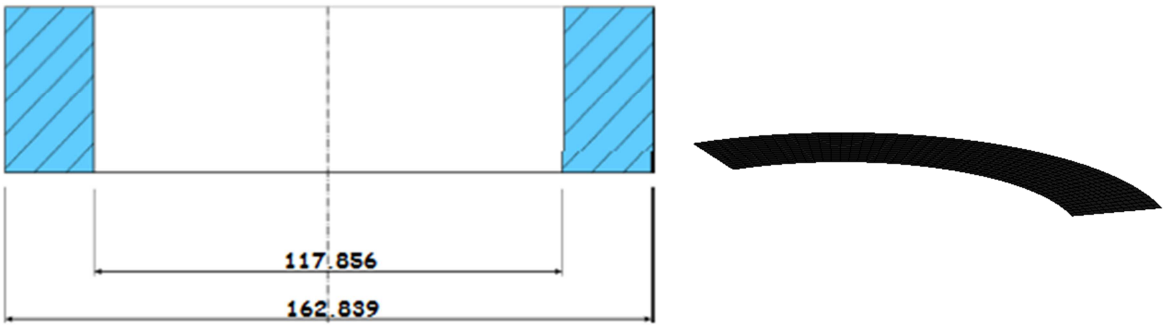

(a) (b)

Figure 2.6. Drawing operation – Pressure-pad 1: (a) concept (b) model.

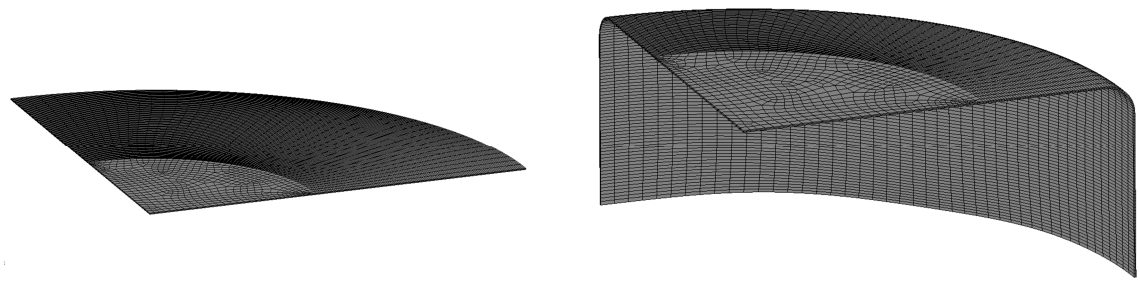

(a) (b)

Figure 2.7. Drawing operation – Aluminum cup: (a) Before drawing (b) After drawing.

2.2.2. Reverse redrawing operation

After the cup is fully drawn, the reverse redrawing operation begins. Figure 2.8 shows a schematic representation of the tools used in this stage, indicating the position of the cup, at the beginning of the redrawing operation. Figure 2.9 presents the punch for the redrawing operation, which now moves downward. The punch for the first phase acts now as the reverse redrawing die (see Figure 2.4). The pressure-pad for the redrawing operation is shown in Figure 2.10. The pressure-pad load for this stage is 4150 N, for a quarter model. It should be mentioned that this tool presents details with small radii, which were not taken into account in the blank sheet discretization, since there is no material flow on those locations. Moreover, as shown in the detail in Figure 2.10 (b), a small fillet was added to avoid convergence problems when the outer-flange of the material arrives at this location. Figure 2.11 (b) shows the aluminum cup at the end of the redrawing operation, showing that the earing phenomenon, which is more visible in the aluminum cup, is now evident.

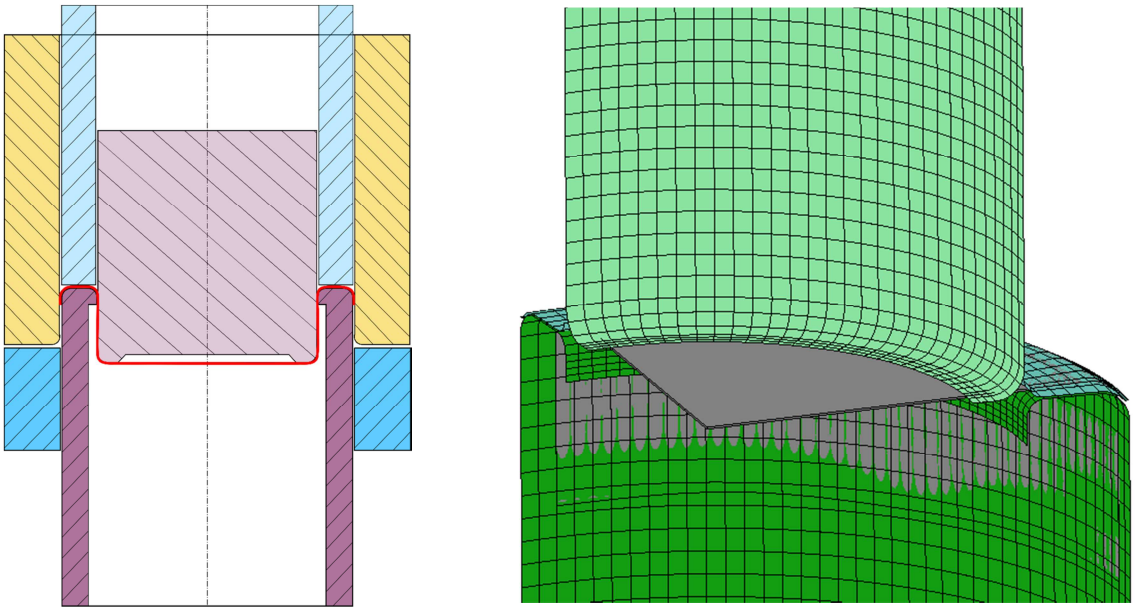

(a) (b)

Figure 2.8. Redrawing operation: (a) concept (b) model.

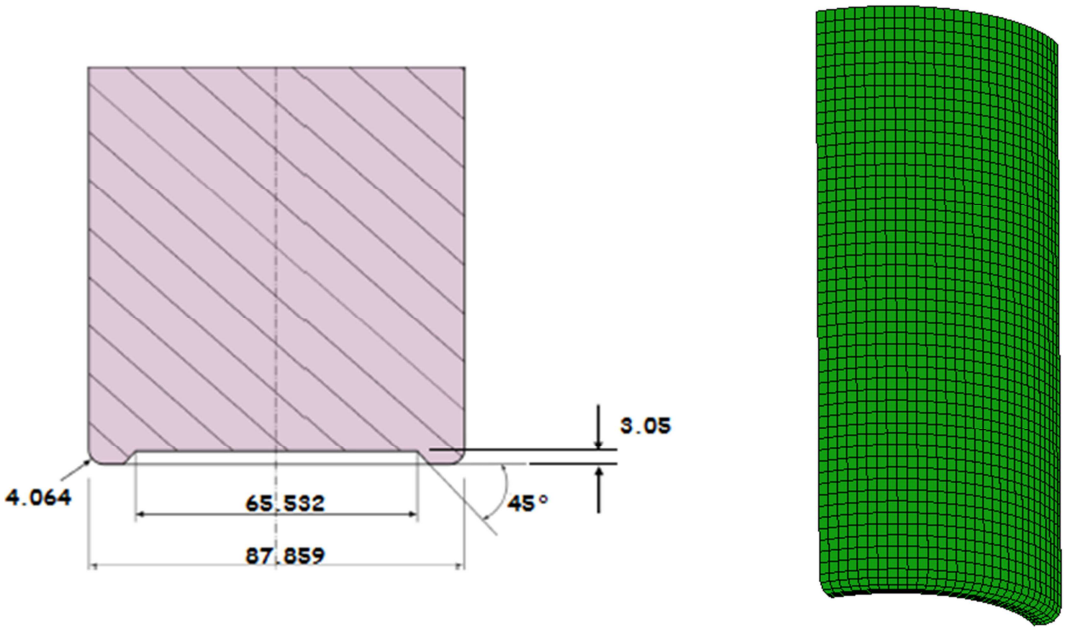

(a) (b)

Figure 2.9. Redrawing operation – Punch 2: (a) concept (b) model.

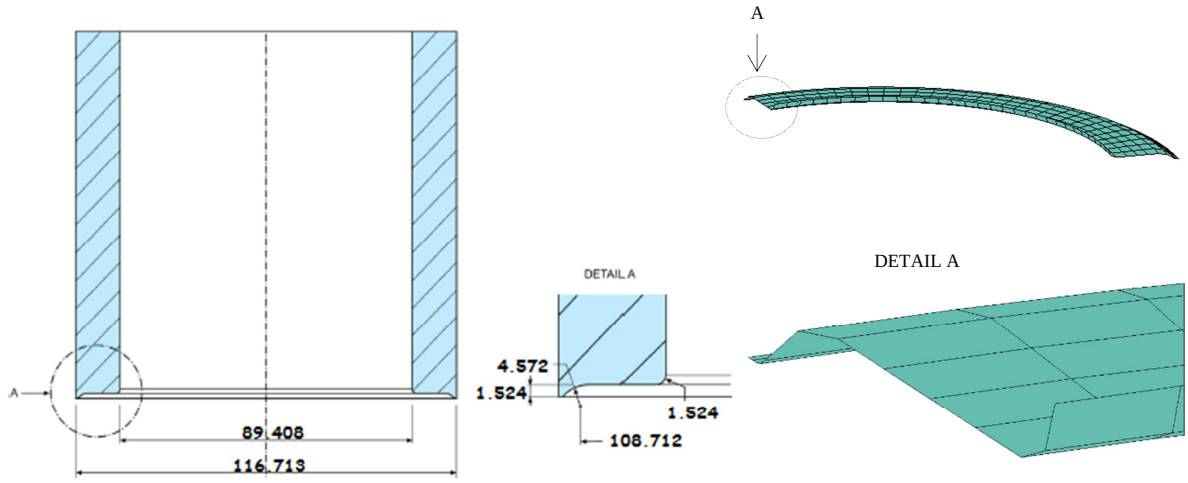

(a) (b)

Figure 2.10. Redrawing operation – Pressure-pad 2: (a) concept (b) model.

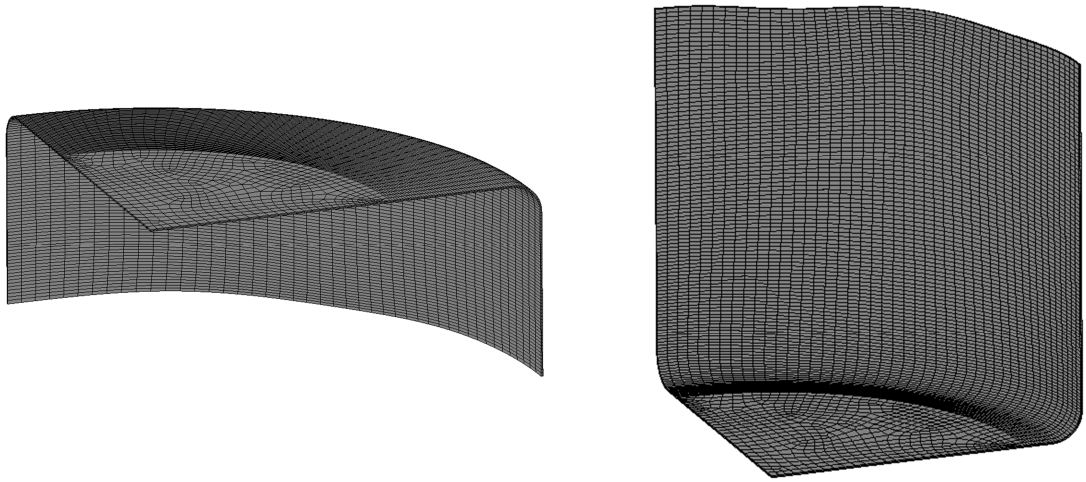

(a) (b)

Figure 2.11. Redrawing operation – Aluminum cup: (a) Before redrawing (b) After redrawing.

2.2.3. Expansion operation

The "Benchmark General Instructions" suffered several revisions, concerning the definition of the tools for the expansion operation. The first version considered that the cup should be simply positioned in a horizontal plane, and different expansion punches were used for each material. Later, a cup support tool was added to this definition. Nevertheless, as shown in Figure 2.12 for the steel cup, the support tool is unable to eliminate the instability problems that occur in the bottom of the cup, causing its wrinkling and a corresponding height decrease.

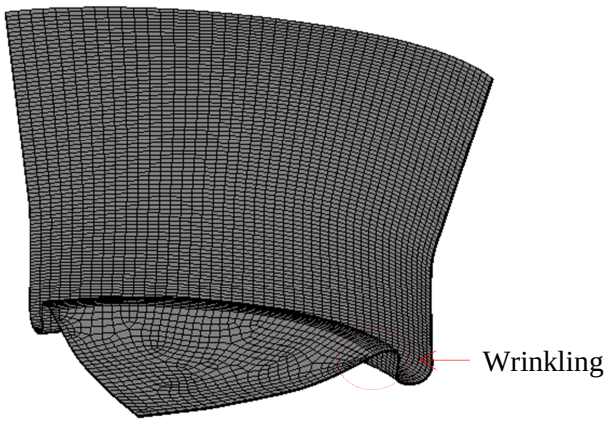

Figure 2.12. Expansion operation without clamp for steel TH330 showing the wrinkling effect.

The final version of the expansion operation considers only one expansion punch, the clamp and the cup support. Moreover, the "Benchmark General Instructions"

states that each participant shall decide how to define the numerical boundary conditions representing the experimental clamping conditions. In this work, the clamp was moved until a fixed distance from the cup support, which was kept constant during the expansion stage. The distance between the clamp and the cup support was determined in order to avoid any deformation during that stage. Figure 2.13 shows a schematic of this process together with the respective tools. It should be noted that the hole in the center of the clamp is not modelled, since the hole in the cup was also not modelled. Figure 2.14 shows the expansion punch, which moves downwards until failure occurs. The cup sits in the cup support tool. Note, once again, that only the parts in contact with the cup are modelled, as shown in Figure 2.15. Finally, Figure 2.16 shows the clamp plate, which was also modelled without the hole. Figure 2.17 shows the aluminum cup before and at the moment identified as the onset failure point.

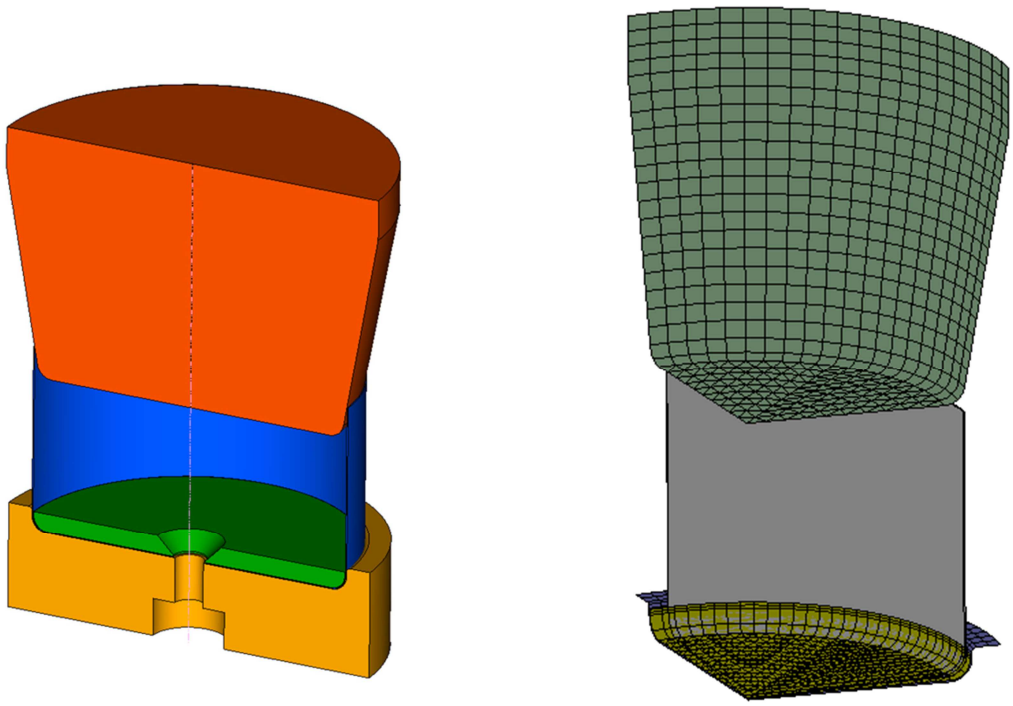

(a) (b)

Figure 2.13. Expansion operation: (a) concept (b) model.

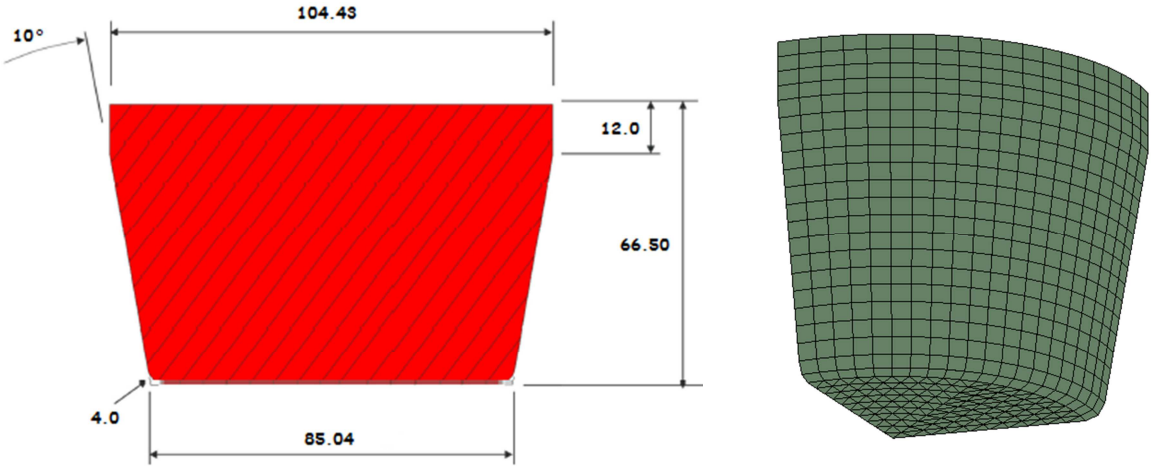

(a) (b)

Figure 2.14. Expansion operation – Punch 3: (a) concept (b) model.

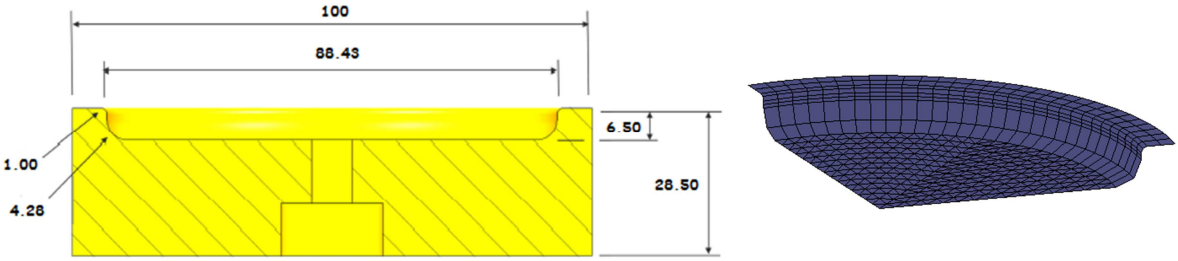

(a) (b)

Figure 2.15. Expansion operation – Cup support: (a) concept (b) model.

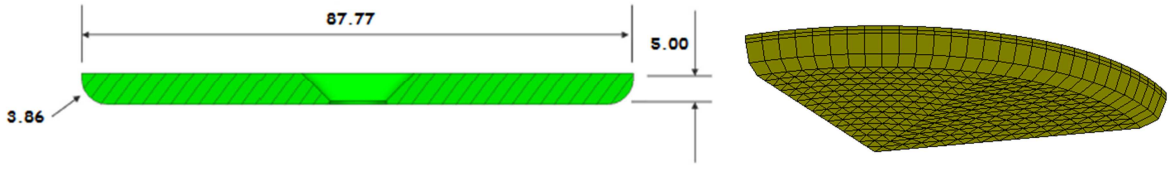

(a) (b)

Figure 2.16. Expansion operation – Clamp: (a) concept (b) model.

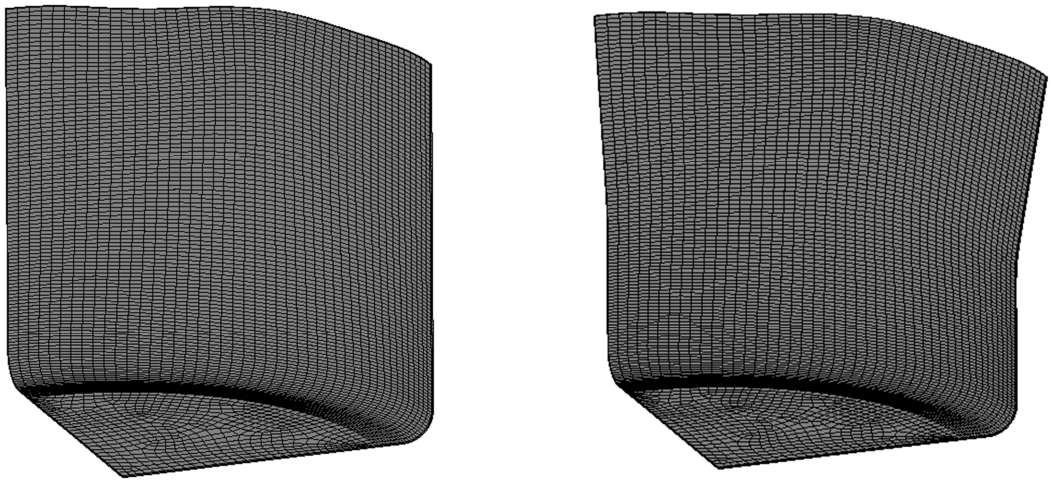

(a) (b)

Figure 2.17. Expansion operation – Aluminum cup: (a) before expansion (b) after expansion (until failure).

2.2.4. Discussion

Several simulations were performed, in order to fine-tune the model. Many parameters were changed from one simulation to another. The more relevant details concern:

- The limits imposed to the vertical movement of the two pressure-pads, in order to avoid excessive ironing of the flange;
- The use of a glue tool throughout the simulation, guaranteeing the control of the metal sheet in the change of phases.

2.3. Material mechanical behaviour

The constitutive model adopted is one of the most important aspects in sheet metal forming simulations. The hardening law describes the evolution of the yield surface being both essential to understand the mechanical behavior of metallic materials when subjected to different strain paths and deformations.

As previously mentioned in Chapter 1, in order to describe the yield surface evolution, there are two approaches: based on microstructural crystal structure or on the macroscopic observation of the material behavior. However, the models based on the first approach require a prohibitive computational effort, for complex shaped components.

Therefore, numerical simulation solvers use models based on the phenomenological approach.

In this chapter, the phenomenological laws used in this work are introduced, in particular, the yield criteria (Section 2.3.1) and the hardening laws (Section 2.3.2). Finally, the experimental characterization and the constitutive parameters identification for the AA5352 aluminum alloy and TH330 steel are presented.

2.3.1. Yield criteria

The yield criteria considered in this work are the CB2001 and the CPB06. These were chosen since the CB2001 yield criterion can lead to an accurate description of the anisotropic behaviour of metallic sheets, presenting a high number of anisotropy parameters, making it quite flexible. On other hand, CPB06 yield criterion is able to describe both the in-plane anisotropy and also the tension–compression asymmetry. In the following sections, a brief summary of both yield criteria is presented.

2.3.1.1. CB2001

The Cazacu & Barlat, 2001 yield criterion is known as a very flexible yield criterion, suitable for predicting the behavior of highly anisotropic materials. The CB2001 is a generalization of the Drucker's isotropic criterion to orthotropy, and, in its general form, is given by:

$$\bar{\sigma} = \left\{ 27 \left[\left(J_2^0 \right)^3 - c \left(J_3^0 \right)^2 \right] \right\}^{\frac{1}{6}}, \tag{2.5}$$

where J_2^0 and J_3^0 are the second and third generalized invariants of the effective stress tensor $\boldsymbol{\Sigma}$, respectively, defined as:

$$\begin{aligned} J_2^0 = {} & \frac{a_1}{6}\left(\Sigma_{11}-\Sigma_{22}\right)^2 + \frac{a_2}{6}\left(\Sigma_{11}-\Sigma_{33}\right)^2 + \frac{a_3}{6}\left(\Sigma_{11}-\Sigma_{22}\right)^2 + \frac{a_1}{6}\left(\Sigma_{11}-\Sigma_{33}\right)^2 \\ & + a_4 \Sigma_{12}^2 + a_5 \Sigma_{13}^2 + a_6 \Sigma_{23}^2, \end{aligned} \tag{2.6}$$

$$
\begin{aligned}
J_3^0 = {} & (1/27)(b_1+b_2)\Sigma_{11}^3+(1/27)(b_3+b_4)\Sigma_{22}^3 \\
& +(1/27)\left[2(b_1+b_4)-b_2-b_3\right]\Sigma_{33}^3 \\
& -(1/9)(b_1\Sigma_{22}+b_2\Sigma_{33})\Sigma_{11}^2-(1/9)(b_3\Sigma_{33}+b_4\Sigma_{44})\Sigma_{22}^2 \\
& -(1/9)\left[(b_1-b_2+b_4)\Sigma_{11}+(b_1-b_3+b_4)\Sigma_{22}\right]\Sigma_{33}^2 \\
& +(2/9)(b_1+b_4)\Sigma_{11}\Sigma_{22}\Sigma_{33} \\
& -(\Sigma_{13}^2/9)\left[2b_9\Sigma_{22}-b_8\Sigma_{33}-(2b_9+b_8)\Sigma_{11}\right] \\
& -(\Sigma_{12}^2/3)\left[2b_{10}\Sigma_{33}-b_5\Sigma_{22}-(2b_{10}+b_5)\Sigma_{11}\right] \\
& -(\Sigma_{23}^2/3)\left[(b_6-b_7)\Sigma_{11}-b_6\Sigma_{22}-b_7\Sigma_{33}\right]+2b_{11}\Sigma_{12}\Sigma_{23}\Sigma_{13},
\end{aligned}
\tag{2.7}
$$

where c, $a_1, \ldots, a_6$ and $b_1, \ldots, b_{11}$ are the anisotropy parameters, while $\Sigma_{ij}, i, j = 1,2,3$ are the effective stress components defined in the material frame. For metal sheets, the parameters a_5, a_6 and b_k $(k = 6,7,8,9,11)$ cannot be evaluated, thus commonly the corresponding isotropic values are adopted. Thus, CB2001 yield criterion involves 11 anisotropy parameters. Consequently, it requires a high amount of input data obtained from mechanical tests, carried out in different loading modes, particularly in the balanced biaxial strain path. In fact, the input data typically used to accurately calibrate the CB2001 anisotropy parameters involves 7 directional yield stresses and 7 directional r-values determined using uniaxial tensile tests, the balanced biaxial yield stress and the balanced biaxial strain ratio r_b-value. Although for metallic sheets, the anisotropy parameters reduce from 18 to 11, this yield function is flexible enough to enable the accurate description of the in-plane anisotropy of both r-value and flow stresses (or yield stresses).

2.3.1.2. CPB06

Characterization and modeling of the anisotropy and the asymmetric yielding of metals is becoming more advanced. However, the most widely used yield criteria do not capture the behavior of hexagonal close packed (HCP) metals. In fact, metals with HCP crystal structure deform plastically by slip and twinning. As opposed to slip, twinning is a directional shear mechanism: shear in one direction can cause twinning while shear in the

opposite direction cannot. Twinning typically leads to lower initial yield stresses in compression than in tension, known as strength differential (SD) effect. Thus, twinning is the predominant mechanism responsible for SD effects, i.e. tension-compression asymmetry in the plastic behaviour.

Recently, Cazacu & Barlat, 2004, based on results of polycrystalline simulations, have proposed a macroscopic isotropic yield criterion expressed in terms of the invariants of the stress deviator, which is able to capture the asymmetry in yielding between tension and compression. In order to describe both the asymmetry and anisotropy in yielding of alloys sheets, an extension of this criterion to orthotropy was formulated. The biggest disadvantage of this orthotropic yield function is the homogeneity of degree three in stresses. To overcome this limitation, Cazacu et al., 2006 proposed an isotropic yield criterion in which the degree of homogeneity (a) is not fixed. Finally, the isotropic form of this yield criterion was extended to orthotropy to capture simultaneously anisotropy and tension/compression asymmetry. This is achieved applying a fourth-order linear operator on the stress deviator. In this work, the orthotropic form of the CPB06 yield criterion is used.

2.3.1.2.1. Description of asymmetric yielding (isotropic form)

The new isotropic yield criterion was defined as:

$$\left(\left|\sigma_1'\right|-k\sigma_1'\right)^a+\left(\left|\sigma_2'\right|-k\sigma_2'\right)^a+\left(\left|\sigma_3'\right|-k\sigma_3'\right)^a=\bar{\sigma}^a, \tag{2.8}$$

where σ_i', $\mathrm{i}=1,...,3$ are the principal values of the stress deviator, while $\bar{\sigma}$ gives the size of the yield locus and k and a are material parameters. The exponent a represents the degree of homogeneity, which has to be a positive integer greater or equal to 2, in order to guarantee the convexity. In this thesis, it is always used $a=2$. Finally, k allows describing the strength differential effects, given by:

$$k=\frac{1-h}{1+h} \text{ with } h=\left[\frac{2^a-2\left(\frac{\sigma^T}{\sigma^C}\right)^a}{\left(2\frac{\sigma^T}{\sigma^C}\right)^a-2}\right]^{1/a}, \tag{2.9}$$

where $\left(\sigma^T / \sigma^C\right)$ represents the ratio between the yield stress in uniaxial tension and the yield stress in uniaxial compression. It is worth nothing that for any value of $a \geq 2$, if $k = 0$, the response in tension and compression is the same. In particular, for $k = 0$ and $a = 2$, the von Mises yield criterion is recovered.

Figure 2.18 represent the plane stress yield loci corresponding to $a = 2$ and k variable. From this figure, it is possible to conclude two ideas: the higher the ratio between the yield stress in tension and compression (corresponding to higher k), the greater is the departure from the von Mises ellipse (Figure 2.18 (a)). Thus, the yield function represents a triangle with rounded corners for the highest admissible value of k; a change in the sign of k results in a mirror image of the yield surface (Figure 2.18 (b)).

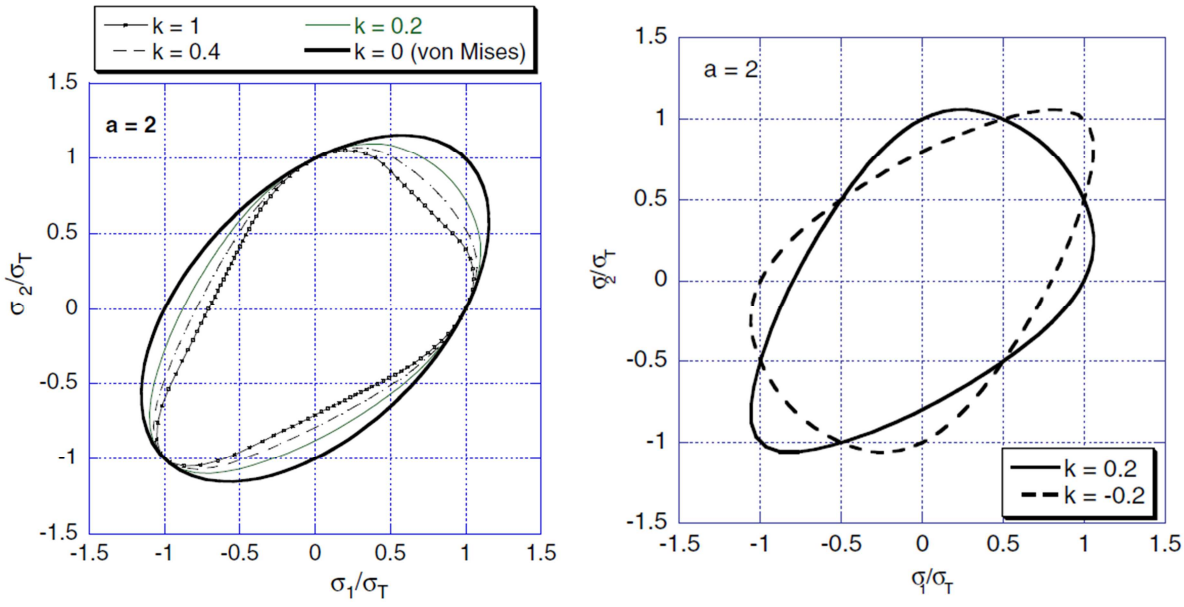

(a) (b)

Figure 2.18. (a) Plane stress yield loci according to CPB06 for different values of the ratio $\left(\sigma^T / \sigma^C\right)$ between the yield stress in tension and compression, in comparison with the von Mises yield locus (b) Plane stress yield loci corresponding to $k = 0.2$ and $k = -0.2$ (extracted from Cazacu et al., 2006).

2.3.1.2.2. Extension of the isotropic yield criterion to include anisotropy

In order to describe both the tension-compression asymmetry and the anisotropy observed in HCP metal sheets, Cazacu et al., 2006 proposed an extension of the proposed isotropic criterion to orthotropy. So, by using a linear transformation on the

deviatoric stress tensor, σ_1', σ_2' and σ_3' are replaced by the principal values of a transformed tensor $\mathbf{s}$ defined as:

$$\mathbf{s} = \mathbf{C} : \boldsymbol{\sigma}', \tag{2.10}$$

where $\mathbf{C}$ is a constant 4th-order tensor. Relative to the orthotropy axes, the tensor $\mathbf{C}$ is represented by (assuming the Voigt notation):

$$\mathbf{C} = \begin{bmatrix} C_{11} & C_{12} & C_{13} & 0 & 0 & 0 \\ C_{12} & C_{22} & C_{23} & 0 & 0 & 0 \\ C_{13} & C_{13} & C_{33} & 0 & 0 & 0 \\ 0 & 0 & 0 & C_{44} & 0 & 0 \\ 0 & 0 & 0 & 0 & C_{55} & 0 \\ 0 & 0 & 0 & 0 & 0 & C_{66} \end{bmatrix}. \tag{2.11}$$

Thus, the anisotropic yield criterion has the form:

$$\bar{\sigma} = B\left[\left(|s_1| - k s_1 \right)^a + \left(|s_2| - k s_2 \right)^a + \left(|s_3| - k s_3 \right)^a \right]^{1/a}, \tag{2.12}$$

where s_1, s_2 and s_3 are the principal values of $\mathbf{s}$. B is a constant defined such that $\bar{\sigma}$ reduces to the tensile yield stress along the rolling direction and defined as:

$$B = \left[\frac{1}{\left(|\phi_1| - k\phi_1 \right)^a + \left(|\phi_2| - k\phi_2 \right)^a + \left(|\phi_3| - k\phi_3 \right)^a} \right]^{1/a}, \tag{2.13}$$

with:

$$\begin{Bmatrix} \phi_1 \\ \phi_2 \\ \phi_3 \end{Bmatrix} = \begin{Bmatrix} (2/3)C_{11} - (1/3)C_{12} - (1/3)C_{13} \\ (2/3)C_{21} - (1/3)C_{22} - (1/3)C_{23} \\ (2/3)C_{31} - (1/3)C_{32} - (1/3)C_{33} \end{Bmatrix}. \tag{2.14}$$

In this anisotropic yield criterion, the physical significance of the k is lost, because it is not possible to define a single $\left(\sigma^T / \sigma^C \right)$ ratio for an anisotropic material. It is worth nothing that convexity is guaranteed for any integer $a \geq 2$ and $k \in [-1,1]$. Once

again, the von Mises can be recovered when $a = 2$, $k = 0$ and $\mathbf{C}$ equal to the 4^{th}- order identity tensor.

2.3.2. Hardening laws

As previously mentioned, the yield surface describes the anisotropy of the metal sheet while the hardening laws, usually isotropic and/or kinematic, describe its evolution. In fact, there are three main modes of yield surface evolution: isotropic expansion, translation and distortion (Alves, 2003) . According to the plasticity theory, the shape and the position of the yield surface are function of the induced changes in texture and microstructure of the material during deformation. It is worth mentioning that it also depends on the loading history. Therefore, the evolution of yield surface is one of the most important characteristics of the modelling of metal sheets plastic behavior.

In sheet metal forming simulation FEA solvers, typically the constitutive models suppose that the yield surface expands (isotropic hardening) and/or eventually translates (kinematic hardening). Figure 2.19 ilustrates a new yield surface, achieved by an uniform expansion of the initial yield surface, defined by yield criterion. Indeed, the centres of the initial and the new yield surfaces remain equal, being the Bauschinger effect neglected. In order to model the Bauschinger effect and similar responses, where a hardening in tension will lead to a softening in a subsequent compression stress state, the use of a kinematic hardening rule is mandatory. In this case the yield surface keeps the initial shape and size and merely translates in stress space, illustrated in Figure 2.19. In order to take into account both the hardening behavior and the change in the flow stress induced by strain path changes, both isotropic and kinematic hardening laws have to be combined.

An alternative approach to represent the effect of a strain path change on the mechanical responses of metallic sheets is the homogeneous-yield-function-based anisotropic hardening, known as HAH model. In this case, the model does not involve the concept of kinematic hardening but rather a novel scheme which comprises the distortion of the yield *loci*. The model is able to explain the most complex hardening responses under reverse loading, like Bauschinger effect, transient hardening and permanent softening (Lee et al., 2015).

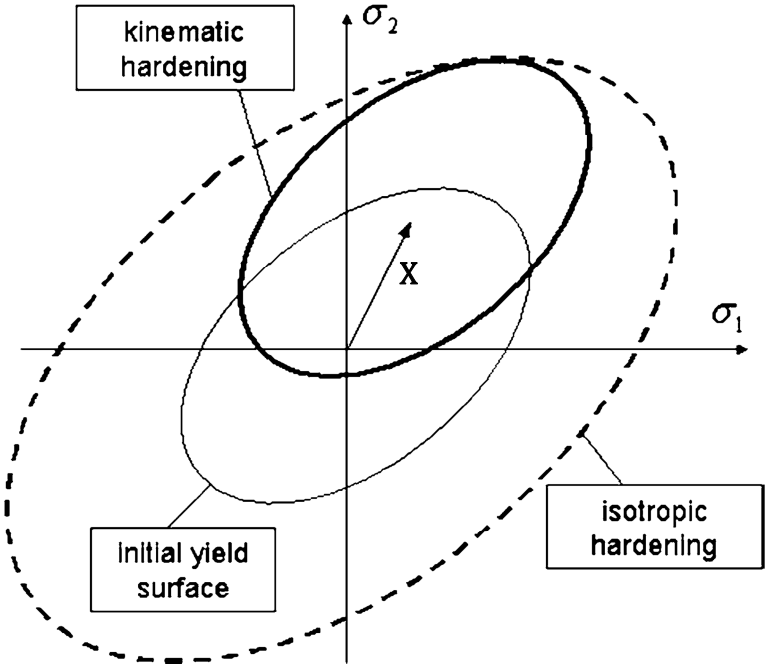

Figure 2.19. Subsequent and initial yield surface with (a) isotropic and (b) kinematic hardening (extracted from Banabic, 2010).

Nevertheless, it must be noted that all these phenomenological models require performing mechanical tests to enable the identification of its parameters. Therefore, to use kinematic hardening laws or more complex models, it is mandatory to perform mechanical tests that involve strain-path changes.

2.3.2.1. Isotropic hardening laws

In sheet metal forming FEA analysis, the Swift and Voce laws are the most used hardening laws. The Swift law describes well the behavior of materials which exhibit isotropic hardening without saturation. Typically, it is suited used to describe the mechanical behavior of steels. The Swift law is given by:

$$Y\left(\bar{\varepsilon}^{\mathrm{p}}\right) = K\left(\varepsilon_0 + \bar{\varepsilon}^{\mathrm{p}}\right)^n, \tag{2.15}$$

where $Y\left(\bar{\varepsilon}^{\mathrm{p}}\right)$ represents the flow stress, $\bar{\varepsilon}^{\mathrm{p}}$ is the equivalent plastic, n is the hardening coefficient, and ε_0 and k are materials parameters.

The Voce law is used to describe the behavior of materials which exhibits isotropic hardening with saturation, like aluminum alloys. This law is given by:

$$Y\left(\bar{\varepsilon}^{\mathrm{p}}\right)=A-B\exp\left(-C\bar{\varepsilon}^{\mathrm{p}}\right) \text{ and} \tag{2.16}$$

$$Y\left(\bar{\varepsilon}^{\mathrm{p}}\right)=Y_0+\left(Y_{\mathrm{sat}}-Y_0\right)\left[1-\exp\left(-C_Y\bar{\varepsilon}^{\mathrm{p}}\right)\right]. \tag{2.17}$$

In Equation (2.16), A, B and C are material parameters. Y_0, Y_{sat} and C_Y are also material parameters, considered in Equation (2.17). The first definition is used by the NUMISHEET 2016 Benchmark committee, while the second form is the one implemented in DD3IMP solver. Both expressions are presented here to highlight the correspondence between the parameters, i.e. $A=Y_{\mathrm{sat}}$, $B=\left(Y_{\mathrm{sat}}-Y_0\right)$ and $C=C_Y$.

2.3.3. Materials characterization

Two materials are considered for this Benchmark: an AA5352 aluminum alloy and a TH330 steel. The material's mechanical behavior is assumed to be isotropic in the elastic regime, being described by the Young's modulus, E, and the Poisson ratio, ν.

Regarding the hardening behavior, the Benchmark committee supplied the parameters for different hardening laws (Swift, Voce, Hollomon and Ludwik), for each uniaxial tensile test performed with the specimen oriented along a direction that makes an angle θ with the rolling direction (RD), between the RD and the transverse direction (TD), for every 15º. Therefore, the plastic behavior is described using a work hardening Voce type law, given by Equation (2.16), and using a work hardening Swift type law, defined as Equation (2.15), for the aluminum and steel, respectively. It should be mentioned that it was decided to identify the material parameters considering the best fit of the 7 hardening curves provided. Table 2.1 and Table 2.2 present the elastic properties and the hardening parameters, for the aluminum alloy and the steel, respectively. Regarding the yield criterion, the Benchmark committee supplied the experimental data for uniaxial tensile tests (yield stress and r-value), the equal biaxial yield stress (σ_b) and the r -value obtained for the disk compression test (r_b), as shown in Table 2.3 and Table 2.4 for both materials.

Table 2.1. Elastic mechanical properties and Voce law for the AA5352 aluminum alloy.

Elastic properties		**Voce law**	
$E\ [MPa]$	68500	A [MPa]	314.53
ν	0.33	B [MPa]	81.74
		C	17.105
		Y_0	232.79

Table 2.2. Elastic mechanical properties and Swift law for the TH330 steel.

Elastic properties		**Swift law**	
E [MPa]	205000	K [MPa]	666.94
ν	0.3	ε_0 [MPa]	0.00775
		n	0.17050
		Y_0	291.21

Table 2.3. Uniaxial tension test data.

	AA532		**TH330**	
Test direction $[^\circ]$	r -value	$\sigma_\theta^{Y_T}$ [MPa]	r -value	$\sigma_\theta^{Y_T}$ [MPa]
0	0.535	197.59	1.4492	258.87
15	0.465	193.39	1.3734	258.25
30	0.655	196.62	1.3012	254.36
45	1.105	193.94	1.2664	255.25
60	1.415	197.03	1.335	251.47
75	1.595	196.89	1.4434	250.33
90	2.27	198.74	1.51	249.42

Table 2.4. Equal biaxial tension and disk compression test data.

AA532	σ_b [MPa]	242.01
	r_b	0.62
TH330	σ_b [MPa]	310
	r_b	0.984

The anisotropy parameters should be determined such that the yield criterion reproduces the material's mechanical behavior as close as possible. The most used experimental results for the identification of anisotropy parameters are the yield stresses and r-values obtained from in-plane tension, for different angles (θ) with the RD. In order to improve the description of the yield surface, it is also recommended to experimentally determine the biaxial yield stress and the biaxial anisotropy coefficient. Therefore, it is possible to confirm that the benchmark committee supplied the recommended data. However, for the CPB06 yield criterion, uniaxial compression experimental results are also necessary for describing the SD effects. However, when performing compression tests for thin metallic sheets it is necessary to avoid buckling effects. This requires the use of small specimens, leading to supplementary difficulties in the acquisition and analysis of experimental results, particularly for high strain values.

The anisotropy parameters for both the CB2001 and the CPB06 yield criteria were determined using the DD3MAT in-house code (Alves et al., 2004; Barros et al., 2016) taking into account the experimental data reported by the benchmark committee. The procedure adopted is based in an optimization problem regarding the minimization of an error function, evaluating the difference between the estimated values and the experimental ones, as follow:

$$F(\mathbf{A}) = \sum_{\theta=0}^{90}\Big[w_{\sigma_\theta^{\mathrm{T}}}\left(\sigma_\theta^{\mathrm{T}}(\mathbf{A})/\sigma_\theta^{\mathrm{T}} - 1\right)^2 + w_{\sigma_\theta^{\mathrm{C}}}\left(\sigma_\theta^{\mathrm{C}}(\mathbf{A})/\sigma_\theta^{\mathrm{C}} - 1\right)^2 + w_{r_\theta}\left(r_\theta(\mathbf{A})/r_\theta - 1\right)^2 \Big], \quad (2.18)$$
$$+ w_{\sigma_b}\left(\sigma_b(\mathbf{A})/\sigma_b - 1\right)^2 + w_{r_b}\left(r_b(\mathbf{A})/r_b - 1\right)^2$$

where $\mathbf{A}$ represents the set of parameters associated with the selected yield criterion. $\sigma_\theta^{\mathrm{T}}$, $\sigma_\theta^{\mathrm{C}}$ and r_θ are the experimental yield stresses in tension, compression and r-values

determined in uniaxial tension, respectively, obtained from the uniaxial tests for a specific orientation (θ) with respect to RD. σ_b is the experimental yield stress obtained from the equibiaxial tensile test, r_b is the experimental r-value obtained from the disc compression test, and, $\sigma_\theta^{\mathrm{T}}(\mathbf{A})$, $\sigma_\theta^{\mathrm{C}}(\mathbf{A})$, $r_\theta(\mathbf{A})$, $\sigma_b(\mathbf{A})$ and $r_b(\mathbf{A})$ are the correspondent values predicted from the adopted yield criterion. Such procedure can be considered a generalization of the one proposed by Banabic et al., 2005. The weighting factors, $w_{\sigma_\theta^{\mathrm{T}}}$, $w_{\sigma_\theta^{\mathrm{C}}}$, w_{r_θ}, w_{σ_b} and w_{r_b} are used to balance the influence of the experimental data. Nevertheless, the selection of the weighting factors is normally a manual procedure, strongly dependent on users' expertise and knowledge. The identification procedure, defined in Equation (2.18), also implies the pre-selection of an initial yield stress or the hardening law parameters, if a specific value of plastic work is defined to select the experimental values for the yield stresses.

In case of the CPB06 yield criterion, since no experimental information regarding the compression yield stresses is available, the σ_b value was used to estimate the SD effect. This procedure is based on the fact that the equibiaxial stress state is equivalent to the through-thickness uniaxial compression (Barros et al., 2015). Nonetheless, it should be mentioned that the σ_b value reported by the Benchmark committee was obtained from a bulge test.

As previously mentioned, parameters a_5, a_6 and b_k $(k=6,7,8,9,11)$ for the CB2001, and C_{44} and C_{55} for the CPB06, cannot be evaluated, since they are related to the off-plane properties. Thus, the corresponding commonly isotropic values are adopted, i.e, 1.0. The anisotropy parameters identified for both materials are shown in Table 2.5, for the CB2001 and the CPB06 yield criteria.

Figure 2.20 shows the evolution of the yield stress with the angle from the RD, for both yield criteria, for the AA5352 and TH330, obtained considering all weighting factors equal to 1.0. Regarding the AA5352 aluminum alloy, the CB2001 presents a better fit than CPB06 for the yield stresses in tension, mainly since it captures the global shape of the evolution. Since CPB06 allows describing the materials' behavior for compression stress states, the evolution is also predicted. The stress ratio is higher than 1 for RD, while for TD is lower, as shown in Table 2.6. As for TH330 steel, the yield stresses evolution is

well described for both yield criteria, with CB2001 being more accurate. Considering the compression yield stresses, the stress ratio is always lower than 1, as presented in Table 2.6.

Table 2.5. CPB06 and CB2001 anisotropy parameters.

	CPB06			**CB2001**	
	AA5352	**TH330**		**AA5352**	**TH330**
C_{11}	0.7704	0.6890	a_1	1.0899	1.3147
C_{22}	1.2732	0.7968	a_2	0.8598	0.9101
C_{33}	2.1750	-0.6023	a_3	1.0647	0.8740
C_{44}	1.0000	1.0000	a_4	0.9802	1.0885
C_{55}	1.0000	1.0000	b_1	2.9498	2.0366
C_{66}	1.3296	0.8560	b_2	0.3230	1.1844
C_{12}	-0.3253	-0.1041	b_3	3.1039	1.0204
C_{13}	-0.3426	-0.1635	b_4	-1.8040	0.8486
C_{23}	0.1305	0.1931	b_5	-1.0546	0.4537
k	-0.4150	-0.1693	b_{10}	0.6584	0.7017
			c	0.9095	0.7902

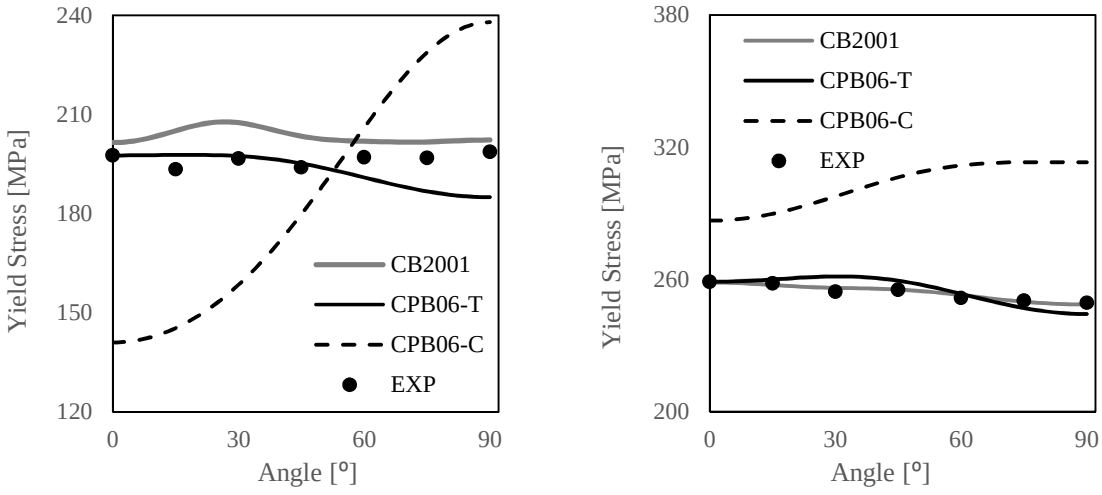

(a) (b)

Figure 2.20. Experimental and predicted yield stresses for (a) AA5352 aluminum alloy and (b) TH330 steel.

Table 2.6. Yield stress ratios $\sigma_\theta^{\mathrm{T}} / \sigma_\theta^{\mathrm{C}}$ for CPB06 yield criterion.

	AA5352	**TH330**
RD	1.40	0.90
TD	0.78	0.78

Figure 2.21 shows the r-values evolution with the angle from the RD, for both yield criteria. For the AA5352 aluminum, CB2001 describes accurately the r-values evolution. For the CPB06, even thought is not flexible enough to describe the inflexion points, the increasing behavior is well described. The r-values predicted with CPB06 for compression are closer to 0 or negative. For the TH330 steel, both yield criteria describe accurately the r-values evolution. The r-values evolution in compression is approximately six times higher than the one in tension, maintaining almost the same shape.

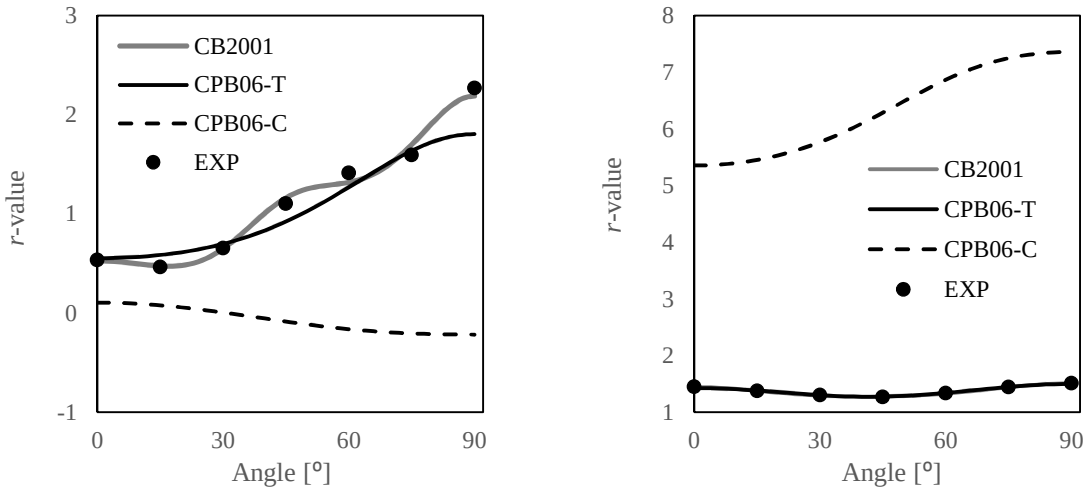

(a) (b)

Figure 2.21. Experimental and predicted r-values for (a) AA5352 aluminum alloy and (b) TH330 steel.

The yield surfaces predicted for the AA5352 aluminum and the TH330 steel for the plane σ_{11}, σ_{22}, with $\sigma_{33} = 0$, are presented in Figure 2.22 (a) and (b), respectively. For the AA5352, the yield surfaces predicted are globally quite different. In the first quadrant, the differences between both yield criteria are more evident for the TD and for the equi-biaxial point. In fact, as shown in Table 2.7, the CPB06 predicts a σ_b value closer to the experimental one. Note that the CB2001 yield criterion presents a point-symmetry from the centre. The CPB06 predicts a lower equi-biaxial compression yield stress, which makes the surface slightly triangular. Since the TH330 steel is quite isotropic, the yield

surfaces predicted for both yield criteria are very similar, except for the third quadrant, where the CPB06 predicts a higher equi-biaxial compression stress.

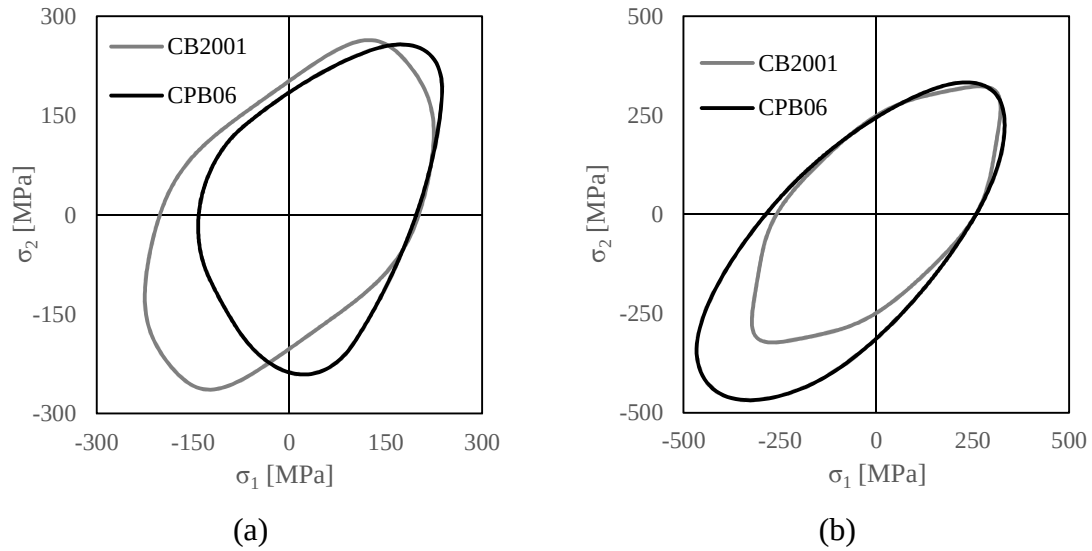

(a) (b)

Figure 2.22. Predicted yield surfaces in the σ_{11}, σ_{22} plane for (a) AA5352 aluminum alloy and (b) TH330 steel.

Table 2.7. Experimental and numerically predicted equal biaxial tension and disk compression test data.

		Exp.	CPB06	CB2001
AA532	σ_b [MPa]	242.01	228.996	203.111
	r_b	0.62	0.553	0.616
TH330	σ_b [MPa]	310	306.799	310.192
	r_b	0.984	0.983	0.984

One of the objectives of this work is the prediction of the earing profile of the cylindrical cup after the drawing and redrawing operations. Previous works indicate that an accurate prediction of both r-values and yield stresses directionalities dictates the ability to predict the earing profile (Yoon et al., 2011). As shown in Figure 2.23, the behavior of the rim in the circumferential direction defined by θ (to the RD) is controlled by the material compression properties, in the direction defined by $\theta+90$. Assuming that the uniaxial tension and compression lead to identical r-values, these can be expressed as a function of the plastic strains at the rim:

$$r_{\theta+90} = \frac{\varepsilon_r}{\varepsilon_t} = -\frac{\varepsilon_r}{\varepsilon_r + \varepsilon_\theta} \tag{2.19}$$

where subscripts r, θ and t correspond to the radial, circumferential and thickness directions, respectively. In Figure 2.23 (a), these properties are equal to the material tension properties, due to its symmetric tension-compression behavior. However, assuming the SD effect, the plastic strains at the rim are controlled by r_θ^C and the stress state by σ_θ^C, as shown in Figure 2.23 (b).

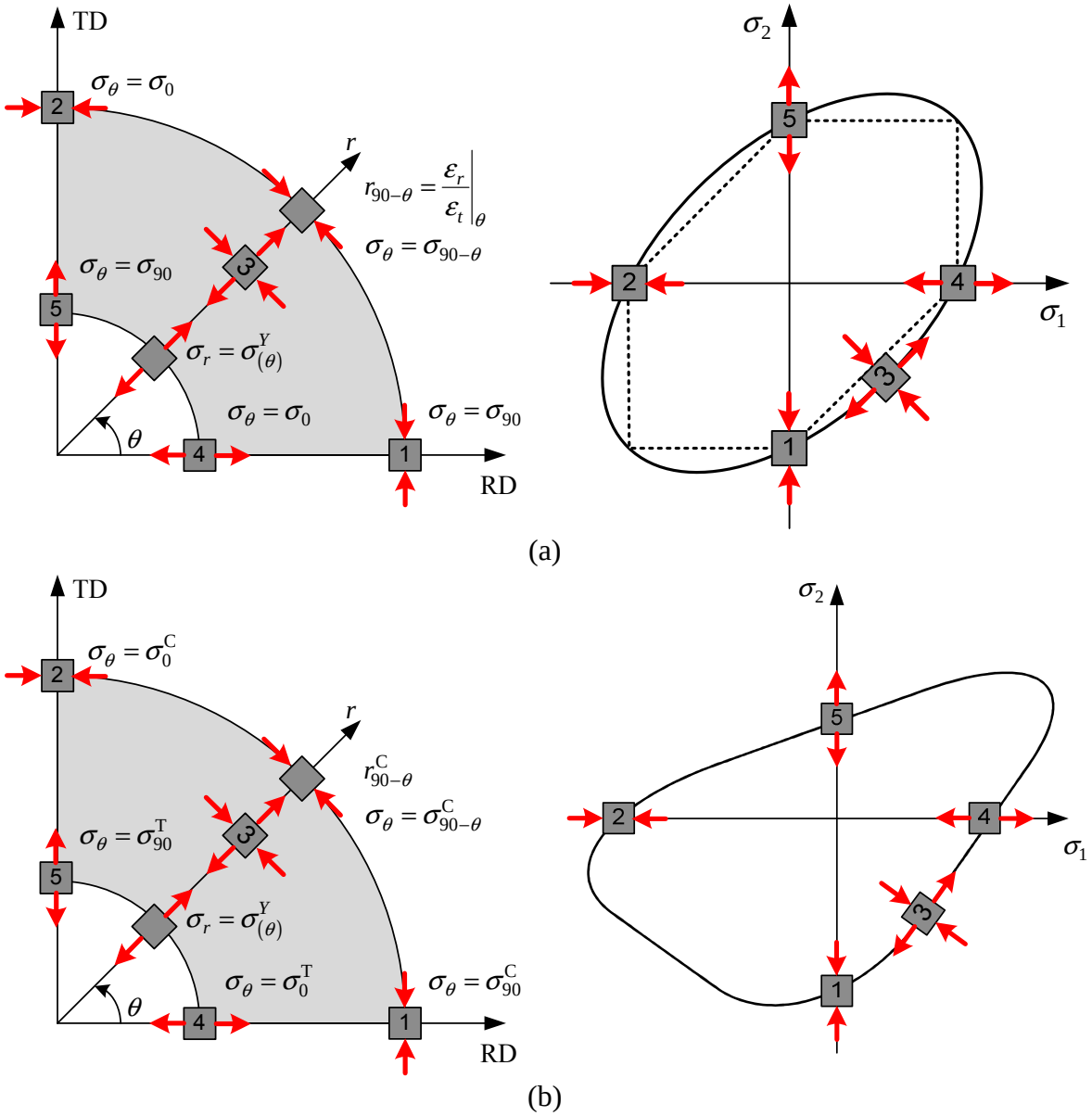

Figure 2.23. Deformation of an element on the flange, stress states on the flange (left) and stress states on the yield surface (right): (a) isotropic material, with symmetric tension-compression behavior; (b) material with asymmetric tension-compression behavior (adapted from Yoon et al., 2011).

2.4. Failure prediction

In order to predict the failure point after the expansion operation, several methods were used, including the strain-based FLC, the stress-based FLC and the analysis of the through-thickness strain rate. In this section, a brief description of these methods, which are based in the post-processing analysis of the results, is given. Moreover, the Gurson-Tvergaard-Needleman (GTN) model was also studied, since it is implemented in DD3IMP code, combined with the CPB06 yield criterion. In this case, in order to be able to predict failure it is necessary to identify the model parameters, for which a procedure has not yet been stablished. Thus, the aim in this case was to try to understand the role of the in-plane anisotropy and the SD effect in the voids evolution.

2.4.1. Strain-based and stress-based FLC

As previously mentioned, the Benchmark committee supplied the strain-based FLC for the aluminum AA5352 and steel TH330. These are based in experimental tests performed under monotonous strain-paths. Therefore, it was expected, since the beginning of this work, that it would not be possible to predict any failure by performing the direct comparison between the numerically predicted major and minor strains and the strain-based FCL. However, the stress-based FLC is independent of the loading history. Therefore, it was decided to study a procedure which allows transforming the strain-based FLC into a stress-based FLC. This procedure is also described in this section.

2.4.1.1. Strain-based FLC

The strain-based FLC data for the AA5352 aluminum alloys and TH330 steel is in Table 2.8. Figure 2.24 presents the corresponding plot in the strain space, highlighting the differences between both materials.

Table 2.8. Strain-based FLC for the AA5352 aluminum alloy and the TH330 steel.

AA5352		TH330	
Major Strain ε_1	**Minor Strain ε_2**	**Major Strain ε_1**	**Minor Strain ε_2**
0.14	-0.038	0.541	-0.270
0.109	-0.012	0.205	0.000
0.09	0.005	0.284	0.213
0.076	0.012	0.310	0.310
0.078	0.026		
0.11	0.092		

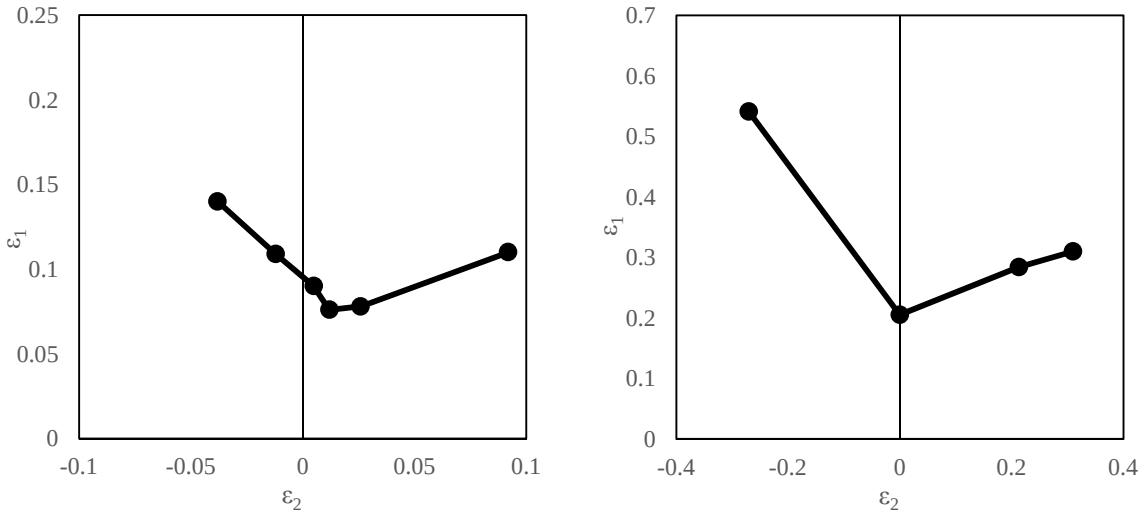

(a) (b)

Figure 2.24. Strain-based FLC for: (a) AA5352 aluminum alloy; (b) TH330 steel.

2.4.1.2. Stress-based FLC

The procedure described in this section is based on the work by Martins et al., 2014 and Dick et al., 2015. The behavior of the forming limit curve in the strain space can be represented by the major strain ε_1 and the ratio between the plastic strains β, such as:

$$\text{strain}-\text{based FLC} = \begin{bmatrix} \varepsilon_1 \\ \varepsilon_2 \end{bmatrix} = \varepsilon_1 \begin{bmatrix} 1 \\ \beta \end{bmatrix}, \tag{2.20}$$

where β is a constant in the range $[-1,1]$. This relation assumes a proportional loading, i.e. a linear strain path. By assuming a proportional loading, it is possible to define the parameter α:

$$\alpha = \frac{\sigma_2}{\sigma_1}, \tag{2.21}$$

where σ_1 and σ_2 are the major and the minor principal stresses. At this stage, it is necessary to select a yield criterion in order to evaluate the equivalent stress. In this case, the Hill'48 yield criterion for normal anisotropy under plane stress conditions $(\sigma_3 = 0)$ is used, which can be written as:

$$\bar{\sigma}(\sigma_1, \sigma_2) = \sqrt{(\sigma_1)^2 + (\sigma_2)^2 - \frac{2\bar{r}}{1+\bar{r}}\sigma_1\sigma_2}\ . \tag{2.22}$$

Taking into account the relation between the major and minor stress states defined in Equation (2.21):

$$\bar{\sigma} = \sigma_1\sqrt{1+\alpha^2 - \frac{2\bar{r}}{1+\bar{r}}\alpha} \Leftrightarrow \frac{\bar{\sigma}}{\sigma_1} = \sqrt{1+\alpha^2 - \frac{2\bar{r}}{1+\bar{r}}\alpha}, \tag{2.23}$$

where $\bar{r}$ represents the averaged r-value. The relation between the major and minor in-plane stresses is obtained by writing the ratio α in terms of the slope β, of the linear strain paths, such as:

$$\alpha = \frac{(1+\bar{r})\beta + \bar{r}}{(1+\bar{r}) + \bar{r}\beta}. \tag{2.24}$$

The equivalent strain increment can also be calculated in terms of the principal strains as:

$$\mathrm{d}\bar{\varepsilon} = \frac{1+\bar{r}}{\sqrt{(1+2\bar{r})}}\sqrt{\mathrm{d}\varepsilon_1{}^2 + \mathrm{d}\varepsilon_2{}^2 + \frac{2\bar{r}}{1+\bar{r}}\mathrm{d}\varepsilon_1\mathrm{d}\varepsilon_2}\ . \tag{2.25}$$

This increment can be used to estimate the equivalent stress. However, this requires the selection of a hardening law. Selecting, for instance, the Voce hardening law (Equation (2.16)), it is possible to determine the major and the minor principal stresses as:

$$\sigma_1 = \frac{\bar{\sigma}}{\sqrt{1+\alpha^2 - \frac{2\bar{r}}{1+\bar{r}}\cdot\alpha}} = \frac{Y_0 + (Y_{sat} - Y_0)\cdot\left[1-\exp\left(-C_y \cdot d\bar{\varepsilon}\right)\right]}{\sqrt{1+\alpha^2 - \frac{2\bar{r}}{1+\bar{r}}\cdot\alpha}}, \quad (2.26)$$

$$\sigma_2 = \sigma_1 \cdot \alpha . \quad (2.27)$$

Thus, it is possible to determine the stress-based forming limit curve for the materials under analysis by applying this procedure. Figure 2.25 shows the data and the stress-based FLC for the AA5352 aluminum alloy and the TH330 steel. However, it should be mentioned that the constitutive model adopted in this procedure should be the same used in the FEA, in order to be able to directly compare the numerically predicted major and minor stresses with the stress-based FLC. In fact, for each constitutive model a different stress-based FLC will be predicted.

Table 2.9. Stress-based FLC for the AA5352 aluminum alloy and the TH330 steel.

AA5352		**TH330**	
Major Stress σ_1 **[MPa]**	**Minor Stress** σ_2 **[MPa]**	**Major Stress** σ_1 **[MPa]**	**Minor Stress** σ_2 **[MPa]**
268.419	70.987	312.579	312.579
273.420	112.819	320.461	185.416
272.351	147.217	321.337	297.728
268.193	163.533	303.227	33.901
264.904	189.217		
251.712	237.190		

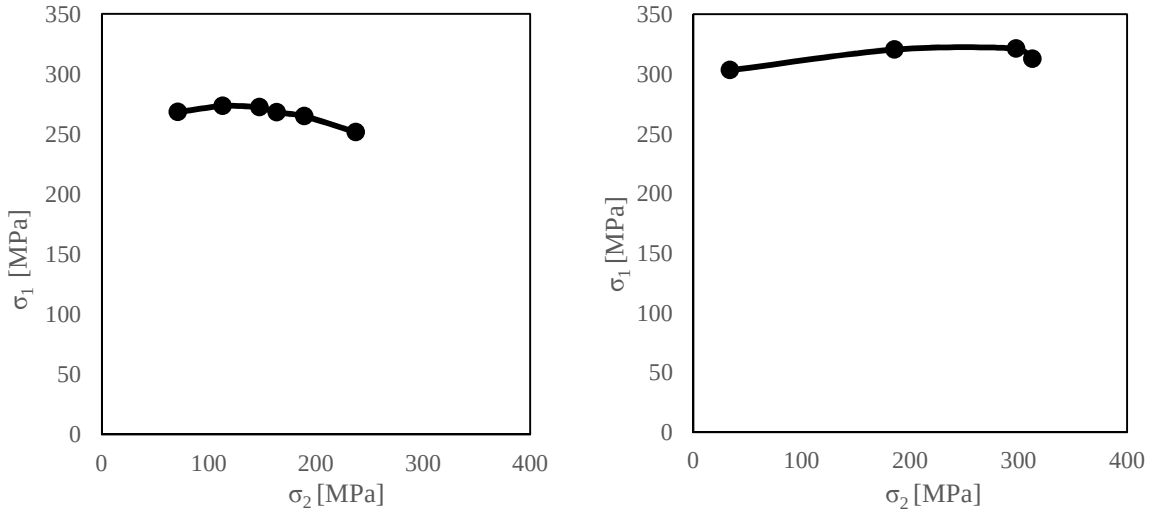

Figure 2.25. Stress-based FLC for: (a) AA5352 aluminum alloy; (b) TH330 steel.

2.4.2. Strain rate analysis – linear best fit

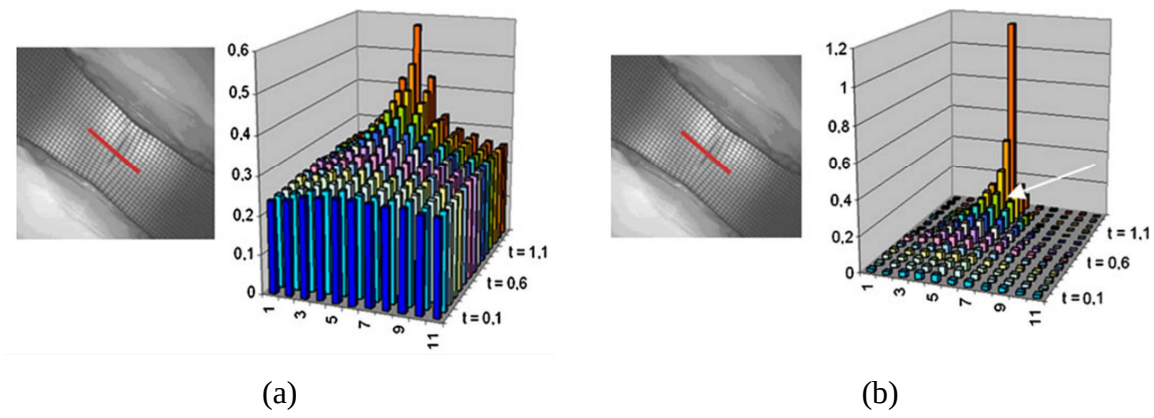

Figure 2.26. Evolution of the necking: (a) Thinning; (b) Thinning rate (extracted from Volk & Hora, 2010).

As previously mentioned, Volk & Hora, 2010 proposed a method for the experimental identification of the onset of failure, which consists in a temporal analysis of the thickness strain, ε_3, and of the thickness strain rate, $\dot{\varepsilon}_3$, along a section perpendicular to the failure region. Figure 2.26 (a) shows a continuously growth of thinning, which can cause problems for an automatic detection of the beginning of the plastic instability. Therefore, it is helpful to have a look at the distribution of the thinning rate, as shown in Figure 2.26 (b). The necking is much more distinct if the thinning rate is in focus. This is

due to the fact that the thinning rate outside of the instability area has to decrease, which intensifies even more the effect of an increase inside this area. In the given example, it is possible to identify the instability beginning (marked with white arrow).

However, as the formulation used in DD3IMP is quasi-static, each time increment corresponds to an increment of displacement. Thus, a temporal analysis becomes a position analysis (displacement-dependent method), in order to detect the onset of necking. The beginning of necking is associated with a thickness reduction. Therefore, it is important to follow the evolution of the strain in the thickness direction. The thickness in each displacement increment, t^u, is given by:

$$t^u = t_0 \exp\left(\varepsilon_3^u\right), \tag{2.28}$$

where t_0 represents the initial thickness of the sheet metal and ε_3^u is the through-thickness strain, in each displacement increment. Therefore, the thinning rate is defined as:

$$\dot{t} = \frac{t^{u+\Delta t} - t^u}{\Delta t}. \tag{2.29}$$

As shown in the beginning of the thinning rate evolution, it is possible to see a stable zone characterized by a nearly homogeneous deformation (low slope). Afterwards, the localized necking is characterized as instable deformation, of different slope, until the crack occurs. Therefore, the method used in this work consists in fitting the stable and instable areas with two linear curves by using a linear regression with Excel ®. The intersection of these two straight lines will be used to define the beginning of the instability, i.e., necking. The algorithm is clear, easy to implement and usable for a wide range of materials. Furthermore, it is based on a physical motivation (identification of instability).

2.4.3. GTN Model

For ductile materials, failure is caused by material internal degradation. There are several ductile damage theories, describing the material internal degradation. The coupled damage models have the ability to predict an accurate fracture location under a specific range of stress triaxiality, especially the formulations proposed by Gurson, 1977 and Lemaitre, 1985. As an example, the GTN original model is able to predict fracture in

ductile materials. One of the suitable theoretical approaches for determining the FLC is the GTN model, which is based on Gurson's theory. Particularly, it has a good performance when the spherical void growth is the predominant mechanism (high levels of triaxiality). However, this model has limitations when the elongation of voids is the predominant mechanism (low stress triaxiality) (Malcher, 2012). The Gurson model and the original GTN model will be presented in the following sections.

2.4.3.1. Gurson's model

The model proposed by Gurson, 1977 is one of the first micromechanical based models for the description of ductile damage and fracture. This theory introduces a strong coupling between plastic strain and damage, in the presence of finite strains. The internal degradation mechanism is related to the appearance of micro-voids associated with a large plastic deformation. The degradation of the material is measured by the void volume fraction (f), which represents the ratio between the volume of the void (V_{void}) and the volume of the representative element (V_{RVE}):

$$f = \frac{V_{void}}{V_{RVE}}. \tag{2.30}$$

Figure 2.27 shows the relation between the degradation of the materials' micro structure and the macroscopic load evolution, for a tensile loading. The presence of micro voids or the formation of new ones causes the degradation of the material, with 4 stages:

a) No appreciable change in the micro structure;

b) Nucleation of micro voids (existence of localized plastic strain);

c) Growth of micro voids (high tensile hydrostatic stresses);

d) Coalescence of voids.

The yield function proposed by Gurson can be expressed by:

$$\phi(\boldsymbol{\sigma}, \bar{\varepsilon}^{\mathrm{p}}, f) = J_2(\boldsymbol{\sigma}') - \frac{1}{3}\left\{1 + f^2 - 2f\cosh\left(\frac{3p}{2Y}\right)\right\}Y^2 \tag{2.31}$$

where J_2 represents the second invariant of the deviatoric stress tensor ($\boldsymbol{\sigma}'$), p is the hydrostatic pressure, Y is the considered isotropic hardening rule and $\bar{\varepsilon}^{\mathrm{p}}$ represents the isotropic hardening internal variable.

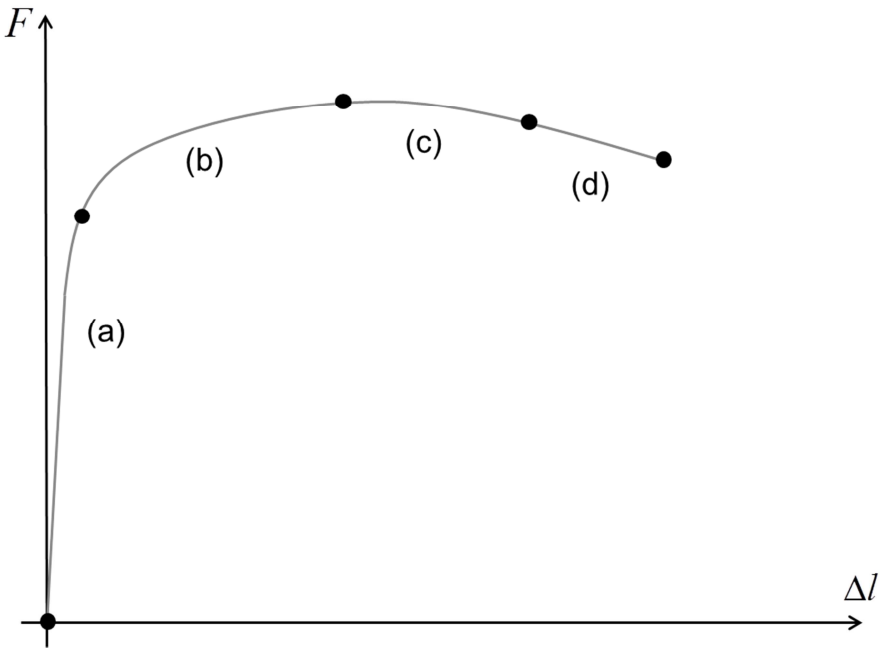

Figure 2.27. Force-displacement diagram indicating the 4 stages of voids evolution.

2.4.3.2. Gurson-Tvergaard-Needleman (GTN)'s model

The biggest disadvantage of the Gurson model is the fact that no void volume fraction will be predicted if the initial void ratio is zero, regardless of the strain history of the material. Thus, in order to improve the performance of the model, several damage mechanisms have been proposed such that voids can nucleate depending on the strain history. Needleman & Tvergaard, 1984 proposed the GTN model, considering that damage evolution is represented by three successive mechanisms: (i) nucleation, (ii) growth and (iii) coalescence of voids.

The effective porosity, f^*, is determined from both nucleation and growth mechanisms if the void volume fraction is less than the critical value, f_c. When the value of this variable is less than the void volume fraction, the coalescence mechanism becomes active. Hence, the effective porosity is given by:

$$f^* = \begin{cases} f, f < f_c \\ f_c + \left(\frac{1}{q_1} - f_c\right)\frac{(f - f_c)}{(f - f_f)}, f \geq f_c \end{cases} \quad (2.32)$$

where f_c represents the critical void volume fraction and f_f is the void volume fraction at fracture. The void volume fraction rate, $\dot{f}$, is obtained by the sum of the nucleation and growth mechanism:

$$\dot{f} = \dot{f}^n + \dot{f}^g \tag{2.33}$$

where $\dot{f}^n$ represents the void volume fraction rate of all particles with potential for micro void nucleation, while $\dot{f}^g$ is the void volume fraction rate of all particles during the growth of micro voids. It is worth noting that the nucleation mechanism can be driven by plastic strain or hydrostatic pressure. Therefore, this mechanism is active if the hydrostatic pressure is greater than 0, $p > 0$. Finally, the yield function is given by:

$$\phi(\boldsymbol{\sigma}, \bar{\varepsilon}^{\mathrm{p}}, f) = J_2(\boldsymbol{\sigma}') - \frac{1}{3}\left\{1 + q_3 f^{*2} - 2q_1 f^{*} \cosh\left(\frac{q_2 3p}{2Y}\right)\right\} Y^2 \tag{2.34}$$

where the adjustment parameters q_1, q_2 and q_3 are introduced to bring the model predictions into closer agreement with the numerical analyses of voids and/or to experimental results.

As previously mentioned, this model is implemented in DD3IMP solver, combined with the CPB06 yield criterion. In the context of the current work, a preliminary study, considering micromechanical finite-element analyses of three-dimensional unit cells, was carried out. The TH330 steel was the material selected to perform the study. In the context of the benchmark analysis, the obtained results are not relevant. Thus, a brief summary is present in ANNEX A.

3. RESULTS AND DISCUSSION

In this section, the numerical results for all forming operations are analyzed and discussed. According to the objectives of this work, the results presented comprise the drawing, reverse redrawing and expansion punches load evolutions with the stroke, the cup height after drawing and reverse redrawing operations and the thickness profile after the reverse redrawing operation. Moreover, the evolutions of the pressure-pad load and position, with respect to the punch stroke, are also presented, for improved results analysis. The numerical simulations were performed considering the CB2001 and the CPB06 yield criteria for each material, since one of the objectives of this work was to improve knowledge concerning the description of the SD effect in sheet metal forming.

For the failure prediction, three approaches are shown: (i) FLC strain-based, with the presentation of the strain paths for some points, (ii) FLC stress-based and (iii) a strategy based on the strain rate. In this last section, the difficulties related with the failure prediction are also highlighted. Moreover, it should be mentioned that the experimental results are not yet available, which limits the analysis concerning which yield criteria renders an improved description of the numerical results.

3.1. Drawing operation

For this first stage, it is important to understand the evolution of the punch load with the stroke and the cup height after the drawing operation. The punch load evolution for the AA5352 aluminum alloy and the TH330 steel is shown, for both yield criteria, in Figure 3.1. For the AA5352, the evolution presents a similar trend for both yield criteria until 10 mm of punch stroke. Between 10 mm and 30 mm, the punch load evolution presents a decreasing monotonous behavior for the CB2001 while, for the CPB06 the load increases, which is an atypical behavior. Both evolutions show a sudden decrease for approximately 25 mm of punch displacement that, as it will be discussed later, corresponds to the instant when the sheet loses the contact with the pressure-pad. The maximum force is attained with the CPB06 yield criterion. From 30 mm forward, the punch load is constant and zero, since it corresponds to the point when the cup is fully drawn, i.e. there is

no contact with the die radius. Regarding the TH330, the punch load evolution is similar for both yield criteria, with the CPB06 attaining a higher maximum value. Also note that, regarding the point of loss of contact with the pressure-pad, the CB2001 shows this instant for a lower punch stroke. This is an indication that the global cup height is lower for this criterion.

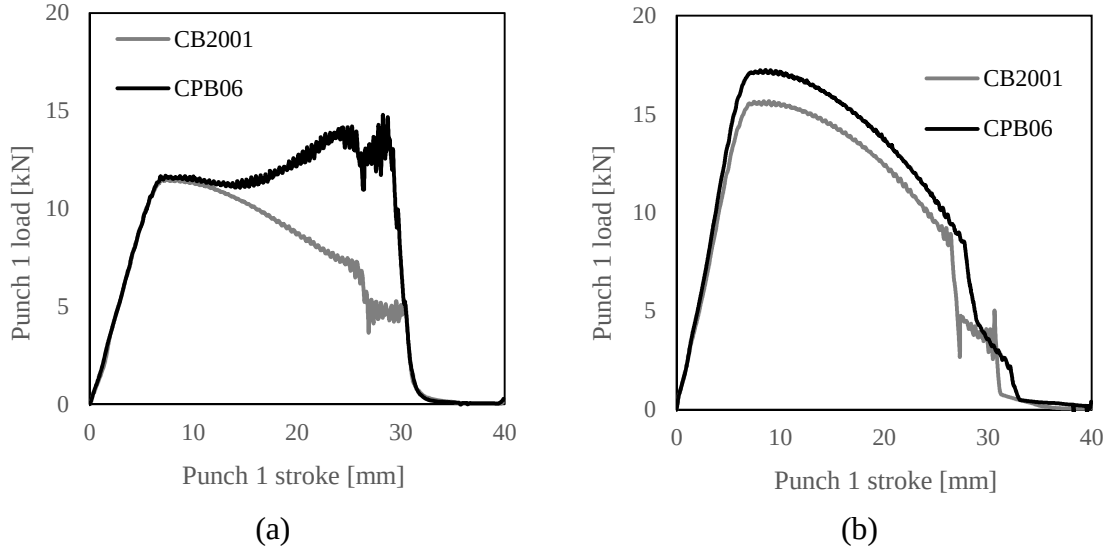

Figure 3.1. Punch 1 load evolution with its stroke during the drawing operation for: (a) AA5352 aluminum alloy and (b) TH330 steel.

The pressure-pad load evolution with the punch stroke is shown in Figure 3.2, in order to clarify some aspects about the punch load evolution. From Figure 3.2, it is possible to confirm that the instant when the blank losses contact with the pressure-pad is almost the same for the AA5352 aluminum, while for the TH330 steel it occurs for a lower punch stroke for the CB2001.

In order to keep the pressure-pad force constant, as shown in Figure 3.2, its vertical displacement evolves during the process, as presented in Figure 3.3. This vertical displacement is negative during most of the process due to the combined effect of the bending moment imposed to the flange, but also to the fact that material located in the flange tends to become thicker, due to the stress state imposed (see Figure 2.23). When the flange becomes smaller than a certain value, the vertical displacement starts to become positive, until attaining the maximum allowed value. As mentioned in section 2.2.4, the maximum positive value of the pressure-pad displacement (about 0.01) was selected, in order to avoid excessive ironing of the flange of the sheet by the pressure-pad. As shown in Figure 3.3 (a), for the AA5352, the numerical simulation performed with the CPB06

presents a more negative displacement, from the beginning of the process. This can be related with the fact reported for the punch load evolution for the AA5352, indicating that for the CPB06 the material located in the flange has more tendency to deform in the thickness than in the radial direction (see the null and negative values of the compression r-values in Figure 2.21 (a)), leading to an increase of the punch force necessary to promote the deformation. This analysis is confirmed by the thickness strain distribution in the final cup, shown in Figure 3.4, where it is visible that the vertical cup wall presents higher thickness in a larger region when the CPB06 yield criterion is used.

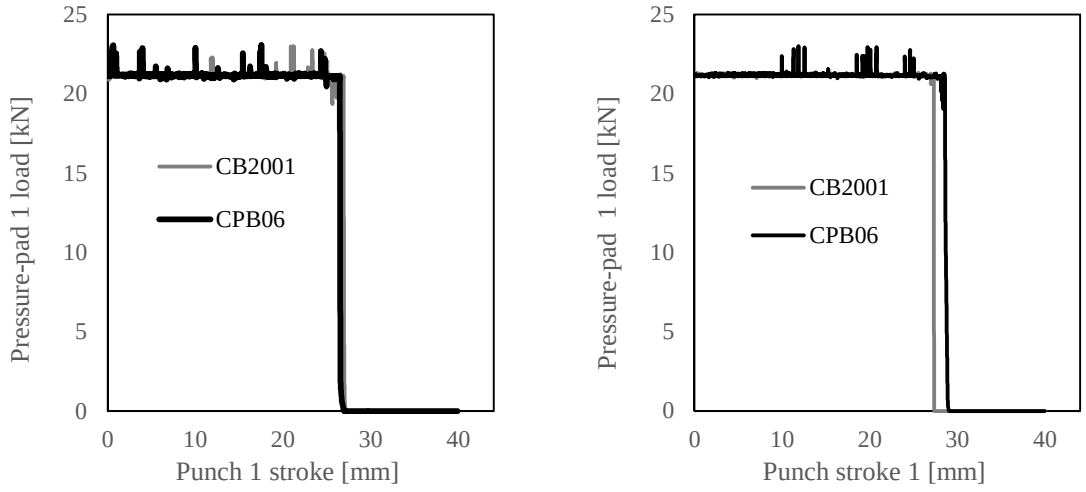

Figure 3.2. Pressure-pad 1 force evolution with the punch 1 stroke during the drawing operation for: (a) AA5352 aluminum alloy and (b) TH330 steel.

Figure 3.3 (b) shows that for the TH330 the more negative displacement is attained with the CB2001 yield criteria, which also presents the globally lower punch force. Thus, this seems to be in contradiction with the previous analysis made for the AA5352. However, it should be noted that this difference between the behavior of the CPB06 yield criterion for both materials may be attributed to the compression r-values prediction (see Figure 2.21 (b)), since for the TH330 steel, they present values always positive, while for the AA5352 they tend to be negative. Moreover, when comparing the compression r-values predicted for TH330 steel, they are about 5 times higher for the CPB06 than for the CB2001, meaning that the deformation in the radial direction *vs* the deformation in thickness direction will be higher for the CPB06. Thus, as shown in Figure 3.5, the numerical simulation performed with the CPB06 yield criterion results in a cup

with a global lower thickness, since the increase of thickness for the material located in the flange is smaller than the one attained with the CB2001 yield criterion. This behavior also seems to slightly restrain the material flow into the die cavity.

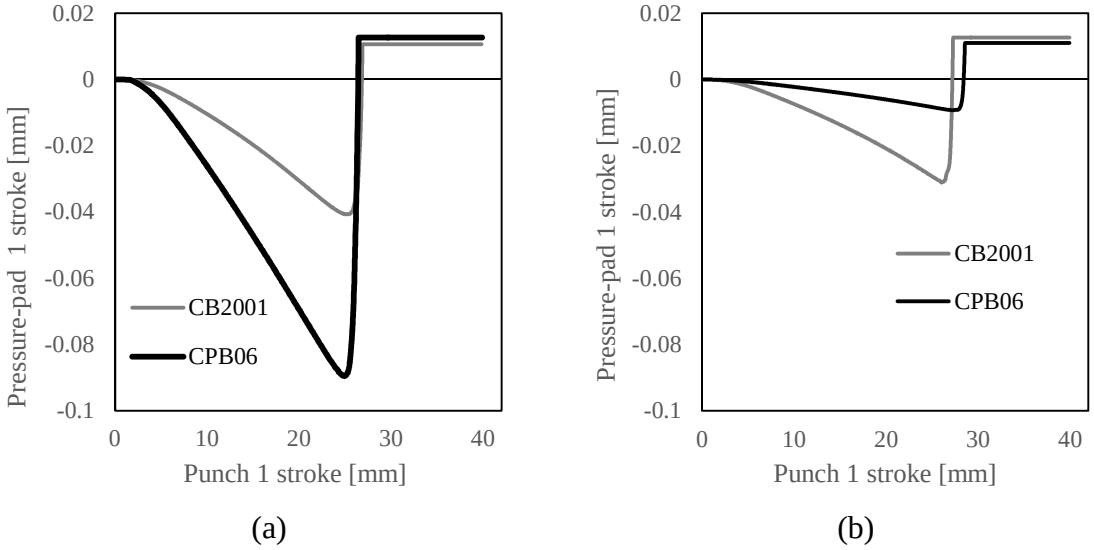

Figure 3.3. Pressure-pad 1 stroke evolution with the punch 1 stroke during the drawing operation for: (a) AA5352 aluminum alloy and (b) TH330 steel.

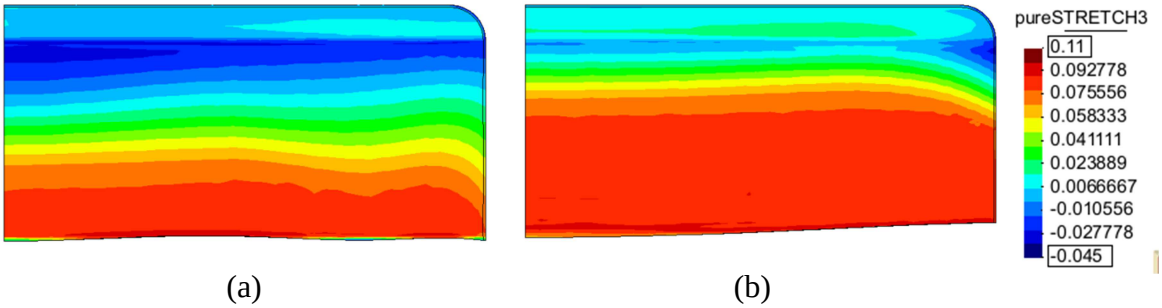

Figure 3.4. Deformation along the thickness direction after the drawing operation for AA5352 aluminum alloy with: (a) CB2001 and (b) CPB06 yield criteria.

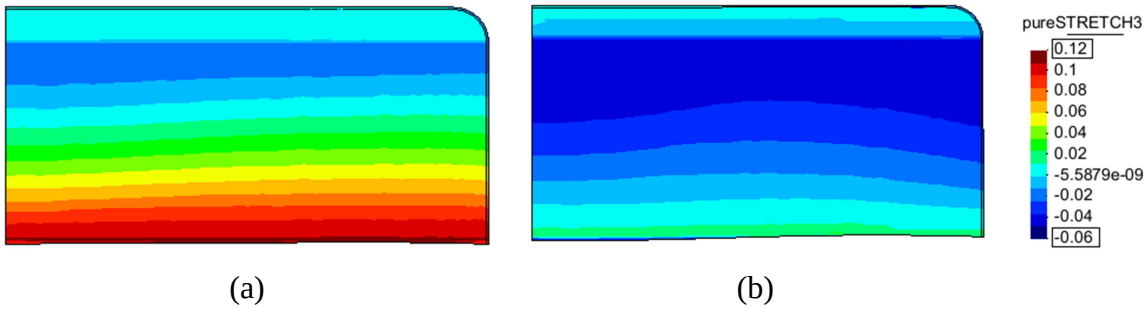

Figure 3.5. Deformation along the thickness direction after the drawing operation for TH330 steel with: (a) CB2001 and (b) CPB06 yield criteria.

Figure 3.6 shows the cup height evolution for the AA5352 and TH330, considering both yield criteria. For the AA5352, considering the full 360º cup, the CB2001 yield criterion predicts a total of eight ears, while CPB06 only predicts two, more pronounced, ears (Figure 3.6 (a)). Figure 2.21 (a) shows that the in-plane distribution for the *r*- values predicted with the CB2001 presents three inflexions, which are also visible in the cup height. Regarding the results obtained with the CPB06 yield criterion, Figure 2.20 (a) shows that of the predicted compression yield stress in RD is lower than in TD. As shown in Figure 2.23, the behavior of the rim in the circumferential direction defined by θ (to the RD) is controlled by the material compression properties, in the direction defined by $\theta + 90$. Thus, the hardening begins earlier in TD than for RD. As a consequence, the plastic strain is higher in TD. Moreover, the thickness in the TD is higher than for the RD, resulting in higher contact forces and, consequently, higher cup height.

For the TH330 steel, the earing profile predicted is similar for both criteria. This seems to be agreement with the fact that this material presents a less pronounced anisotropic behavior considering uniaxial tensile results, with an in-plane distribution of the yield stresses and r-values with only slight variations, which both yield criteria describe similarly well. The major differences are the increased height and the slightly more pronounced ear of the results obtained with the CPB06 yield criterion. As previously mentioned, this seems to be related with the differences reported for the in-plane distribution of the compression yield stresses and r-values.

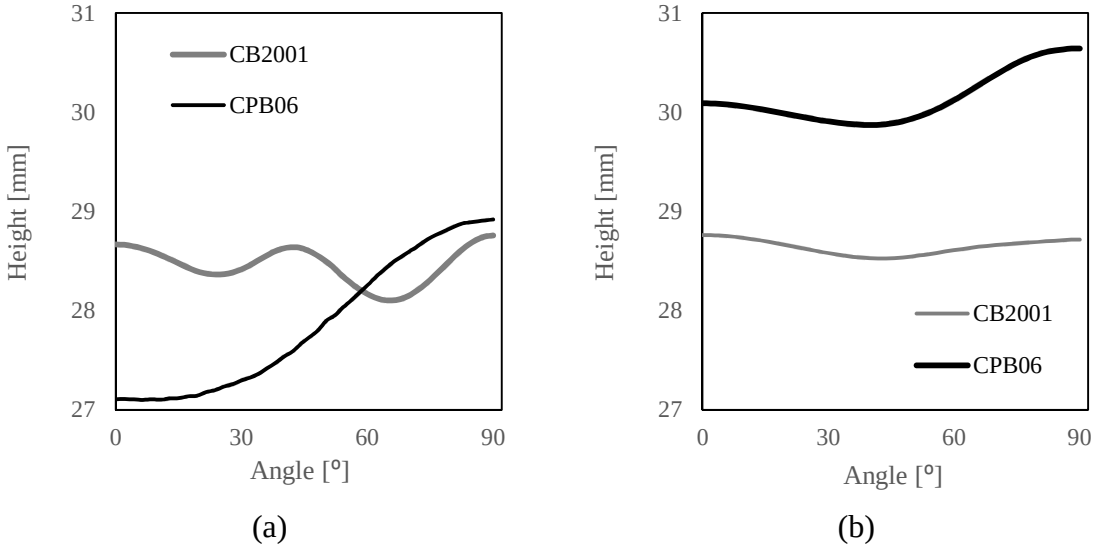

Figure 3.6. Cup height after drawing operation for (a) AA5352 aluminum alloy and (b) TH330 steel.

3.2. Reverse redrawing operation

The reverse redrawing punch load evolution with its stroke is presented in Figure 3.7. Globally, the evolutions obtained present the expected trend, exhibiting a peak for a punch force related with the instant the thickened area goes through the die/blank-holder free space, which give rise to some restraining forces that must be overcome (Thuillier et al., 2010). In fact, after the first stage the thickness distribution is not uniform in the cup wall, presenting values that are higher than the initial thickness in the upper part of the cup (see Figure 3.4 and Figure 3.5).

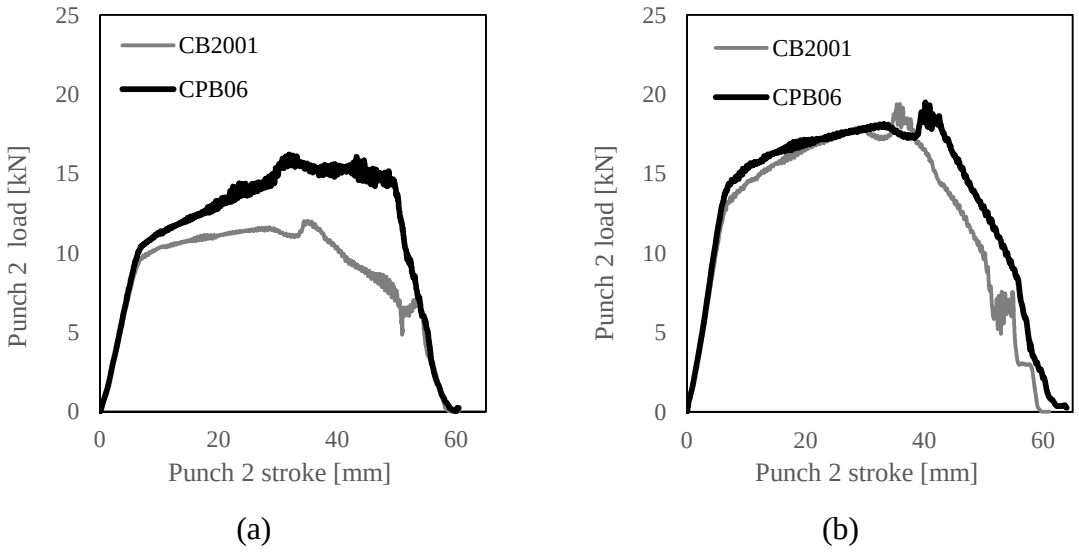

Figure 3.7. Punch 2 force evolution with the punch 2 stroke during the reverse redrawing operation for (a) AA5352 aluminum alloy and (b) TH330 steel.

Regarding the AA5352, until 8 mm of punch stroke, the evolution for both yield criteria is the similar. Between 10 mm and about 35 mm, the punch force evolution presents an increasing monotonous behavior, for both yield criteria, followed by the peak previously mentioned. Thus, the thickness strain distribution presented in Figure 3.4 seems to explain the fact that the force is always higher for the CPB06 yield criterion. Indeed, the cup wall presents a distribution with a wider zone with higher thickness values. This can also explain why for the CPB06 the peak, related with the transition of the thicker material through the die/blank-holder free space occurs for a smaller punch stroke. From 55 mm onward, the behavior is the same again, indicating that loss of contact with the pressure-pad occurs for the same punch stroke.

For the TH330 steel, the punch load evolution is, like for the drawing operation, very similar. Nevertheless, it should be noted that the previously mentioned

peak occurs earlier for the result obtained with the CB2001, which is in agreement with thickness strain distribution presented in Figure 3.5. Also, the instant when the blank loses contact with the pressure-pad is, again, earlier for the results obtained with CB2001 yield criterion, indicating a globally smaller cup.

As for the drawing operation, Figure 3.8 presents the pressure-pad force evolution with the punch stroke, to highlight the instants corresponding to the loss of contact between the cup and this tool. As for the drawing stage, for the AA5352, the loss of contact occurs for a similar instant. For the TH330 steel, as for the drawing stage, the results obtained with the CB2001 yield criterion indicate an earlier loss of contact. In comparison to the drawing phase, the difference between the prediction for TH330 with both yield criteria increases.

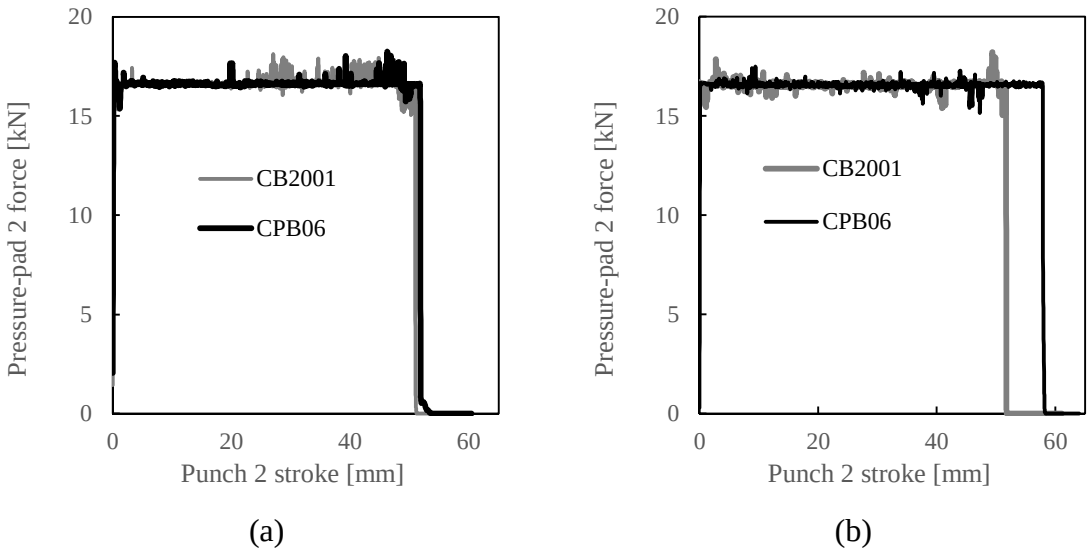

Figure 3.8. Pressure-pad 2 force evolution with the punch 2 stroke during the reverse redrawing operation for (a) AA5352 aluminum alloy and (b) TH330 steel.

Figure 3.9 presents the evolution of the pressure-pad vertical displacement with the punch stroke. In order to press the cup, all curves present an initial negative displacement. Notice that in this case, due to the reversed direction of the punch, the bending moment and the increase of thickness tends to move the pressure-pad to positive values. Thus, the limit value for the pressure-pad displacement, to avoid excessive ironing of the flange, is negative (-0.05 for the AA5352 and the TH330 with the CB2001 and -0.1 with the CPB06). Figure 3.9 (a) shows that for AA5352, the pressure-pad displacement is globally more positive for the simulation performed with CPB06, which is in agreement with the thickness distribution in the cup at the end of the drawing stage. Moreover, it also

indicates that during this stage there is also an increase of thickness of the cup, which should be higher for the simulation performed with the CPB06 yield criterion. Figure 3.10 shows the thickness strain distribution, for the AA5352, for a punch displacement of 50 mm (close to the instant the cup loses contact with the pressure-pad), confirming that globally higher thickness are attained with the CPB06 yield criterion. Thus, a higher positive value of the displacement of the pressure-pad is required, in order to keep its force constant, to avoid vertical movements. For the TH330 steel, Figure 3.9 (b) shows an almost constant pressure-pad displacement for the CPB06, which can be explained by the small variation of thickness induced by the drawing stage (see Figure 3.4). For the results obtained with CB2001, since the cup drawn in the first stage presents higher thickness values (see Figure 3.4), this results in a higher positive vertical movement of the pressure-pad. Moreover, Figure 3.11 presents shows the thickness strain distribution, for the TH330, for a punch displacement of 50 mm, confirming that the numerical simulation performed with the CPB06 presents almost no thickness change. Thus, since there is no thickness increase for the material located between the pressure-pad and the die, the pressure-pad force restrains more the movement of the cup. Furthermore, Figure 3.9 (b) confirms the quicker flow of the cup for the TH330 steel modelled with CB2001.

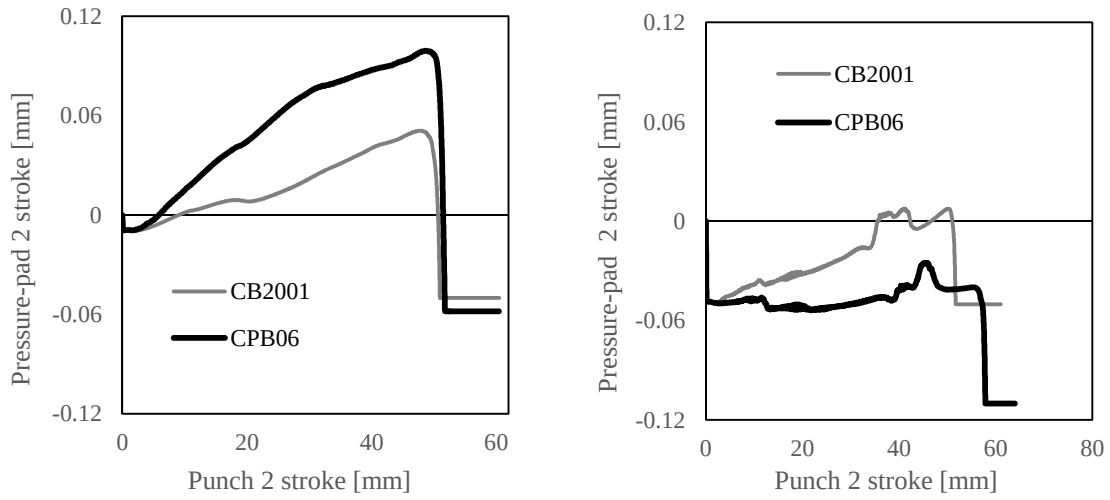

Figure 3.9. Pressure-pad 2 stroke evolution with the punch 2 stroke during the reverse redrawing operation for (a) AA5352 aluminum alloy and (b) TH330 steel.

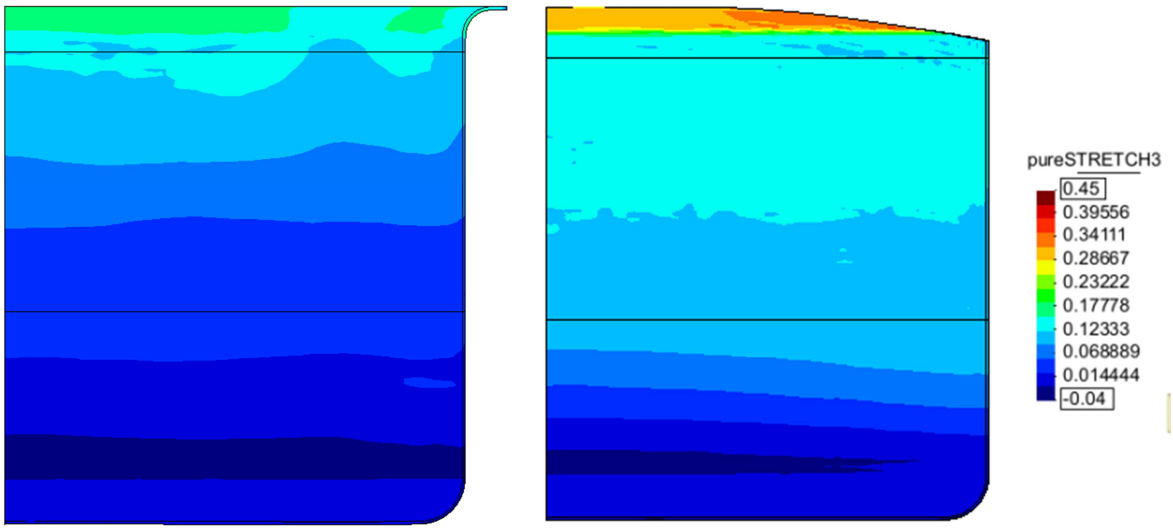

(a) (b)

Figure 3.10. Deformation along the thickness direction for the AA5352 aluminum alloy and a 50 mm punch stroke, as predicted by the yield criterion: (a) CB2001 and (b) CPB06. The black lines correspond to the ones that will be located at 20 mm and 45 mm from the cup bottom, at the end of the redrawing stage.

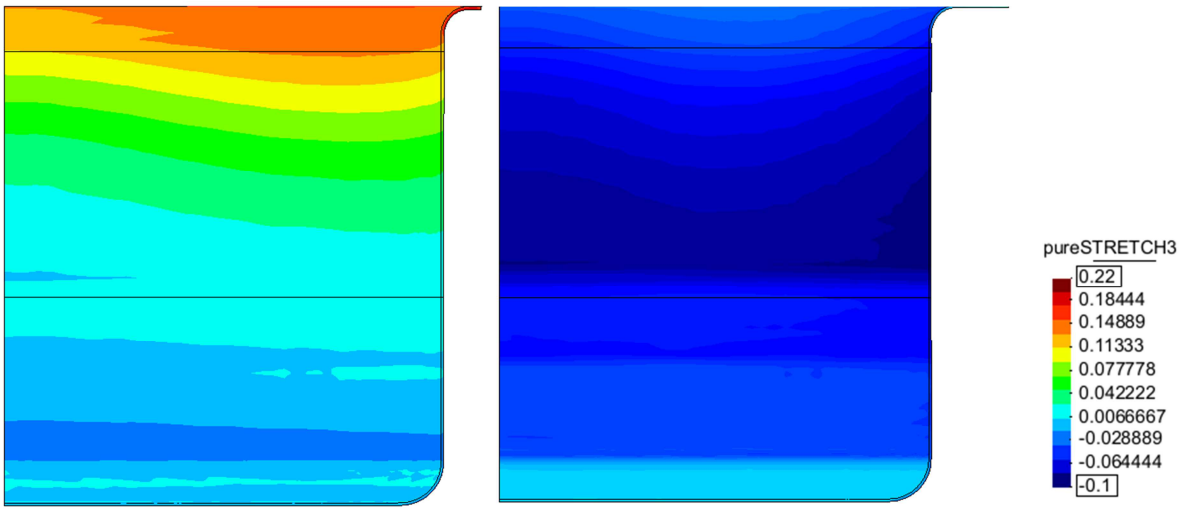

(a) (b)

Figure 3.11. Deformation along the thickness direction for the TH330 steel and a 50 mm punch stroke, as predicted by the yield criterion: (a) CB2001 and (b) CPB06. The black lines correspond to the ones that will be located at 20 mm and 45 mm from the cup bottom, at the end of the redrawing stage.

Figure 3.12 presents the cup height after the reverse redrawing operation. Globally, for both materials, the earing profile remains the same with only a slight attenuation of the earing phenomenon.

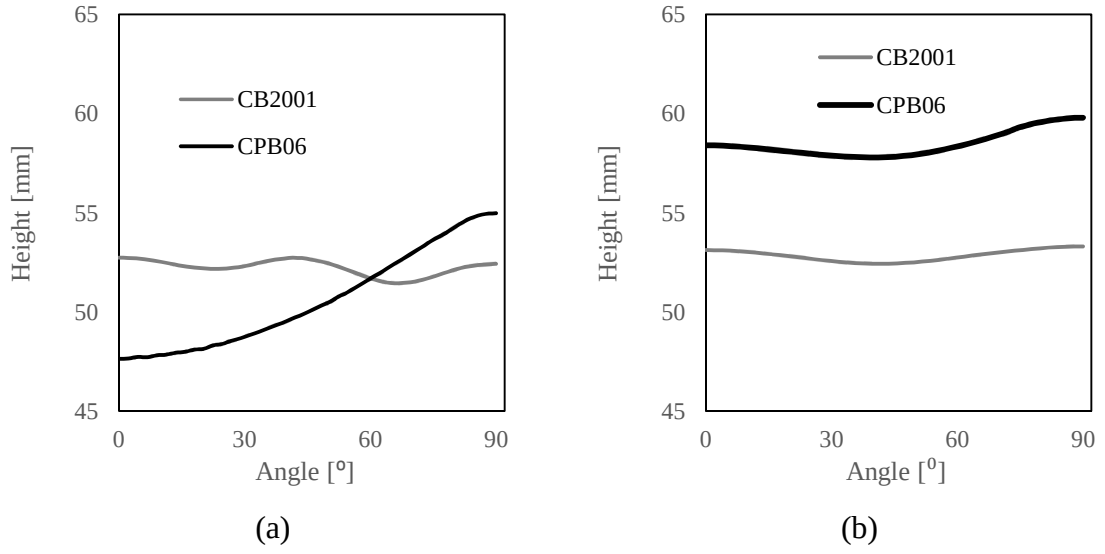

Figure 3.12. Cup height after the reverse redrawing operation for (a) AA5352 aluminum alloy and (b) TH330 steel.

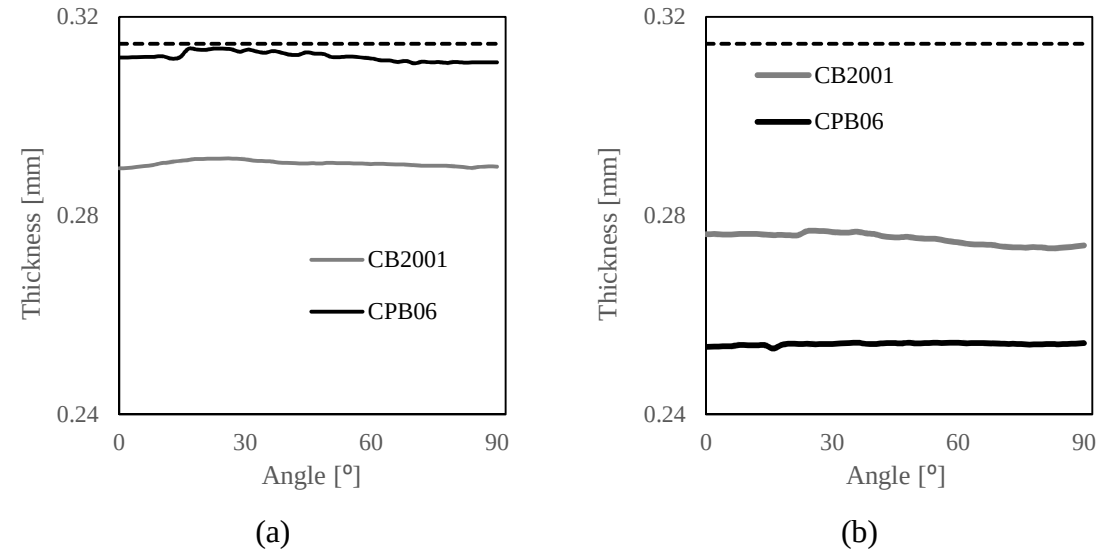

Figure 3.13. Thickness profile at a height of 20 mm from the base of the cup after the reverse redrawing operation for: (a) AA5352 aluminum alloy and (b) TH330 steel. The dashed line corresponds to the gap between the punch and the die of the redrawing operation.

Figure 3.13 presents the thickness profile at a height of 20 mm from the base of the cup after the reverse redrawing operation, for both materials, with the CB2001 and CPB06 yield criteria. Regarding the AA5352, the thickness predicted with the CB2001 yield criterion is lower when compared with the CPB06, with an evolution along the RD quite similar. For the TH330 the reverse relation is observed, with the CB2001 predicting a higher thickness. In fact, it should be mentioned that for the AA5352, both yield criteria

predict thickness values higher than the initial one (0.279), while for the TH330 only the CB2001 predicts a value slightly higher than the initial one (0.270).

Figure 3.14 presents the same results, at a height of 45 mm from the base of the cup. Regarding the AA5352, the results show a similar thickness evolution predicted by both yield criteria. These results are in agreement with the distribution shown in Figure 3.10, where it is shown that the thickness is higher with CPB06 than with CB2001, at 20 mm of cup height (bottom low black line), being always higher than the initial thickness (0.279 mm). However, at 45 mm of cup height, the thickness is almost similar. Indeed, the gap between the punch and the die of the redrawing operation is 0.31455 (dashed line in Figure 3.13 and Figure 3.14). Thus, these results indicate that, for both yield criteria, there is ironing of the vertical wall. Figure 3.15 shows the contact forces, for the instant corresponding to a punch stroke of 50 mm, highlighting the ironing effect. This figure also shows that, although the loss of contact between the pressure-pad and blank occurs for a similar instant, the flange is much smaller for the CPB06, promoting the more pronounced ear.

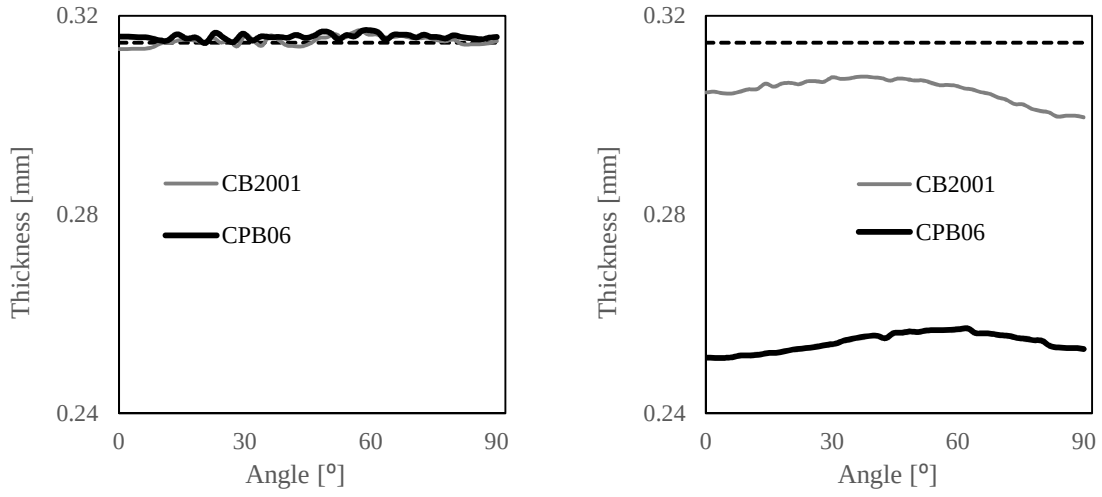

Figure 3.14. Thickness profile at a height of 45 mm from the base of the cup after the reverse redrawing operation for: (a) AA5352 aluminum alloy and (b) TH330 steel. The dashed line corresponds to the gap between the punch and the die of the redrawing operation.

For the TH330, **Figure 3.13** (b) and **Figure 3.14** (b) show a thickness reduction (compare with the initial thickness of (0.270 mm)) with CPB06 yield criterion, for both heights. As previously mentioned, this seems to be related with the very higher compression r-values predicted with CPB06 (see Figure 2.21). On the other hand, the

CB2001 predicts an increase of thickness. Note that the thickness values are always smaller than the gap between the redrawing punch and die (black dashed line). Thus, there is no ironing effect of the vertical wall in this case.

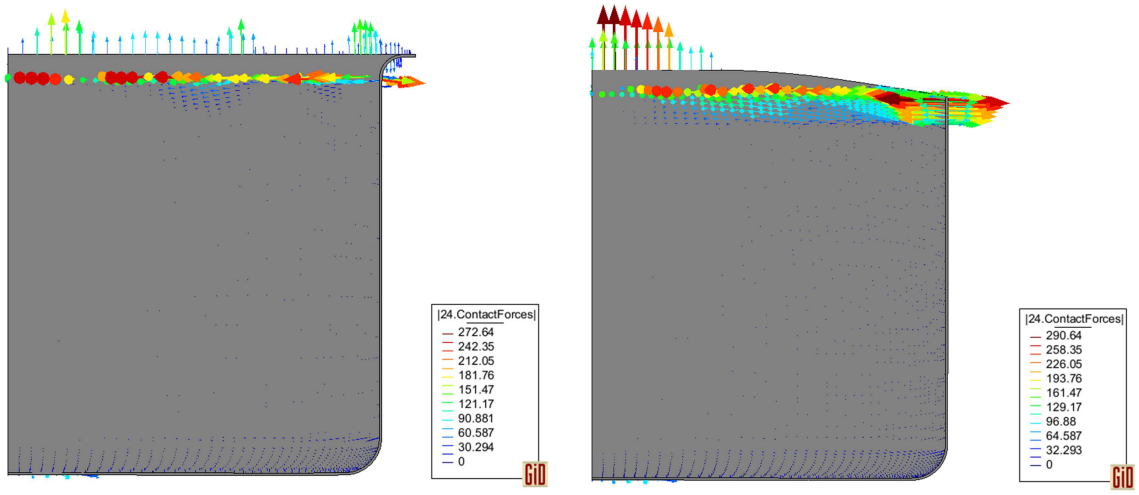

(a) (b)

Figure 3.15. Contact forces when punch 2 stroke is 50 mm for AA5352 aluminum alloy with yield criterion: (a) CB2001 and (b) CPB06.

3.3. Expansion operation

The expansion punch load evolution with its stroke is presented in Figure 3.16, for both materials and both yield criteria. In contrast with the previous stages, the results obtained with the CB2001 always present the higher values of force. For the AA5352, both yield criteria present a similar evolution. The results obtained with the CPB06 start with a smaller force because the contact will be stablished in a smaller region, as a result of the earing profile. For the TH330 steel, both yield criteria present a similar evolution until a punch stroke of approximately 10 mm. The fact that afterwards the CB2001 predicting a higher punch load can be related with the higher thickness predicted for the cup wall, at the end of the redrawing operation.

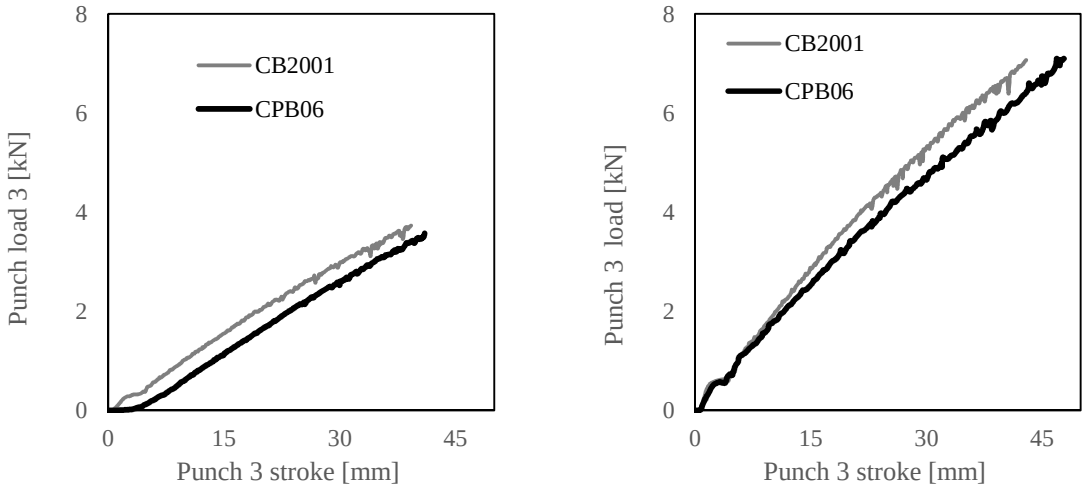

Figure 3.16. Punch 3 force evolution with the punch 3 stroke during the expansion operation for (a) AA5352 aluminum alloy and (b) TH330 steel.

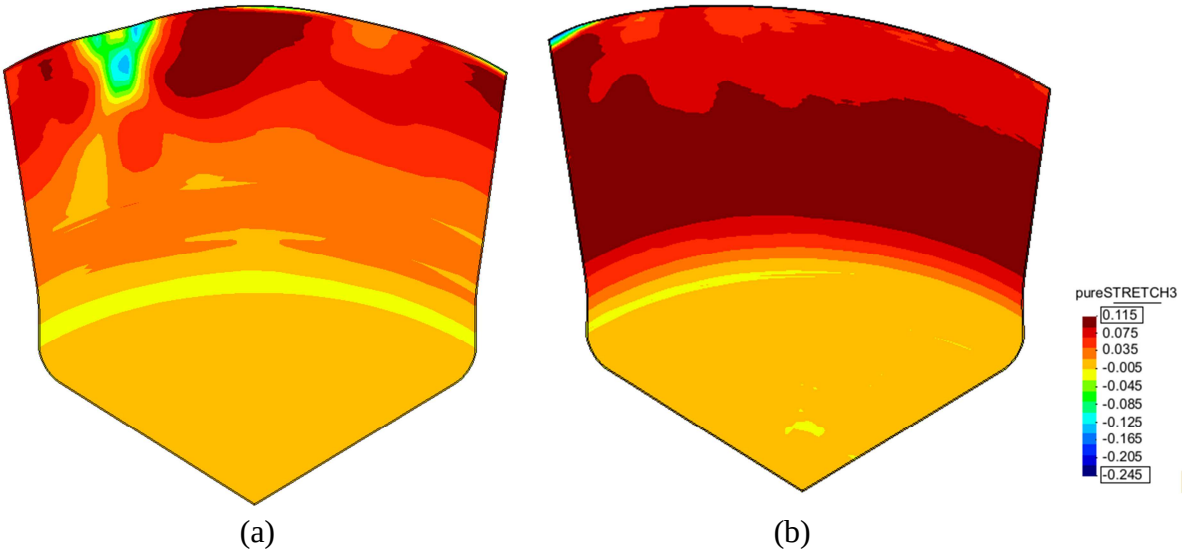

Figure 3.17. Deformation along the thickness direction after the expansion operation for AA5352 aluminum alloy with yield criterion (a) CB2001 and (b) CPB06.

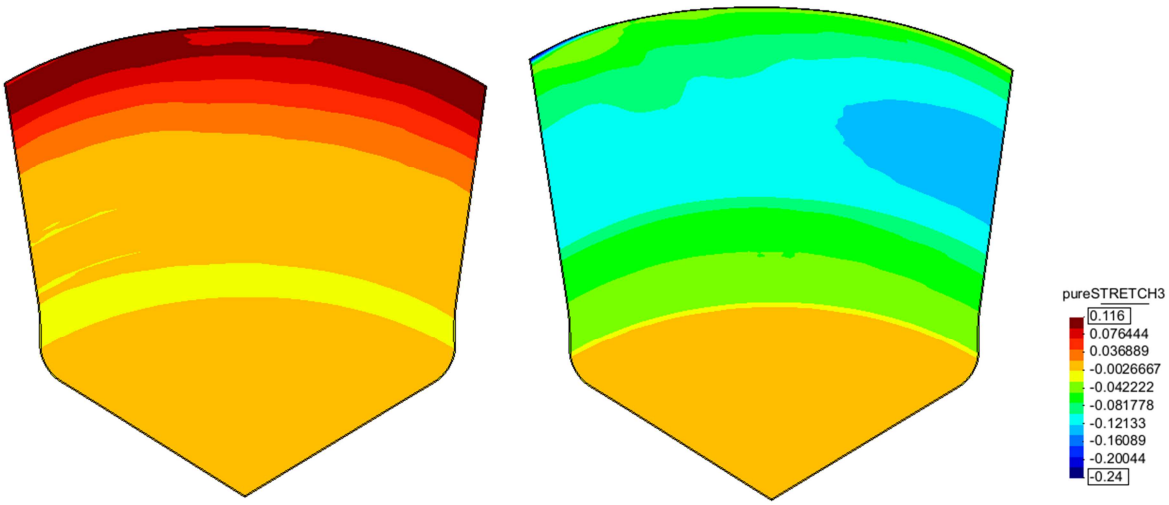

(a) (b)

Figure 3.18. Deformation along the thickness direction after the expansion operation for TH330 steel with yield criterion (a) CB2001 and (b) CPB06.

As shown in Figure 3.16, the expansion phase was simulated until a maximum punch displacement, without taking into account the onset of failure. Therefore, it is possible to analyze the deformation along the thickness direction, at the end of the expansion phase, for all materials and yield criteria. Figure 3.17 and Figure 3.18 shows these results for the AA5352 and the TH330 materials, respectively. The only simulation showing strain localization (necking) is the one performed with the CB2001 yield criterion, for the AA5352 aluminum alloy. Hereinafter, the only simulation taken into account to predict the onset of the failure and the failure point is this one.

3.4. Strain-based FLC and strain paths

The first strategy adopted to try to predict the instant and the location of the onset of failure is to follow the numerically predicted strain paths, in order to compare them with the experimental FLC (see Figure 2.24).

The numerical implementation of the failure criterion based on the experimental FLC strain-based considers the eigenvalues of the stretch tensor $\mathbf{U}$ evaluated for each node, corresponding to the major and minor strain, ε_1^{num} and ε_2^{num}. In order to evaluate if the node is prone to necking, it is necessary to compare its major strain with the admissible one, evaluated based on the FLC. This is done performing a linear interpolation of the experimental data, as schematically shown in Figure 3.19.

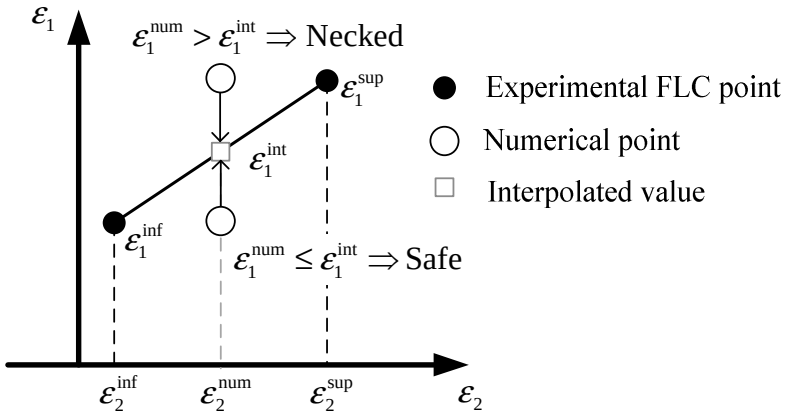

Figure 3.19. Schematic representation of the interpolation method adopted to compare the numerical results with the FLC strain-based.

Thus, the interpolated value is determined using the following expression:

$$\varepsilon_1^{int} = \varepsilon_1^{inf} - \frac{\left(\varepsilon_1^{sup} - \varepsilon_1^{inf}\right)}{\left(\varepsilon_2^{sup} - \varepsilon_2^{inf}\right)}\left(\varepsilon_2^{num} - \varepsilon_2^{inf}\right). \tag{3.1}$$

It should be mentioned that the procedure adopted does not perform any extrapolation of the experimental data, i.e. the interpolated value is only evaluated if the ε_2^{num} is contained within an interval of known experimental data. Table 3.1 presents the outline of the algorithm adopted to perform the formability analysis based on the experimental FLC, represented in section 2.4.1.1. It should be noticed that this algorithm is applied at the end of each user pre-selected increment, i.e. it is not mandatory to make the analysis for all increments.

With this algorithm implemented in DD3IMP, the simulation did not detect any failure problems, i.e. never stopped. As previously mentioned, this was already expected, since the drawing and reverse redrawing operations impose complex strain path changes.

Following the Benchmark requests, the strain history (major and minor principal strains) of three points located in the upper surface of the blank, as a function of each punch stroke (drawing, reverse redrawing and expansion) was recorded. The points are located in the outer flange of the blank at the RD, 45º with the RD (labelled DD) and 90º with RD (labelled TD). In this section, this information is used to present the strain paths for each point, as shown in Figure 3.20 and Figure 3.21, for the AA5352 aluminum alloy and the TH330 steel, respectively. It was decided to show the results for the last one

in order to enable the comparison of strain paths for both materials. The results presented in this section were all obtained with the CB2001 yield criterion. As highlighted in both figures, the strain paths never cross the strain-based FLC, represented by a thick black line.

Table 3.1. Outline of the algorithm adopted in the numerical implementation of the rupture criterion based on the experimental FLC.

READ file containing the FLC experimental information
DO i=1, total number of node of the deformable body
    Determine the major and minor strain ε_1^{num} and ε_2^{num}
    IF $\varepsilon_2^{num} \in \left[\varepsilon_2^{inf}, \varepsilon_2^{sup}\right]$ THEN
        Determine ε_1^{int} using Equation (3.1)
        IF $\varepsilon_1^{num} > \varepsilon_1^{int}$ THEN FIN=True to STOP the computation
    END IF
END DO
IF FIN THEN
    Output the major and minor strain ε_1^{num} and ε_2^{num}
    STOP the computation
END IF

Typically, the strain paths are similar for all three points. In the drawing operation, the strain path is approximately characterized by being situated between pure shear and uniaxial compression (middle and low streak line). Close to the end of the first stage, the points tend to plane strain. In the reverse redrawing operation, the strain path is characterized, once again, by a state between the uniaxial compression and the pure shear. Once again, close to the end of this phase, the point tends to a plane strain path. Finally, the expansion operation corresponds to a strain path close to uniaxial compression. Globally, it is possible to observe that the points follow a more dissimilar trend for the AA5352, highlighting the fact that this material presents a more anisotropic behaviour than the TH330 steel. Also, for the AA5352 higher strains are attained, particularly at the end of the redrawing operation. This seems to be associated with the plane strain path, induced by the ironing stage.

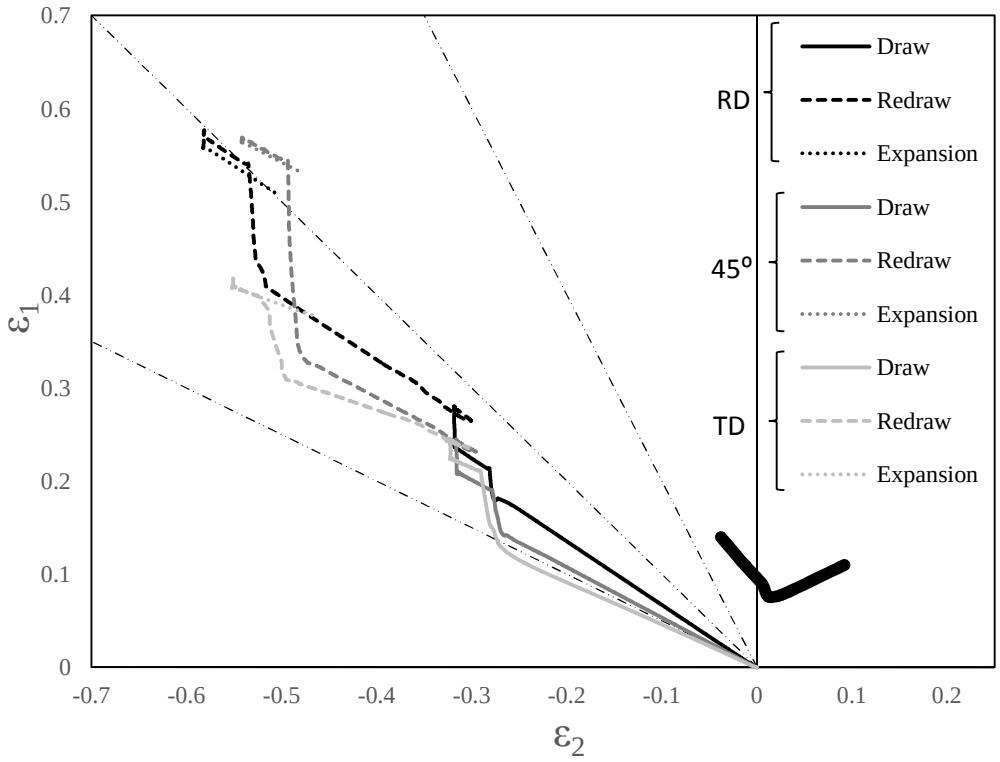

Figure 3.20. FLC strain-based for the AA5352 aluminum alloy and the strain paths at the leading edge of the cup at 0º, 45º and 90º, respected to each stage.

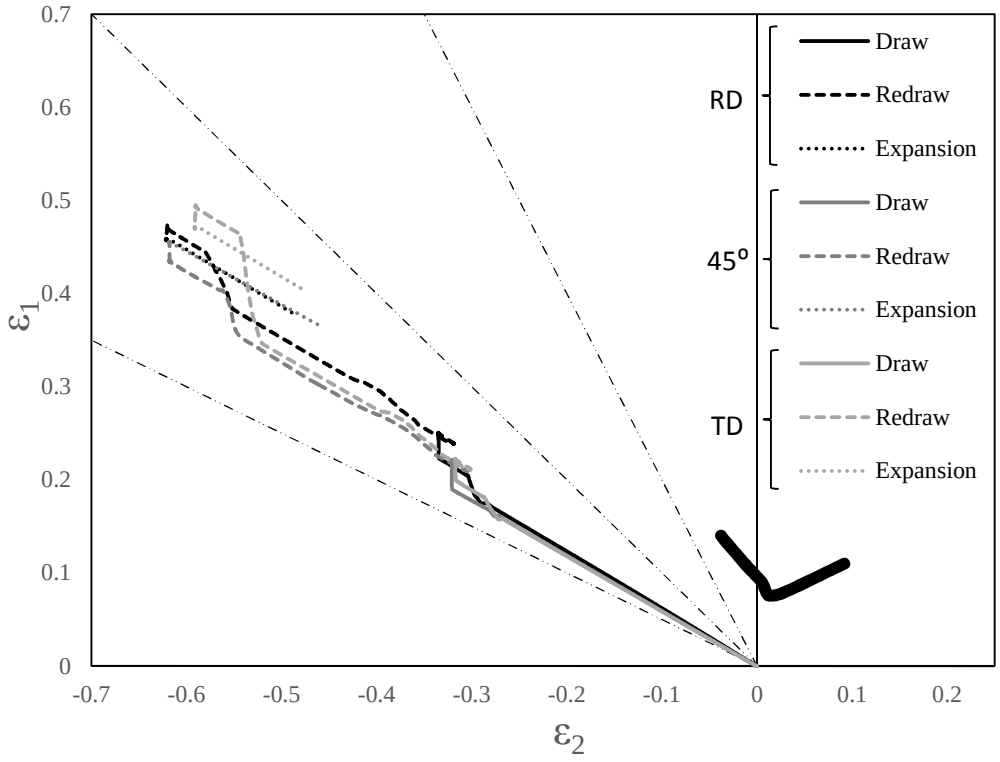

Figure 3.21. FLC strain-based for TH330 steel and the strain paths at the leading edge of the cup at 0º, 45º and 90º, respected to each stage.

3.5. Stress-based FLC

The second strategy adopted to try to predict the instant and the location of the onset of failure is to follow the numerically predicted stress states, in order to compare them with the stress-based FLC (see section 2.4.1.2).

The numerical implementation of the failure criterion based on the experimental stress-based FLC is described in this section. The eigenvalues of the $\hat{\boldsymbol{\sigma}}$ are evaluated for each gauss point (GP), in order to determine the major and minor stress, σ_1^{num} and σ_2^{num}. $\hat{\boldsymbol{\sigma}}$ is the Cauchy stress tensor ($\boldsymbol{\sigma}$) defined in the orthotropic frame which, by definition, has the same eigenvalues as $\boldsymbol{\sigma}$. However, it is important to take into account that the stress-based FLC is determined considering plane stress conditions, assuming that the major and minor stresses occur in the sheet's plane. Moreover, it is also assumed that $\sigma_1 > \sigma_2$ and that $\sigma_3 = 0$. The use of the $\hat{\boldsymbol{\sigma}}$ stress tensor allows a better control (although not free of errors) about the selection of the principal stresses in the sheet's plane, as schematically shown in Figure 3.22.

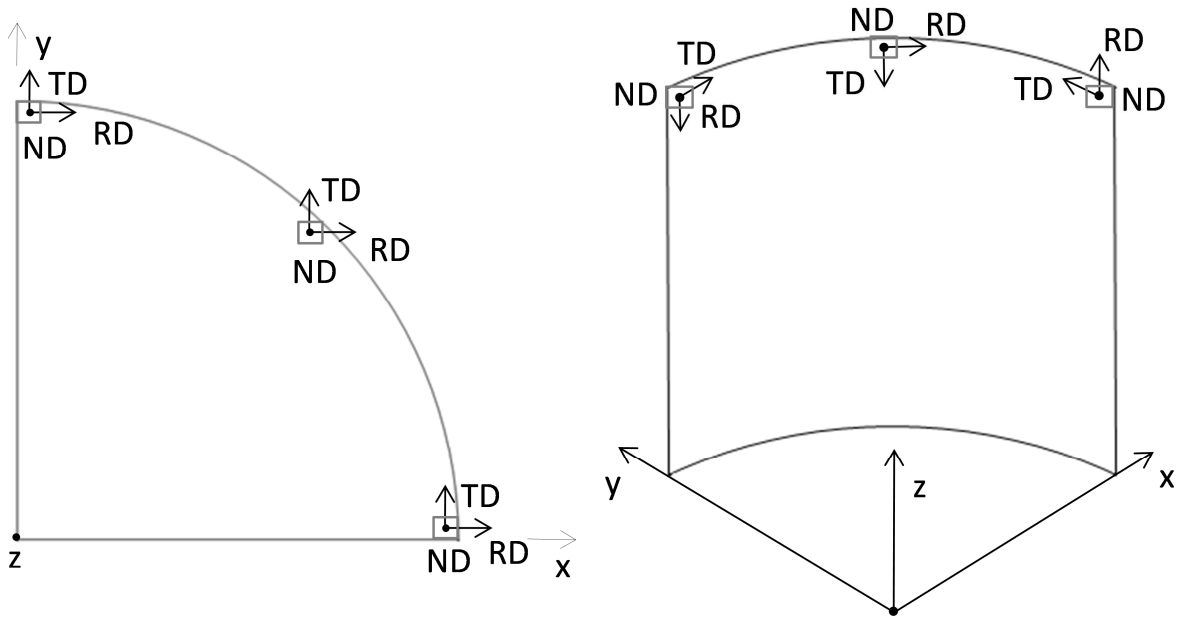

(a) (b)

Figure 3.22. Schematic representation of the orthotropic frame in the: (a) blank and (b) in the vertical wall.

Moreover, based on experimental observations, Tharrett & Stoughton, 2003 showed that it is not possible to form any neck under pure bending, since the stress on the concave side is in compression. As a consequence, it is always below the limit for

initiation of a through-thickness necking instability. On the other hand, necking can be formed at high tension under bending when the stresses on all surfaces exceed the stability limit. Consequently, a reliable necking criterion requires confirmation that all layers through the sheet thickness exceed the instability limit that applies to in-plane tension, before any insipient through-thickness neck can develop or predicted to occur, as schematically shown in Figure 3.23. This figure also shows the strategy introduced by Stoughton & Yoon, 2011, which suggest the subtraction of the current value of σ_3 from all three principal stresses, to obtain an equivalent plane-stress state, ($\sigma_1-\sigma_3, \sigma_2-\sigma_3$, 0), retaining the shape of the conventional stress-based FLC for plane-stress conditions. This strategy is based on the fact that, if the tri-axial stress condition (σ_1, σ_2, $\sigma_3 = 0$) is a point of necking instability on the conventional stress-based FLC, then, as a result of the invariance with respect to hydrostatic stress, all stress states ($\sigma_1+c, \sigma_2+c, \sigma_3=c$) will also be unstable against necking. So as a result, the magnitude of σ_3 defines if all points in the entire (σ_1, σ_2) space used in the conventional stress-based FLC are safe or necked.

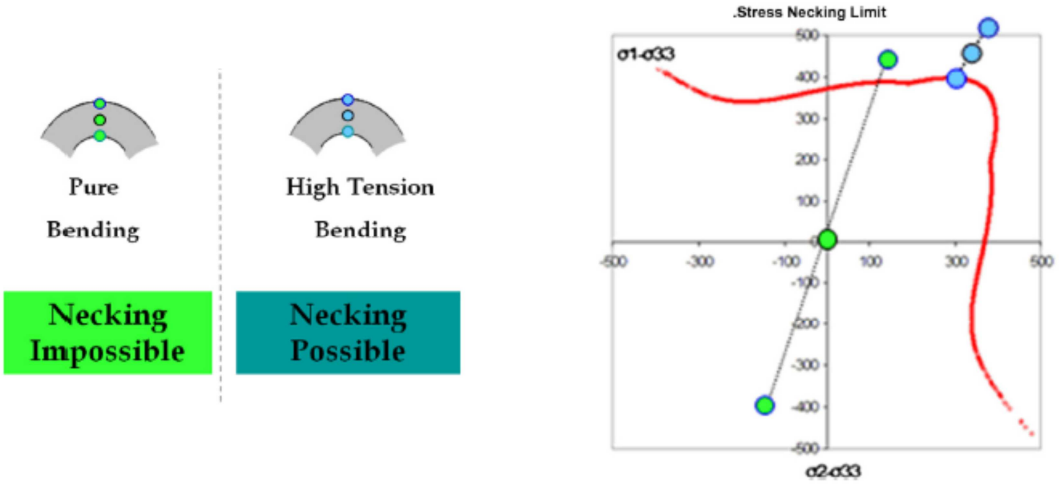

(a) (b)

Figure 3.23. Necking analysis with stress-based FLC: (a) Pure bending *vs* High tension bending; (b) Stress necking limit (extracted from Stoughton & Yoon, 2011).

The concept of high tension bending implies that the analysis of the stress-based FLC based on the major and minor stress values evaluated for each GP, should be performed taking into account their relative through-thickness position. In this study, this analysis was performed taking into account that the blank sheet discretization was built by layers, i.e. first all elements in the lower layer are numbered and only afterwards the

second layer is numbered. Thus, it is possible to quickly identify the lower and upper layer. Moreover, the gauss points are always labelled following the same sequence, as exemplified in Figure 3.24 (a), which allows defining all possible combinations for necking occurrence, as shown in Figure 3.24 (b).

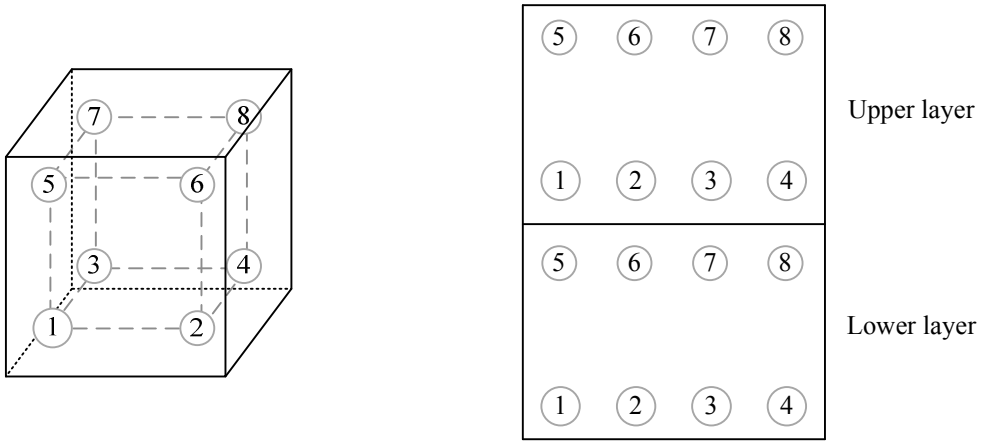

Figure 3.24. (a) Schematic representation of the hexahedral solid element with the 8 GP used in selective reduced integration, identified by local numbers; (b) Four possible combinations of GPs of two elements, corresponding to necking occurrence.

In order to evaluate if a GP is prone to necking, it is necessary to compare its major stress with the admissible one, evaluated based on the experimental stress-based FLC. This is done through a linear interpolation of the experimental data, using a procedure identical to the one explained previously for the FLC, in Equation (3.1). Thus, the interpolated value is determined using the following expression:

$$\sigma_1^{\text{int}} = \sigma_1^{\text{inf}} - \frac{\left(\sigma_1^{\text{sup}} - \sigma_1^{\text{inf}}\right)}{\left(\sigma_2^{\text{sup}} - \sigma_2^{\text{inf}}\right)}\left(\sigma_2^{\text{num}} - \sigma_2^{\text{inf}}\right). \tag{3.2}$$

As for the strain analysis, it is worth nothing that the procedure adopted does not perform any extrapolation of the experimental data, i.e. the interpolated value is only evaluated if the σ_2^{num} is contained within an interval of known experimental data. Table 3.2 presents the outline of the algorithm adopted to perform the formability analysis based on the experimental stress-based FLC. It should be noticed that this algorithm involves the evaluation of the principal stress values for all GP's. Therefore, it can be applied at the end of each user pre-selected increment.

Table 3.2. Outline of the algorithm adopted in the numerical implementation of the rupture criterion based on the experimental FLCS.

READ file containing the FLCS experimental information
DO ig =1, total number of GP's of the deformable body
  Determine the major and minor stress σ_1^{num} and σ_2^{num}
  IF $\sigma_2^{num} \in \left[\sigma_2^{inf}, \sigma_2^{sup}\right]$ THEN
    Determine σ_1^{int} using Equation (3.2)
    IF $\sigma_1^{num} > \sigma_1^{int}$ THEN IFlag(ig)=1
  END IF
END DO
DO i =1, number of elements if the lower layer deformable body
  DO j =1,4 (combinations presented in Equation (3.2))
    Calculate the sum of IFlag(ig) for each 4 GP's in the combination
    IF the sum=4 THEN FIN=True to STOP the computation
  END DO
END DO
IF FIN THEN
  Output the major and minor stress σ_1^{num} and σ_2^{num}
  STOP the computation
END IF

With this algorithm implemented in DD3IMP, the simulation predicted a failure point for a small expansion stroke displacement of 1.75 mm. Figure 3.25 shows the comparison between the stress-based FLC and the numerically predicted stress states for all GP located in the lower layer (labelled z=0) and in the upper layer (labelled z=t). The figure also shows the stress state for the two GP of the first element for which failure is detected (labelled E1 - lower, E1 – upper) and for the second (labelled E2 – lower, E2 – upper). The element E1 is located in the lower layer while E2 is located in the upper layer. As shown in the figure, the values of all layers are above the stress-based FLC. Note that this analysis was done considering that the through-thickness stress is zero ($\sigma_3 = 0$). However, applying the strategy proposed by Stoughton & Yoon, 2011, the results would be similar. Although this location was identified by the stress-based FLC, Figure 3.26 shows that there is no local region with thickness reduction is visible near that element. Moreover, comparing the location identified with the one shown in Figure 3.17, it is clear that they are distinct. Thus, it is not still possible to state that the stress-based FLC allows to identify a failure point. Nevertheless, it should be mentioned that the stress-based FLC used was not identified with the CB2001 yield criterion.

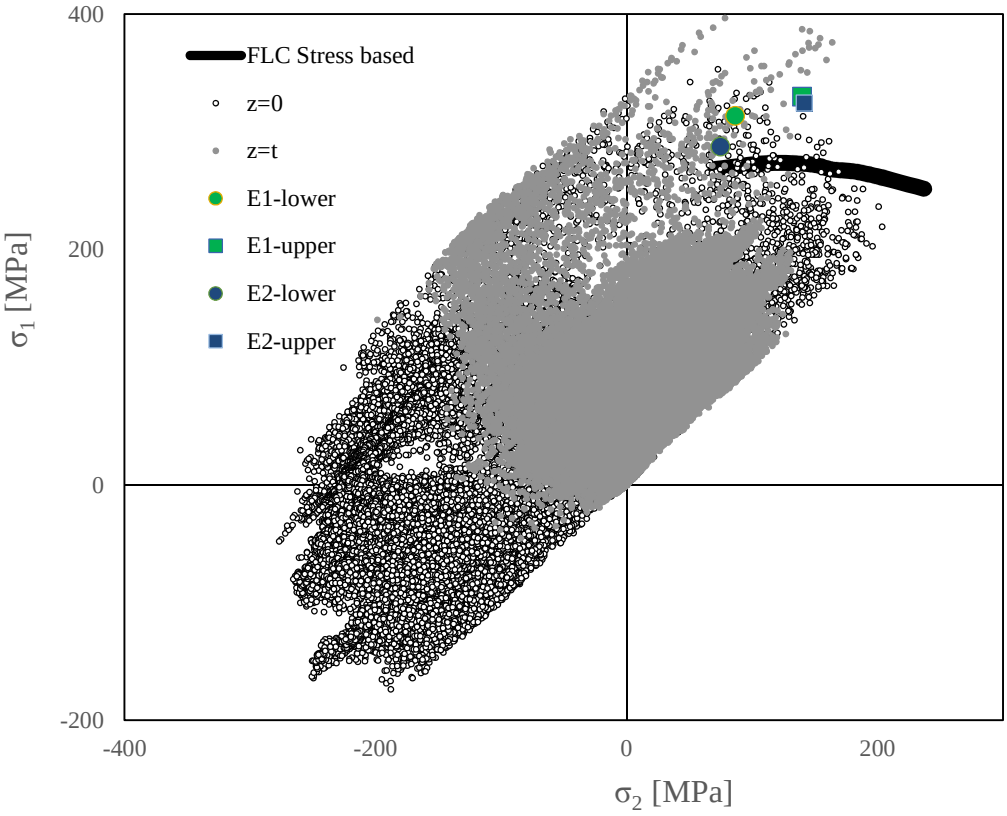

Figure 3.25. Evaluation of σ_1 with σ_2 for the AA5352 aluminum alloy with CB2001 yield criterion.

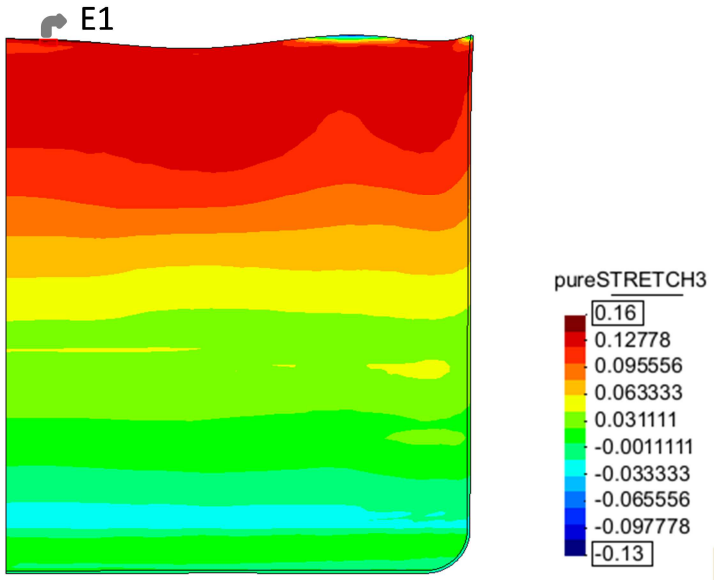

Figure 3.26. Deformation along the thickness direction when the simulation for the AA5352 aluminum alloy with CB2001 yield criterion stopped according to the strategy using stress-based FLC.

3.6. Strain rate analysis – linear best fit

The third strategy adopted to try to predict the instant and the location of the onset of failure is based on the strain rate analysis. This involved the analysis of the thickness strain evolution for some elements located near the necked zone, shown in Figure 3.17. Moreover, the strain history of those elements was followed, during the expansion phase. This allowed to identify the element which presents a higher strain rate. Figure 3.27 presents the major strain, the minor strain and the thickness strain evolution of that element, during the expansion phase. As previously mentioned, the necking is much more distinct if the thinning rate is considered. Thus, Figure 3.27 also presents this rate, evaluated as described in section 2.4.2. The analysis of the evolution of this parameter allows to dividing the curve in three zones:

- Stable area: homogeneous deformation (low slope);
- Begin of instable necking: variation of the deformation (the slope changes);
- Instable zone: instable deformation (high slope).

Therefore, as highlighted in Figure 3.28, the stable and instable areas are fitted with two linear curves ® (linear regression) by using Excel. The intersection of these two straight lines defines the onset of necking, as shown also in this figure, resulting in:

- Expansion punch 3 stroke until necking: 27.6 mm;
- Angle of the onset of failure location: 66.546º;
- Cup Height in the onset of failure location: 50.492 mm.

Figure 3.29 allows comparing the strain paths for the point located in the RD, 45º and the TD positions of the outer flange, with the one for the onset of failure location.

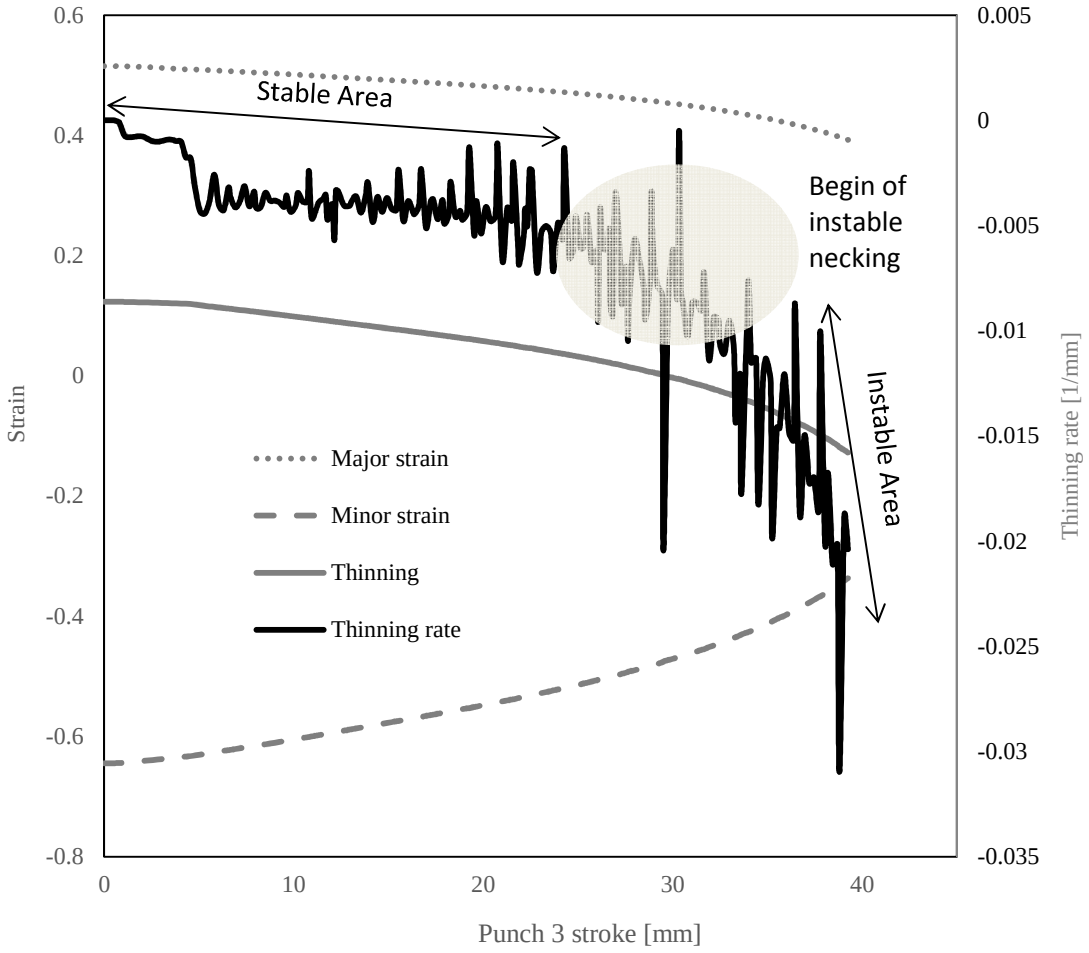

Figure 3.27. Analysis of the deformation and thinning rate during expansion operation for the AA5352 aluminum alloy with yield criterion CB2001, for the element identify for the onset of failure.

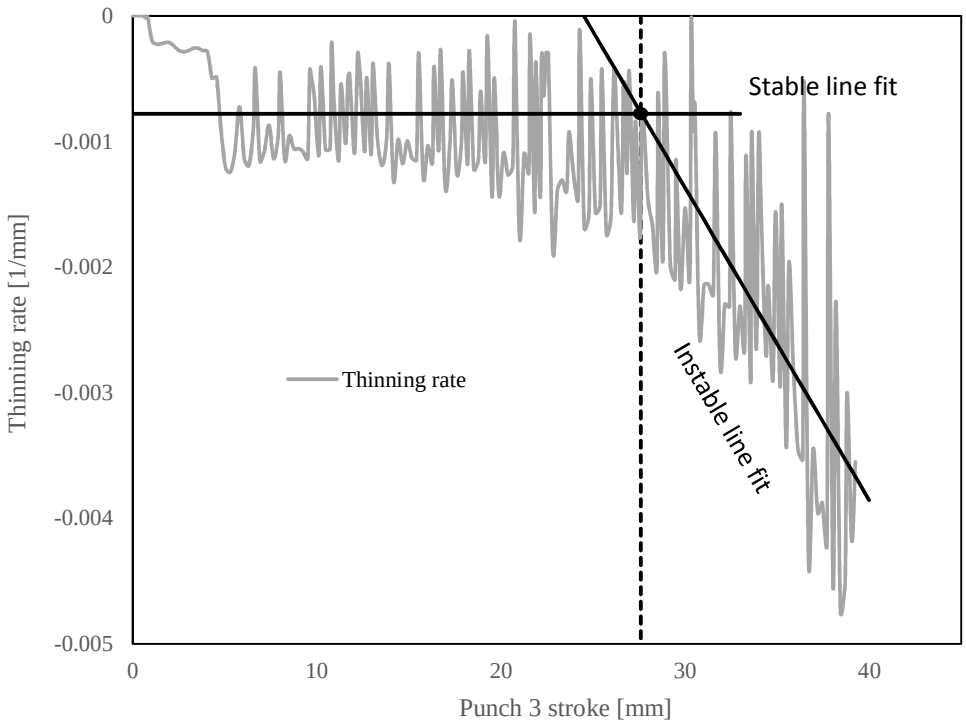

Figure 3.28. Linear best fit.

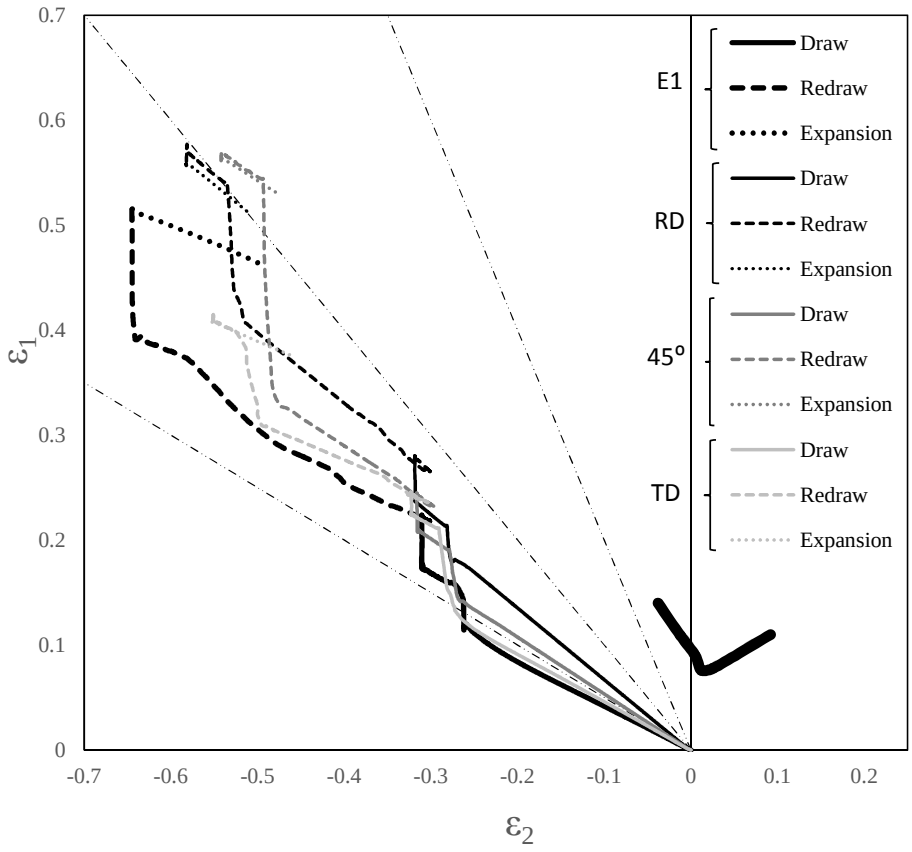

Figure 3.29. Comparison of the strain paths for points located in RD, 45° and TD with the point where necking occurs (necking).

4. CONCLUDING REMARKS

In this work, a can's deep drawing process was studied, including the prediction of the failure instant and location. The stamping operations consider the drawing, reverse redrawing and expansion. Two materials were considered in this study: an AA5352 aluminum alloy and a TH330 steel. For both materials, two yield criteria were used, in order to describe the initial anisotropy of the metal sheet: CB2001 and CPB06. The evolution of the yield surface was described by two hardening laws: Swift law and Voce law for steel and aluminum, respectively. All the numerical simulations of the forming processes were performed with the DD3IMP in-house code.

Numerical simulations were performed for both materials, considering the CB2001 yield criterion, which is known for its accurate description of the material anisotropic behavior, and with the CPB06, which also enables the description of SD effects. The numerical results were analyzed, comparing the CB2001 with CPB06 yield criterion for both materials, considering the punch force evolution, the thickness profile, the cup height and the strain history. For both materials, the CPB06 predicts a higher force punch for the drawing and redrawing operations, while the punch force is higher with the CB2001 for the expansion phase. However, the thickness profiles predicted for both materials are quite different. It is worth mentioning that the thickness predicted for the TH330 steel cup, with the CPB06 yield criterion, is globally lower than the initial thickness, which does not correspond to the expected behavior reported in literature for this type of process. Both yield criteria predict a different cup height, which confirms the influence of the yield criterion in the material flow during the process. In particular, for the AA5352 aluminum alloy, the CPB06 yield criteria predicts two pronounced ears, while the CB2001 predicts eight ears, of smaller amplitude. In brief, the values predicted by CPB06 for the in-plane compression yield stress and r-values can have a significate impact in the results.

The results analysis at the end of the expansion phase show that only the AA5352 aluminum alloy, modelled with the CB2001 yield criterion, presents a pronounced local thickness reduction. In order to predict the instant and location of failure

in this simulation, three methods were used, including the strain-based FLC, stress-based FLC and the through-thickness strain rate. Only the last method allows predicting the failure instant and location, by observing the slope variation of the thinning rate. The analysis performed using the stress-based FLC predicted an instant and location which could not be considered valid, since there is no local thickness reduction. Nevertheless, it should be mentioned that the analysis could be improved, by using the CB2001 yield criterion, in the conversion of the experimental strain-based FLC.

Typically, the strain paths observed for the upper surface of the blank, in the outer flange, are characterized by presenting strain paths situated between pure shear and uniaxial compression, with plane strain path close to the end of the drawing and redrawing stages and also for the expansion phase. The material point corresponding to the failure location, predicted with the CB2001 yield criterion for the AA5352, presents strain paths similar to the other analyzed points.

Globally, the use of the CPB06 yield criterion always lead to safe parts, which can be related with the strategy used to identifies the material parameters. Nevertheless, it should be mentioned that the CB2001 only predicts the occurrence of localized deformation for the AA5352 aluminum alloy. It is also interesting to note that strain history seems to have an influence in the occurrence of localized deformation in the expansion phase, since only the AA5352 aluminum alloy presents a pronounced plane strain path, at the end of the reverse stage, related with the ironing of the flange. Although the experimental results are not yet available, the aluminum alloy presents lower mechanical strength and lower formability for monotonic loads, as shown in the strain-based FLC. Thus, the fact that the aluminum alloy presents necking while no localized strain is predicted for steel maybe an accurate prediction.

5. REFERENCES

Alves, J. L. D. C. M. (2003). Simulação numérica do processo de estampagem de chapas metálicas - Modelação mecânica e métodos numéricos, 403.

Alves, J., Oliveira, M., & Menezes, L. (2004). An advanced constitutive model in the sheet metal forming simulation: the Teodosiu microstructural model and the Cazacu Barlat yield criterion. *Proc. Proc. AIP Conf. Proc*, *451*(10). http://doi.org/10.1063/1.1766765

Banabic, D. (2010). *Sheet Metal Forming Processes*. *Springer*. http://doi.org/10.1007/978-3-540-88113-1

Banabic, D., Aretz, H., Comsa, D. S., & Paraianu, L. (2005). No Title. *Int. J. Plast.*, *21*, 493–512.

Barlat, F., Chung, K., & Richmond, O. (1994). Anisotropic Plastic Potentials for Polycrystals and Application to the Design of Optimum Blank Shapes in Sheet Forming.

Barlat, F., Lege, D., & Brem, J. (1991). A six-component yield function for anisotropic materials. *International Journal of Plasticity*, *7*, 693–712.

Barros, P. (2011). Pre-Strain Effect on Spring back of 2-D Draw Bending.

Barros, P. D., Alves, J. L., Oliveira, M. C., & Menezes, L. F. (2016). Modeling of tension–compression asymmetry and orthotropy on metallic materials: Numerical implementation and validation. *International Journal of Mechanical Sciences*, *114*, 217–232. http://doi.org/10.1016/j.ijmecsci.2016.05.020

Barros, P. D., Oliveira, M. C., Alves, J. L., Andrade-Campos, A., & Menezes, L. F. (2015). Modelling of tension-compression asymmetry and orthotropic anisotropy in case of thin metallic sheets: identification procedure and case studies, 149–154.

Barros, P. D., Oliveira, M. C., Alves, J. L., & Menezes, L. F. (2013). Earing Prediction in Drawing and Ironing Processes Using an Advanced Yield Criterion. *Key Engineering Materials*, *554-557*, 2266–2276. http://doi.org/10.4028/www.scientific.net/KEM.554-557.2266

Cazacu, O., & Barlat, F. (2001). Generalization of Drucker's yield criterion to orthotropy.

Mathematics and Mechanics of Solids, *6*, 613–630.

Cazacu, O., & Barlat, F. (2004). A criterion for description of anisotropy and yield differential effects in pressure-insensitive metals. *International Journal of Plasticity*, *20*(11), 2027–2045. http://doi.org/10.1016/j.ijplas.2003.11.021

Cazacu, O., Plunkett, B., & Barlat, F. (2006). Orthotropic yield criterion for hexagonal closed packed metals. *International Journal of Plasticity*, *22*(7), 1171–1194. http://doi.org/10.1016/j.ijplas.2005.06.001

Chung, K., Kim, D., & Park, T. (2011). Analytical derivation of earing in circular cup drawing based on simple tension properties. *European Journal of Mechanics - A/Solids*, *30*(3), 275–280. http://doi.org/10.1016/j.euromechsol.2011.01.006

Dequiedt, J. L. (2015). Statistics of dynamic fragmentation for a necking instability. http://doi.org/10.1016/j.ijsolstr.2015.06.028

Dick, R. E. (2011). BENCHMARK 1 - Earing Evolution During Drawing and Ironing Processes Jeong Whan Yoon (Swinburne University of Technology , Australia) 1-1 : TOOLING GEOMETRY, 1–4.

Dick, R. E., Whan Yoon, J., & Stoughton, T. B. (2015). Path-independent forming limit models for multi-stage forming processes. http://doi.org/10.1007/s12289-015-1220-4

Du, C., Stoughton, T., Huang, G., Shi, M. F., Yang, L., & Wu, X. (2013). BENCHMARK 1 - Nonlinear Strain Path Forming Limit of a Reverse draw. *Journal of Chemical Information and Modeling*, *53*(9), 1689–1699. http://doi.org/10.1017/CBO9781107415324.004

Feistle, M., Golle, R., & Volk, W. (2016). Determining the Influence of Shear Cutting Parameters on the Edge Cracking Susceptibility of High-strength-steels Using the Edge-fracture-tensile-test. *Procedia CIRP*, *41*, 1078–1083. http://doi.org/10.1016/j.procir.2016.01.007

Frederick, C. O., & Armstrong, P. J. (2007). A mathematical representation of the multiaxial Bauschinger effect. *Materials at High Temperatures*, *24*(1), 1–26. http://doi.org/10.3184/096034007X207589

Gurson, A. L. (1977). Continuum Theory of Ductile Rupture by Void Nucleation and Growth: Part I—Yield Criteria and Flow Rules for Porous Ductile Media. *J.Eng. Mater. Technol*, *99*, 2–15. http://doi.org/10.1115/1.3443401

Hasan, R. Z., Kinsey, B. L., & Tsukrov, I. (2011). Effect of Element Types on Failure

Prediction Using a Stress-Based Forming Limit Curve. *J. Manuf. Sci. Eng*. http://doi.org/10.1115/1.4005044

Hill, R. (1948). A theory of the yielding and plastic flow of anisotropic metals. In *Proceedings of the Royal Society of London. Series A. Mathematical and Physical Sciences* (pp. 281–297).

http://www.clker.com/. (n.d.). Retrieved May 23, 2016, from http://www.clker.com/clipart-247204.html

http://www.expack.co.uk. (n.d.). Retrieved June 14, 2016, from http://www.expack.co.uk

Isik, K., Silva, M. B., Tekkaya, A. E., & Martins, P. A. F. (2014). Formability limits by fracture in sheet metal forming. *Journal of Materials Processing Technology*, *214*(8), 1557–1565. http://doi.org/10.1016/j.jmatprotec.2014.02.026

Kanetake, N., & Tozawa, Y. (1987). Crystallographical Calculation of Earing in Deep Drawing under Various Conditions, *7*, 131–147.

Lee, J., Kim, D., Lee, Y.-S., Bong, H. J., Barlat, F., & Lee, M.-G. (2015). Stress update algorithm for enhanced homogeneous anisotropic hardening model. *Comput. Methods Appl. Mech. Engrg.*, *286*, 63–86. http://doi.org/10.1016/j.cma.2014.12.016

Lemaitre, J. (1985). A Continuous Damage Mechanics Model for Ductile Fracture. *J. Eng. Mater. Technol*, *107(1)*, 83–89. http://doi.org/10.1115/1.3225775

Li, H. W., Yang, H., & Sun, Z. C. (2008). A robust integration algorithm for implementing rate dependent crystal plasticity into explicit finite element method. *International Journal of Plasticity*, *24*(2), 267–288. http://doi.org/10.1016/j.ijplas.2007.03.014

Li, K. P., Carden, W. P., & Wagoner, R. H. (2002). Simulation of springback. *International Journal of Mechanical Sciences*, *44*(1), 103–122. http://doi.org/10.1016/S0020-7403(01)00083-2

Lin, C.-T., & Kwan, C.-T. (2009). Application of abductive network and FEM to predict the optimal blank contour of an elliptic cylindrical cup from deep drawing. *Journal of Materials Processing Technology*, *209*(3), 1351–1361. http://doi.org/10.1016/j.jmatprotec.2008.03.042

Malcher, L. (2012). Continuum Modelling and Numerical Simulation of Damage for Ductile Materials.

Martins, P. A. F., Bay, N., Tekkaya, A. E., & Atkins, A. G. (2014). Characterization of fracture loci in metal forming. *International Journal of Mechanical Sciences*, *83*,

112–123. http://doi.org/10.1016/j.ijmecsci.2014.04.003

Mc-Meeking, R. M., & Rice, J. . (1975). Finite element formulations for problems of large elastic-plastic deformation. *Int.J. Solids Struct.*, *11*, 601–616.

Menezes, L. F., & Teodosiu, C. (2000). Three-dimensional numerical simulation of the deep-drawing process using solid finite elements. *Journal of Materials Processing Technology*, *97*(1), 100–106. http://doi.org/10.1016/S0924-0136(99)00345-3

Needleman, A., & Tvergaard, V. (1984). An analysis of ductile rupture in notched bars. *Journal of the Mechanics and Physics of Solids*, *32*(6), 461–490. http://doi.org/10.1016/0022-5096(84)90031-0

Neto, D. M. (2014). Numerical simulation of frictional contact problems using Nagata patches in surface smoothing, (September), 350.

Nikhare, C., Marcondes, P. V, Weiss, M., & Hodgson, P. D. (2008). EXPERIMENTAL AND NUMERICAL EVALUATION OF FORMING AND FRACTURE BEHAVIOUR OF HIGH STRENGTH STEEL.

Stoughton, T. B., & Yoon, J. W. (2011a). A new approach for failure criterion for sheet metals. *International Journal of Plasticity*, *27*(3), 440–459. http://doi.org/10.1016/j.ijplas.2010.07.004

Stoughton, T. B., & Yoon, J. W. (2011b). Paradigm Change: Alternate Approaches to Constitutive and Necking Models for Sheet Metal Forming, *15*(10), 1541–1407. http://doi.org/10.1063/1.2011245

Stoughton, T. B., & Yoon, J. W. (2012). Path independent forming limits in strain and stress spaces. *International Journal of Solids and Structures*, *49*(25), 3616–3625. http://doi.org/10.1016/j.ijsolstr.2012.08.004

Tekkaya, A. E. (2000). State-of-the-art of simulation of sheet metal forming. *J Mater Process Technol*, *103*, 14–22.

Tharrett, M., & Stoughton, T. (2003). Stretch-bend forming limits of 1008 AK steel.

Thuillier, S., Manach, P. Y., & Menezes, L. F. (2010). Occurence of strain path changes in a two-stage deep drawing process. *Journal of Materials Processing Technology*, *210*(2), 226–232. http://doi.org/10.1016/j.jmatprotec.2009.09.004

Volk, W., & Hora, P. (2010). New algorithm for a robust user-independent evaluation of beginning instability for the experimental FLC determination. http://doi.org/10.1007/s12289-010-1012-9

Vrh, M., Halilovič, M., Starman, B., Štok, B., Comsa, D.-S., & Banabic, D. (2014). Capability of the BBC2008 yield criterion in predicting the earing profile in cup deep drawing simulations. *European Journal of Mechanics - A/Solids*, *45*, 59–74. http://doi.org/10.1016/j.euromechsol.2013.11.013

Wallmeier, M., Linvill, E., Hauptmann, M., Majschak, J.-P., & Östlund, S. (2015). Explicit FEM analysis of the deep drawing of paperboard. *Mechanics of Materials*, *89*, 202–215. http://doi.org/10.1016/j.mechmat.2015.06.014

Watson, M., Dick, R., Huang, Y. H., & Lockley, A. (2016). Benchmark 1 – Failure Prediction after Cup Drawing , Reverse Redrawing and Expansion, 1–14.

www.meatsandsausages.com. (n.d.). Retrieved June 7, 2016, from http://www.meatsandsausages.com/canning-equipment/canners-cans

Yoon, J. W., Dick, R. E., & Barlat, F. (2011). A new analytical theory for earing generated from anisotropic plasticity. *International Journal of Plasticity*, *27*(8), 1165–1184. http://doi.org/10.1016/j.ijplas.2011.01.002

Yoon, J.-H., Cazacu, O., Whan Yoon, J., & Dick, R. E. (2010). Earing predictions for strongly textured aluminum sheets. *International Journal of Mechanical Sciences*, *52*(12), 1563–1578. http://doi.org/10.1016/j.ijmecsci.2010.07.005

ANNEX A

Triaxiality and Lode Angle

The analysis of the void evolution, for a unitary cell, or of the void volume fraction, f, using a single element, requires the knowledge of the effective stresses to be applied in each plane. In fact, it is required to know the ratio between the effective macro-stresses, in each direction. Typically, the user knows the value of the stress triaxiality, defined as:

$$T_{\Sigma} = \frac{\Sigma_M}{\sqrt{3J_2}} \tag{A.1}$$

and the Lode parameter, defined as:

$$\mu_{\Sigma} = \frac{3\sqrt{3}}{2}\frac{J_3}{J_2^{3/2}} \tag{A.2}$$

to be studied. Assuming that the average stress (Σ_M) is known, it is possible from (A.1) to determine J_2, such as:

$$J_2 = \frac{1}{3}\left(\frac{\Sigma_m}{T_{\Sigma}}\right)^2. \tag{A.3}$$

Moreover, from (A.2), J_2 can be defined as:

$$J_2 = \left(\frac{3\sqrt{3}}{2}\frac{J_3}{\mu_{\Sigma}}\right)^{2/3}. \tag{A.4}$$

The equality between (A.3) and (A.4) allows to define J_3 as a function of the assumed as known parameters:

$$J_3 = \left[\frac{1}{3}\left(\frac{\Sigma_m}{T_{\Sigma}}\right)^2\left(\frac{2}{3\sqrt{3}}\mu_{\Sigma}\right)^{2/3}\right]^{3/2}. \tag{A.5}$$

Considering an equibiaxial stress state, for instance:

$$\frac{\Sigma_1}{\Sigma_2} = 1 \Leftrightarrow \Sigma_1 = \Sigma_2, \tag{A.6}$$

it is possible to define:

$$\Sigma_3 = 3\Sigma_m - 2\Sigma_1, \tag{A.7}$$

based on the average stress definition. Under this conditions, J_3 can also be calculated as:

$$J_3 = \left(\Sigma_1 - \Sigma_m\right)^2 \left(2\Sigma_m - 2\Sigma_1\right). \tag{A.8}$$

At this stage, it is possible to use the Solver from Excel® in order to determine the average stress $\left(\Sigma_m\right)$ value that guarantees that J_3 calculated with (A.5) is equal to the one obtained with (A.8). Finally, the second invariant J_2 and the effective stress are calculated as follows:

$$J_2 = \frac{{\Sigma_e}^2}{3} \text{ or } J_2 = \frac{1}{2}\left({\Sigma_1}^2 + {\Sigma_2}^2 + {\Sigma_3}^2\right), \tag{A.9}$$

$$\Sigma_e = \sqrt{3J_2}\ . \tag{A.10}$$

This procedure was used to define the conditions to perform the analysis of the void volume fraction evolution, considering: (i) a single element and (ii) a three-dimensional unit cell. The initial porosity is 1%, which corresponds a void radius equal to 0.271 mm. For the GTN model (see section 2.4.3.2), all the adjustment parameters, q_1, q_2 and q_3, where considered equal to 1.0. The material selected for the analysis is the TH330 steel, described with the Swift hardening law parameters given in Table 2.2 and the CPB06 yield criterion (see Table 2.5). For the analysis of the three-dimensional unit cell, the Hill'48 yield criterion was used, in order to try to evaluate the influence of the SD effect. The anisotropy parameters considered for the Hill'48 yield criterion are shown in Table A. 1.

Table A. 1. Hill'48 anisotropy parameters.

F	G	H	M	L	N
0.369525	0.380126	0.550982	1.5	1.5	1.333786

Figure A.1 shows the results obtained for the single element, considering different values for the stress triaxiality, in the range $T_\Sigma \in [2/3;5]$ and two values for the Lode parameter: -1.0 and 1.0. The results show a similar trend except for the lower value of stress triaxiality, for which the volume void fraction evolution has a higher slope for the positive value of the Lode parameter.

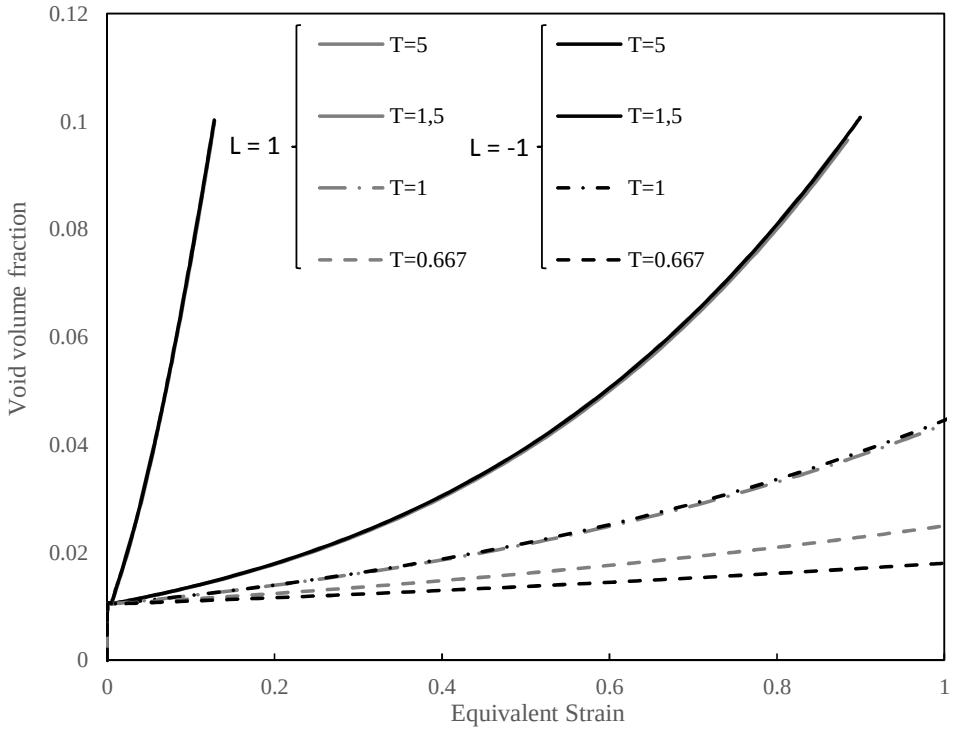

Figure A.1. Void volume fraction evolution predicted using the GTN model for a single element, considering different values for the stress triaxiality (labeled "T") for two values of the Lode parameter (labeled "L").

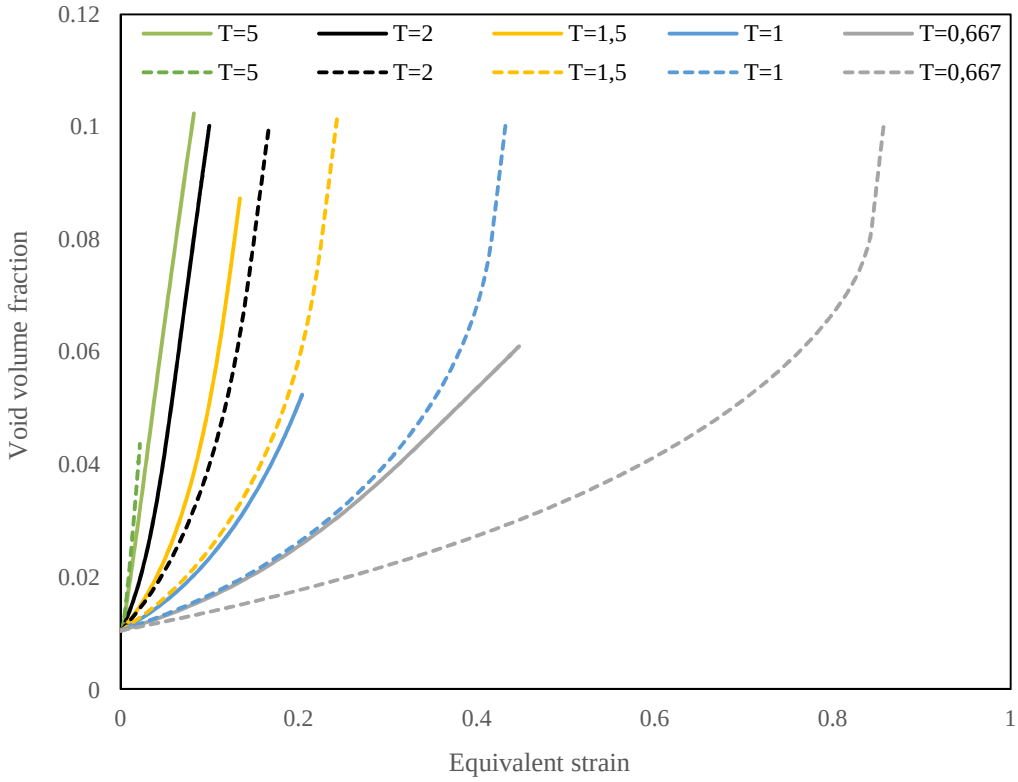

Figure A. 2. Void volume fraction evolution predicted for a three-dimensional unit cell, considering the CPB06 (continuous line) and the Hill'48 (dashed line) yield criteria, using different values for the stress triaxiality (labeled "T") and a Lode parameter equal to 1.0.

Figure A. 2 shows the results obtained for a three-dimensional unit cell, considering the same range of values for the stress triaxiality and a value for the Lode parameter equal to 1.0. Figure A. 3 presents the same results for a Lode parameter equal to -1.0. Comparing both figures it is possible to conclude that the CPB06 yield criterion predicts a void volume fraction evolution with a higher slope, except for the highest value of stress triaxiality. Moreover, for the positive value of the Lode parameter, the slope of the void volume fraction *vs* equivalent strain is higher. Finally, Figure A. 4 shows the distribution of the equivalent plastic strain for both yield criteria, for the stress triaxiality of 1.5, highlighting the differences in the predicted void shape.

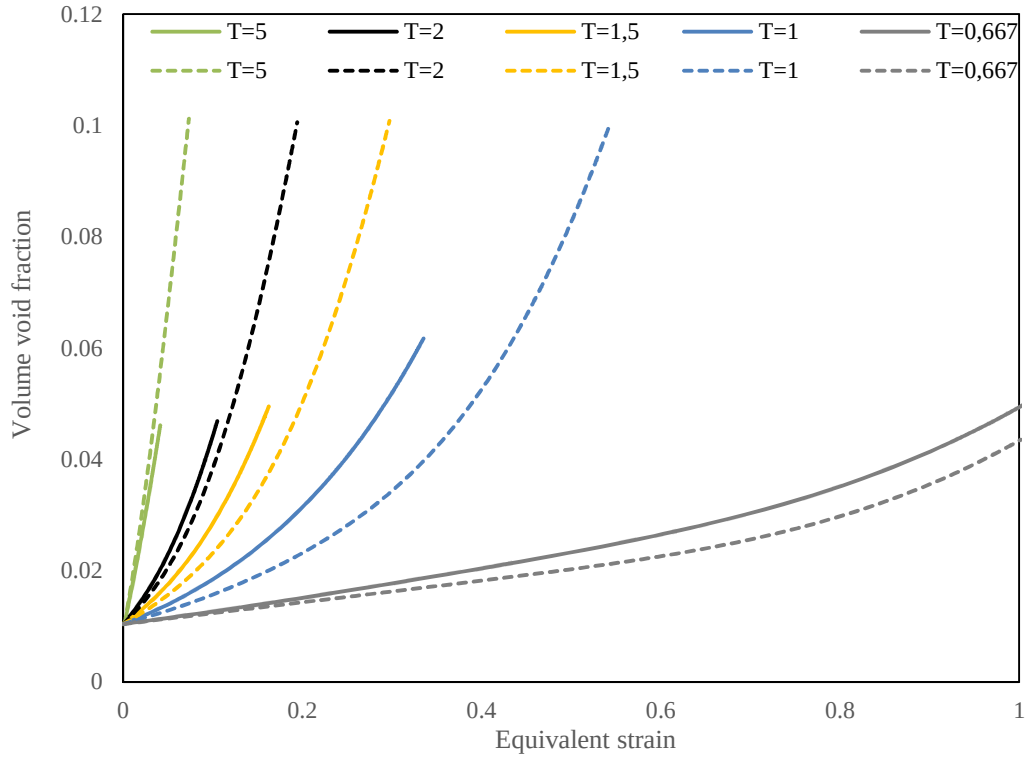

Figure A. 3. Void volume fraction evolution predicted for a three-dimensional unit cell, considering the CPB06 (continuous line) and the Hill'48 (dashed line) yield criteria, using different values for the stress triaxiality (labeled "T") and a Lode parameter equal to -1.0.

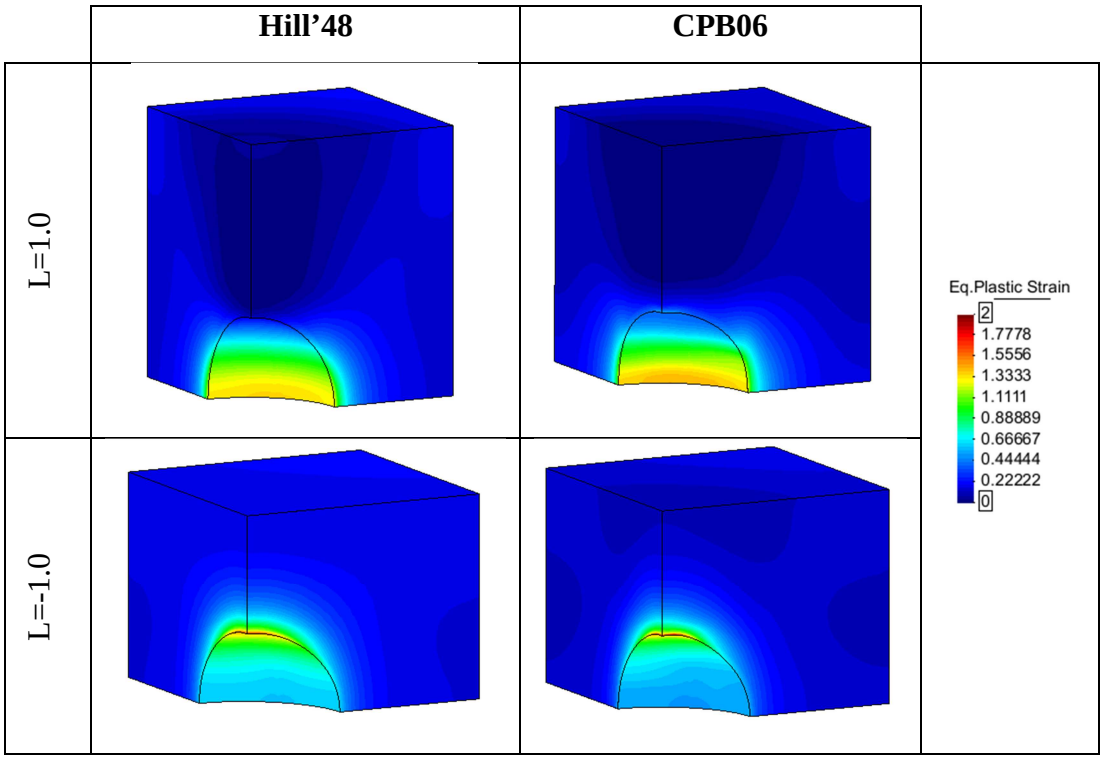

Figure A. 4. Distribution of the equivalent plastic strain in the three-dimensional unit cell, for both yield criteria, for the stress triaxiality of 1.5.